Faculty of Engineering and Surveying

University of Southern Queensland

CRITICAL ISSUES IN PRECISE MACHINING OF OVERSIZE MOULDS IN POLYSTYRENE

A Dissertation submitted by

Muhammad Razif Mahadi

MSc (Biosystems Engineering), BSc (Mechanical Engineering)

For the award of

Doctor of Philosophy

2011

Abstract

Parts made from fibre reinforced plastics (FRP) are first laid up on a polystyrene mould. Hence dimensional accuracy is dependent on the quality of the mould. If the parts are oversize, larger than a metre or so, the moulds must be machined in sections and fitted together. There is therefore substantial advantage in a new machining system that can manufacture the mould as one piece. Currently, moulds are machined on a multi-axis robotic or CNC machine that removes material using a milling cutter. When an observation of the current system was conducted on site, the industrial partner gave permission to use their CNC milling robot for cutting expanded polystyrene. A medium density board was also tested. The cutting forces were recorded. It was found that adapting the same cutting strategy was inefficient. The design of such a machine must be based on a new set of requirements.

A number of design factors must be considered. The new machine would be massive and expensive unless three critical issues were resolved at the design stage; cutting approach, instrumentation for control of accuracy, and innovation in the drive.

For removing polystyrene, slicing was considered as an alternative to milling. The fundamental operations of slicing are discussed, from simple pushing of the blade to the incorporation of sideways forces and motions. When using a straight blade, the cutting action can be assumed to act along a straight line. For a curved blade, the straight line was replaced by an effective sector curve, measured from an imaginary centre. While a curved blade and a disk blade work with the same principle, the central axis of a disk blade is fixed, thus the effective sector curve is constant. This

allows the disk blade to provide constant sideways force uni-directionally. For slicing, the cutting surface has been evaluated by carving polystyrene with a variety of blades. Later, the force required for cutting with a disk blade was analysed. It was confirmed that a higher cutting speed generated higher cutting forces, but for equal feed rates the cutting force was substantially lower than that required for milling.

The size of the machine was set at five metres by five in plan and two metres in height. It was necessary to devise a position transducer that could operate over these distances, while giving a resolution of a tenth of a millimetre. A transducer was devised based on the visual interpretation of graduations on a precision tape with markings at two millimetre intervals. The concept was embodied using a self-built line-scan camera. The camera performed scans at one or two millisecond intervals, leading to the choice of two millimetre graduations as a compromise between precision and the risk of aliasing at a speed of up to half a metre per second.

A Cartesian gantry configuration was selected as the base platform for the cutting machine. A light weight solution was studied. Traction was provided to each axis using a soft rubber wheel and a pair of DC motors, mounted on the slider. It was possible to combine more than one motor for actuating the slider, if necessitated by heavier loads. In the development of the transducer, a displacement of five metres was achievable with the required placement accuracy. The embedded microcontroller that formed part of the transducer was equipped with an algorithm for precise movement control. Using a nonlinear velocity demand strategy enabled the motion parameters to be optimized.

In summary, construction of a full-sized prototype axis has enabled the critical issues to be researched thoroughly. This had created a clear path to the final design.

CERTIFICATION OF DISSERTATION

I certify that the ideas, experimental work, results, analyses, software and conclusions reported in this dissertation are entirely my own effort, except where otherwise acknowledged. I also certify that the work is original and has not been previously submitted for any other award, except where otherwise acknowledged.

_____ _____

Signature of Candidate Date

ENDORSEMENT

_____ _____

Signature of Supervisor Date

ACKNOWLEDGEMENTS

Fresh from graduation of Bachelor of Science in Mechanical Engineering from the California State University, Sacramento, I was working as process engineering for a manufacturing firm in Malaysia. Then, I was offered a tutor position at the Department of Biological and Agricultural Engineering, Universiti Putra Malaysia. Part of the job is to conduct research and development in the application of mechatronics in agriculture. In order to enhance my knowledge, I had successfully completing a Master of Science Degree in Biosystems Engineering at the University of Manitoba Canada. Upon returning home, I have planned for a future research that integrates agriculture with mechatronics. The field is new in Malaysia. Therefore, the best way is to learn from an international expert. Then, a scholarship was successfully secured from the Ministry of Higher Education of Malaysia.

In mid 2006, Professor John Billingsley of the University of Southern Queensland, Australia had accepted my application to conduct research in mechatronics under his supervision. It was a great pleasure for me to have him as my mentor. While preparing for the dissertation proposal, we were informed that the Buchanan Advanced Composites (BAC) was proposing a new machining project. A meeting was set between Mr. Norm Watt (Managing Director of BAC), Professor Billingsley and I. The project was not directly related to agriculture, but the concept was similar. Hence, the Advanced Control Research group of the Faculty of Engineering and Surveying, USQ and BAC had agreed on a collaboration.

Mr. Tim Harris of BAC was appointed as the liaison officer between the research group and BAC. As a liaison officer, Tim had provided valuable input about the operation and major problems with the current system.

Under the guidance of Professor Billingsley, I had developed a general framework for the research. Initially, the overall plan was too wide for a research person to handle within a reasonable time frame. Then a committee that consisted of Professor Billingsley, Dr. Sam Cubero, the Associate Dean of Research David Buttsworth, Dr. Paul Wen, Mr. Tim Harris and Mr. Rex Parmenter had advised that the research scope should be narrowed down to the most critical issues that challenge precise machining in oversize polystyrene large moulds for fibre layup.

As the research was progressing, some components were needed and fabricated. The support team of the Faculty, Bratt, Terry, Chris, Brian, Mohan and Adrian were always there to provide assistance. There were times when I had problems with the circuit board that I had designed. It was Dean Beliveau who helped me in troubleshooting.

As time passing by, Tim had moved on to another firm, Jake Williams had taken over the position as the liaison officer. In the beginning, the transducer was tested under the lab condition. Then, the time had come when the performance of a full scale prototype gantry need to be observed and verified. Utilizing his skills as a machinist and a designer, a full size prototype gantry was finally fabricated. Resourceful, creative and patient, Jake was the greatest ally I ever had during this entire journey.

Commuting between the BAC plant and the campus was a huge problem. Fortunately, Wendy Watt was more than happy to give me a lift.

While working on the cutting characteristics of expanded polystyrene, two practical training students from the local high school, Cody and Morgan, were more than willing to assist in the experiments. In return, I had provided some basic introduction to AutoCAD. They were very pleased, and I really appreciated the time we had spent together.

Working on the project was part of the requirement; the other was translating the entire process into a dissertation format. I would like to thank to Dr Selvan Pather for his comments on my earlier drafts. I would also like to thank to Juanita Ryan for helping me with the administrative issue.

A day at work was sometimes very stressful. I was blessed to have Fariza, my lovely wife and Hassan my little one. They were always there to support me, in good times and bad times.

Thank you everyone.

Table of Contents

Table of Figures

List of Tables

Chapter 1

Introduction

Parts made of fibre reinforced plastic (FRP) materials are manufactured using a moulding technique. The accuracy of the manufactured components is heavily reliant on the quality of the moulds. These are typically made of polystyrene blocks, shaped on a multi-axis milling machine. While machines that are one metre by two metres can be commonly found in industry, larger footprint with higher ground clearance machines are less common, and very expensive. With a restriction on the size of the cutting machine, the current practice is to assemble smaller parts to form an oversize mould.

A large machine that is affordable for a medium scale industry is desired that will allow fabrication of an oversize part as one piece. The design of such a machine involved many interlocking aspects that included efficient cutting approaches, the mechanical framework to enclose the entire workpiece, and an affordable positioning system to control the movement of the cutter. These were the critical issues that influenced the overall design of a precise cutting machine.

The aim of this research was to provide a breakthrough in the design of a mechanism for precise machining in oversize polystyrene moulds. The critical issues were studied and discussed in depth. These had led to original contributions in the cutting

behaviour of expanded polystyrene based on slicing and the mechatronics approach in the control of long travel gantry sliders.

1.1 Background

Consumer demands for light weight, strength and durability in the design for high performance boats and land vehicles has called for applications of FRP materials as substitute to metals. Examples of such materials are fibre glass and carbon fibre. Components made of FRP are usually created from moulds, wherein layers of fibres are lay-up. Typically, components for marine and land vehicles are more than two metres in length and width.

A prominent FRP manufacturing house in Toowoomba, Buchanan Advanced Composite (BAC) had been actively seeking new methods to simplify the moulding process. This had established a link between the industry and the Faculty of Engineering and Surveying of USQ. This research had been motivated by the needs of the industry to design a specialized machine for making polystyrene moulds.

Hand lay-up, or sometimes referred to as contact moulding, is widely applied in the manufacturing of fibre composite components (Edwards, 1998; Shan and Qiao, 2005; Chaudhuri and Balaraman, 2007). The BAC practises a variation of this technique to fabricate parts from fibre composites. The mould acts as a one-off template. Hence, a cheap material such as expanded polystyrene is preferred. In the manufacture of

oversize components, a large mould is required. In general, the construction methods are classified into two; segment bonding and single machining.

In segment bonding, an oversize component is broken into smaller segments. Each segment is machined separately. A complete mould is formed when the segments are joined together. Using this method, the overall size of the mould is unlimited. However, bonding of smaller segments leads to dimensioning error. One of the reasons is due to variation in the machine setup for machining individual segments. Because resins are applied to hold the segments together, there are also errors in bonding since the process is done manually. The effect of error in bonding smaller segments is cumulative.

From the industry point of view, a desirable alternative is to machine an oversize mould directly as one piece. Therefore, bonding errors are eliminated from the manufacturing process that shortened the manufacturing period. In order to produce such a mould, a large machine is required. The machine must be large enough to encompass the entire component. The machine must also be capable of directing and orienting the cutter head to reach any points on the work piece in the desired 3-D space.

The final aim was to design a cutting machine that covers a height of two metres with five metres by five metres ground area. An accuracy of 100 microns in tool positioning was also included as a requirement. This level of accuracy was an aesthetic constraint. The experience of the industry indicates a machining fluctuation

of greater than 100 microns on a flat surface produces bumps and waves that in reflections are visible to the naked eye. This research was aimed at developing the conceptual design of the intended cutting machine, whereas critical design issues were highlighted and novel solutions that were also cost effective were proposed.

1.2 Field Observation on Milling Polystyrene

In order to comprehend the current design problems that the industry and the industrial partner in particular were facing, a field observation was conducted. In this section, the cutting force of a ball-end mill to cut expanded polystyrene was observed.

Milling is a viable means of machining expanded polystyrene (Lye et al., 1996). The tool cuts the material through physical contact. In milling, cutting is performed by feeding the cutter along the cutting direction, normal to the axis of the spindle. The teeth of the end mill shatter the excess parts of the work piece as the cutter is fed along the cutting line.

Most manufacturing houses use CNC milling machine to fabricate polystyrene moulds. While milling the material, the industry has experienced several setbacks, primarily on the condition of the excess materials that turns into fine particles. The debris readily clogs moving components of the machine as well as being tedious to clean. Because fine chips have little economic value, this has become an annoyance.

CNC milling cutters are commonly used for sculpting of surfaces on solid (Guzel and Lazoglu, 2004). A multi-axis CNC machine equipped with this cutter can generate wide range of shapes from various types of materials. The number of axes determines the number of ways that the cutter can be oriented within the workspace (Tutunea-Fatan and Feng, 2005). Designs of most CNC milling machines are based on a gantry configuration in order to utilize the rigidity characteristics of this design. The three-axis (Sheen and You, 2006) and five-axis (Sencer et al., 2008) milling machines are commonly used.

In order to create a smooth appearance, the workpiece is milled in multi stages (Kim et al., 2007). The first stage usually removes the greatest volume of excess material. Generally referred to as the roughing stage, this process creates the general outline of the designed feature. There are subsequent stages that aim to create the shape gradually. The final stage focuses on the task of refining the shape. It is not impossible for one tool to be used in all stages, but the cutting parameters for feed speed and the spindle speed are different (Aspinwall et al., 2007). The effect of resistance force is significant during roughing process, because large amounts of material are removed (Budak, 2006). However, the magnitude of the cutting force reduces as the shape is refined, because now the removal of the excess material is less. Several passes are needed before the shape can be finalised. Thus milling method is also time-consuming.

1.2.1 Expanded Polystyrene

Expanded polystyrene has a wide range of densities. The value of densities is directly proportional to the amount of blowing agents being added. The polystyrene foam is produced synthetically by adding gas to styrene during polymerization. The gas acts as a blowing agent that expands the styrene foam. Higher amount of blowing agents produces lower density blocks (Pallay et al., 2000). Blocks of higher densities have greater thermal resistance, as well as high tensile and compressive strengths.

In general an expanded polystyrene block consists of compressed spheres. The block is stable under room condition. The size of the spheres is larger for lower densities block. Figure 1.1 shows two types of expanded polystyrene block. Figure 1.1 (a) shows a sample of high-density expanded polystyrene, provided by the industrial partner. This type is used for making moulds. A sample of the low-density type is shown in Figure 1.1 (b). The low-density polystyrene was obtained from a local shop; it is commonly used in decoration, signage, and packaging works.

(a)

(b)

Figure 1. 1 (a) High density polystyrene foam, (b) Low density polystyrene foam

The engineering properties of expanded polystyrene vary considerably among manufacturers, thus the material is not recommended for structural work (Rusmee et al., 2001). Table 1.1 lists the common engineering properties of expanded polystyrene blocks, surveyed from various manufacturers. Typical range of densities is from 15 kg/m^3 to 68 kg/m^3. The tensile strength is from 150 kPa to 744 kPa. On shear strength, the values are from 90 kPa to 220 kPa. The glass temperature occurs at 95^oC. The melting point is 240^oC, which is relatively low compared to most solid materials. In lay-up process, a high-density polystyrene block is preferred for making moulds as it is harder to compressed.

Table 1. 1 Typical engineering properties of expanded polystyrene blocks

Properties	Values	Units
Density	15-68	kg/m^3
Tensile Strength	150-744	kPa
Shear Strength	90-220	kPa
Glass Temperature	95	^oC
Melting Points	240	^oC

1.2.2 Experimental Set-Up

Milling tests were conducted on the manufacturing site. The BAC had permitted the use of their CNC milling robot for the cutting tests. The robot comprised of a platform for placement of the workpiece and there was a three axes gantry for tool manipulation. The spindle for tool actuation was powered by a 2 kW AC motor.

Although BAC prefers expanded polystyrene for making moulds, there are cases where medium density boards are also used. Therefore, in this experiment, both materials were tested. Typical machining parameters were applied during the test. The cutter type was a ball-end mill, with a diameter of 25.4 mm. For testing, the cutter was used to create a 300 mm long straight line cut. The spindle speed of the end-mill was 22,000 RPM. The feed speed was 5 mm/s. The feed speed of this value is also typical in the roughing process used by the manufacturing house. The cutting depth was 12.7 mm. This depth was measured from the top surface of the workpiece to the tip of the cutter. The cutting parameters are summarized in Table 1.2.

Table 1. 2 Parameters of the test set-up

Parameter	Value	Unit
Ball end mill, diameter	25.4	mm
Spindle speed	22,000	rpm
Feed rate	5	mm/s
Cutting distance	300	mm
Cutting depth	12.7	mm

Figure 1.2 illustrates the experimental set up. In the test, the cutting resistance forces along the line of feed, F_{cut} and the cutting forces normal to the line of feed, F_{side} were recorded. For cutting normal to the line of feed, the load cell was placed on the side, along the centre line of the workpiece. The experiment was repeated three times for both materials. Although the number of repetition was small and inadequate for significance test, the objective was to obtain a first-hand experience and quantification

of the challenges imposed by the current technique in machining expanded polystyrene for moulding.

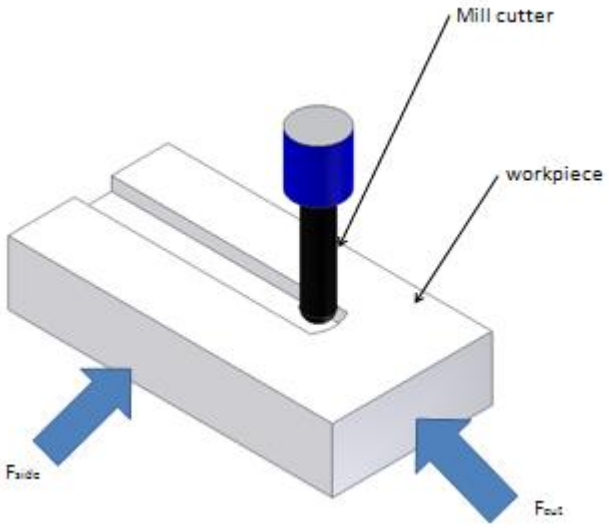

Figure 1. 2 Experimental set up

The cutting work, W_{cut} (N-m) along the line of cut was calculated. The W_{cut} is the product of the cutting force F_{cut} (N) along the feed direction to the distance that the cutter had travelled D (m) (Eq. 1.1):

$$W_{cut} = F_{cut} \cdot D \qquad \text{(Eq. 1.1)}$$

The maximum energy of the cutter along the line of cut was also calculated based on the relationship of the rated electrical values of the motor multiplied by the time, t required to complete the (Eq. 1.2), where E_{max} is the maximum energy, V_{rated} is the

rated voltage of the motor, and I_{rated} is the rated maximum current that the motor could sustain.

$$E_{\max} = V_{rated} \cdot I_{rated} \cdot t \qquad \text{(Eq. 1.2)}$$

If the feed speed and the distance of cut were controlled, the time t in Eq. 1.2 can be replaced with the feed speed, $v_{feedrate}$ and cutting distance, d relationship (Eq. 1.3).

$$E_{\max} = V_{rated} \cdot I_{rated} \cdot \frac{d}{v_{feedrate}} \qquad \text{(Eq. 1.3)}$$

Since the motor that actuated the spindle was rated at 2 kW, the maximum energy that the motor was capable of was 2 kW-min. The ratio of work to the maximum energy available was calculated by dividing the actual work to the theoretical energy. This ratio determined the percent consumption of the energy.

1.2.3 Results and Preliminary Discussion

Table 1.3 shows the mean cutting forces as measured along the feed and the side of the workpiece. For expanded polystyrene, the mean cutting force was 8.41 N, while the side force was 6.16 N. For medium density board, the mean cutting force was 33.53 N, while the lateral force was 32.04 N. In comparison, the force for cutting medium density board along the feed direction was nearly four times greater than expanded polystyrene. On the side, the cutting force for medium density fibre was nearly six times greater than expanded polystyrene. The difference in cutting force

resistance was due to the densities of the workpiece. Under constant feed rate, the average cutting force along the feed was greater than the side force in expanded polystyrene. The average cutting forces along the feed direction were slightly greater than the forces along the side for medium density board. Work done on the medium density board was 0.90% of the maximum energy available from the motor and 0.25% for expanded polystyrene. In reference to the medium density board, cutting expanded polystyrene consumed 35% less energy. This confirmed that the BAC robotic CNC machine was designed to function as a generic machining facility, whereas emphasis was given to deal with high density material such as a wood fibre board. If a cutting system dedicated to expanded polystyrene was to be designed, the machine will require a motor with power less than 2 kW (as of the current motor) to actuate the cutter. This will lead to weight saving in the overall design of the machine.

Table 1. 3 Mean cutting forces, work and Work/Energy ratio

Material	Mean Force, N		Work, N-m	Work/Energy, %
	Feed	Side		
Expanded polystyrene	8.41	5.16	2.52	0.25
Medium density fibre	33.53	32.04	8.95	0.90

Additional observation revealed that the excess materials had turned into fine particles completely. Since the volume of the excess material was related to the cross section of the cutter, the depth of cut and the length of cut; the mass of the excess was nearly 7 grams, which came from a cutting volume of 96.7 mm^3.

1.3 Implication

Generic CNC mill machines were designed to work with a wide range of material hardness. While there were many design factors involved in sizing the motor, the primary objective of installing a high-powered motor in generic CNC machine was to enable the cutter to machine high hardness materials such as woods and metals.

While this observation was brief, it was intended as a practical review of the conventional machining practice. The simple experiments had provided an insight to the divergence of cutting forces involved in machining expanded polystyrene and medium density fibre board. Even without measuring the cutting forces, machinists can feel that the cutting forces on expanded polystyrene were smaller compared to the medium density board, due to the fact that the medium density board had greater mass density. Upon measurement of the cutting resistance force, the values confirmed and provided a clearer indication on the level of differences between the two materials. As shown in Table 1.3, the mean cutting force of expanded polystyrene was about a fifth of that of medium density board.

In milling expanded polystyrene, excess material along the cutter path had turned to fine particles. The excess could easily clog machine components, tedious to clean, had no economic value and could not be reused. These were considered as major drawbacks by the manufacturing house.

Currently, the CNC milling machine is the only viable option for the industry when complex shaping is required. If a machine is dedicated for machining expanded polystyrene, an alternative cutting approach is sought. While the cutting approach is one of the issues, there are other questions that require thorough investigation, such as the machine configuration and method of driving the tool. In developing a feasible machining concept, these questions are interrelated and required researches that are concurrent, rather than a clear progression from one issue to another.

1.4 Chapter Organization

In this chapter, the background that motivates this research is presented. A practical review is also presented that serves as the basis of the problems that are highlighted by the industry. The rest of the chapters are organized as follows:

Chapter 2: This chapter reviews the current issues that are stressed out in the design of a cutting machine. The critical issues are identified and developed into the research objectives.

Chapter 3: This chapter reviews and considers alternative cutting based on slicing. The fundamental of slicing is reviewed. The term “soft solid” for expanded polystyrene is also defined. The influence of cutter geometry, such as straight versus curved edges is also investigated.

Chapter 4: This chapter describes the design of an optical transducer based on direct pattern mapping. The objective is to use the transducer for feedback control of the slider on the oversize machine, where the slider is to be the prime mover for placement of the cutter within the design workspace.

Chapter 5: This chapter concentrates on the work done to establish a mechanical framework for an oversize cutting machine. Attention is focussed on the development of a design for light weight. While the effect of beam geometry is reviewed, a direct drive assembly for actuating long travel slider is also developed.

Chapter 6: This chapter concludes the works from the previous chapter and proposed a future direction for further work.

Chapter 2

Literature Review and Objectives

In chapter 1, the background of the research has been explained. There are a number of interlocking issues but the critical factors are the cutting approach, the method of controlling precise movement that includes sensing capability, and the overall design of the machine. This chapter reviews the current methods in order to develop the directions of the research.

2.1 Cutting Oversize Moulds in Polystyrene

In order to replicate the shape of an oversize part, a large mould made of expanded polystyrene must be machined to the design specification. A familiar alternative to milling is using a hot wire cutter. Figure 2.1 shows the basic construction of a hotwire cutter. There is a frame for holding the wire from one end to another. One end of the wire is attached to a positive source of an electrical voltage supply, while the other is connected to the ground, thus forming a close loop circuit. Upon activation, electrical current flows through the wire and develops heat. When the cutter and the foam are in contact, small areas on the foam are vaporised along the cutting line. Hence the excess material is removed as the wire is fed into the polystyrene block. Typical materials for wires are steel, tungsten or nichrome (Gallina, 2006). Metal wires are favoured because they could sustain extreme heat and use repeatedly. During cutting process,

the wire could be heated up to 700 ^{o}C (Ahn et al., 2003). The diameter of the wire can be as small as a quarter of a millimetre.

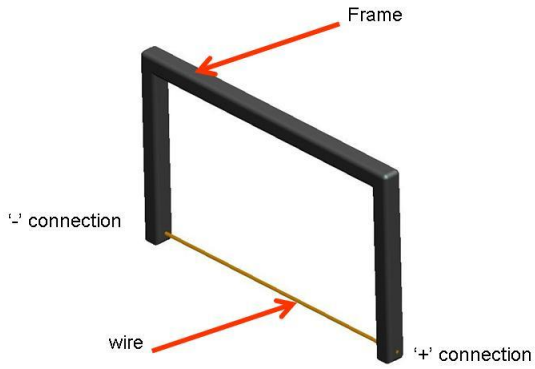

Figure 2. 1 Basic construction of a hot wire cutter.

One of the advantages of cutting with hot wires is the appearance of a smooth cutting surface. At slow cutting feed rates, cutting resistance is absent. Its magnitude rises as the cutting feed speed is increased. Wires made of steel, tungsten and nichrome start developing higher cutting resistance force when they are fed at a speed of three to four mm/s (Gallina, 2006). This is the limit where physical contact is detected. At feed speeds higher than four mm/s, the hot wire is unable to ablate the cutting line before making a contact. Thus, the wire strikes the workpiece. The impact of the strike causes the cutting line to curl along the axis normal to the feed direction. As the cutting force resistance developed gradually due to contact, the wire is in the state of a higher tension than the pre-set value. For precise machining with hot wire, it is crucial

to maintain the wire in tension. Fundamentally, a wire as long as five metres will also sag under its own load.

The concept applied in hot wire cutters relies on vaporization because the material is separated by means of vaporization rather than through physical contact. Expanding this idea, the hot wire can be stretched or pre-formed into a cutting tool with any desired geometry. The smaller tool can be manipulated by a robotic arm. (Posthuma, 2007)

Kim et al., (2007) designed a hot rod that functioned like a ball end mill. Instead of spinning like a conventional mill head, the hot tool was fixed to a chuck. The hot rod vaporized the excess materials along the cutting path. During operation, molten foam formed a layer of thick crust on the machined surface. The maximum feed rate was tested at 50 mm/s. Under this feed speed, the hot tool could complete a given task eight times faster than a commercial five-axis mill cutter head. Additionally, the hot tool is compatible with commercially available tool-path generation software.

The pre-formed wires and the hot rod could emulate milling machine in order to produce a three dimensional feature on a polystyrene block. However, the effect of irritating fumes released from the vaporization could produce an unpleasant working environment. This issue was not being addressed clearly in the literatures (Kim et al., 2007; Posthuma 2007). In machining an oversize mould, more fumes could be released due to contact on wider surface.

An independent foam cutter manufacturer, ROMOCUT, designed a novel cutter head that resembled a mill end. The cutter was designed to cut along the tip, while the central section of the cutter head was hollow. This section was connected to a vacuum suction hose. Although the cutter was shown to perform satisfactorily, just as a normal mill cutter head, the tool needed a high-powered motor in order to actuate the spindle at high rotational velocity. Therefore, the mass of the actuator was substantial. In fact, the actuator was attached to a robotic arm that was placed firmly on the floor. Hence, the tool had limited reach, unless the arm assembly was manually adjusted to machine the other sections.

2.2 Transducer for Long Travel

While the cutting outcome is influenced by the type of cutters, the precision in cutting depends on the capability of the positioning system. The precision in positioning in a cutting machine relies on the capability of the transducer for feedback and control (Seco et al., 2004). The most significant component in a positioning control transducer is the sensing element. However, the cost of applying such a sensor increases with finer precision and greater measurement range (Webster, 1999).

From origins that were mechanical, the design of linear motion transducers has evolved into methods that are electronically based. One of the motivations was the demand of the industry to have a non-contact device that was free from wear and tear. Electronic sensors also have the ability to track movement to a higher degree of resolution. This trait is beneficial for applications that require tight tolerances.

Assembly of semiconductor devices, for example is done at sub-micron tolerance (Giam et al., 2007). This could be achieved if the sensor that controls the placement of the tool has the degree of resolution that matches the assembly tolerances.

Advances in microprocessor technology have benefited the area of motion control. Due to tighter requirement in the dimensional tolerance of a product, the technology in sensing devices has changed from analogue to fully digital control. One of the advantages of digital control is the reduction of the number of sensors. In some cases, no additional sensors are used at all. Instead, movement is estimated based on logic. The sensor-less approach was motivated by the need to reduce cost. However, the measurement accuracy was not as precise as using a sensor. Sensor-less approaches are mostly applied in the control of the rotational speed of a motor for applications that does not need precise linear motion control (Amano et al., 2003; Santiago-Perez et al., 2008; Petrovic et al., 2009).

The sensor and processor can be mounted in a single or in separate housings. The decision depends on the application. The advantage of a single unit is size (Ekekwe et al., 2008). This is beneficial in miniaturised medical robotics (Carr et al., 2009). However, the cost to integrate numerous systems into a compact unit is high for oversize machining application.

All electronic based transducers measure displacement based on the difference between two TTL voltage pulses. Techniques to produce the pulses vary significantly from one type of sensor to another. Different technique also produces different level

of resolution. The technology for positioning sensor can be grouped into three, which are laser interferometer, magnetic and optical (Seco et al., 2005). Laser interferometer is based on phase modulation of light (Wang et al., 2001). Laser is beamed towards a beam splitter, which later deflects the laser to two cubic prisms. The deflected light causes interference pattern because of the difference in the path length from the two cubic prisms. Displacement of an object is measured from the split rays (Luo et al., 2004). In magnetostrictive measurement, the technology manipulates the polarity in magnetic field to create a differential in TTL voltage pulses. While in optical sensor design, the alternating blockage of light transmission from the source to the phototransistor creates the pulses (Nyce, 2004).

A nano-scale level of resolution could be achieved with a laser interferometer. However, the cost of development for a laser interferometer based sensor is on the upper extreme side for a small and medium industry. Magnetostrictive and optical methods on the other hand could cost less. In fact both magnetostrictive and optical could achieve a resolution within microns. Between magnetic and optical, the components for sensing the phase difference is much simpler and reliable with optical.

2.3 Design of a Machine for Oversize Cutting

Since oversize parts require a large machine to drive the cutter head, the design configuration for optimum tool reach, while minimizing loads on the structural members, are two of the major challenges that often affect the cost of developing such

a machine, especially when there is a requirement for accuracy in tool placement. In the design for optimum tool reach, one of the primary factors to be considered is the workspace volume. At the basic level, the workspace can be described according to the coordinate system, namely Cartesian, cylindrical, polar and articulate.

A machine designed to conform to a certain coordinate has distinct features built at the joint. A Cartesian type configuration has all prismatic joints that allow linear sliding. Conversely, an articulate configuration has all revolute joints that only permit rotation. Cylindrical and polar are hybrids of Cartesian and linear articulation. A revolute configuration has the greatest reach in three-dimensional space and the workspace that it could cover forms a full sphere. However, if the task requires high placement accuracy, the most suitable candidate should be based on Cartesian axes, because in this configuration, the machine can be designed to have greater stiffness (Sciavicco and Siciliano, 1996; Kondo and Ting, 1999).

Depending on the work objective, it is possible to integrate more than one configuration into a system. The Cartesian type works best for the base, where high structural integrity can be built. Adding articulated axes to system allow the tool reach to be more flexible. Indeed a number of Cartesian based machines have been designed for fabric trimming (Amin-Nejad et al., 2003) and circuit assembly (Giam et al., 2007). These applications demanded accuracy of placement at micron level.

While the machine configuration provides the ability of a device to work in three-dimensional space, cables are the primary source of relaying powers to the actuators

and to link transducers that control motions of the joint to the master controller. From mechanical design standpoint, cables and wires are extra burden to the system (Golnabi, 2003). In fact, cables require restrainers to prevent them getting tangled with other cables when the joints are moving. If a high-powered motor such as a three phase motor is used, the cables for linking are also bigger and heavier. In addition, the cost of installing and troubleshooting cables is escalating (Apneseth et al., 2003).

2.3 Objectives

Efficient machining relies on specific cutting approach, whereas the mechanical framework is built to realize the cutting concept. For precise positioning, the transducer capability also affects the system considerably. Therefore, the following objectives are developed:

- To study an alternative cutting method on expanded polystyrene for fast and efficient cutting
- To develop a new design of transducer for long travel positioning control that is cost effective for small and medium industry
- To propose the optimum design configuration of a large machine for making oversize moulds

Chapter 3

Characteristics and Force of Slicing in Polystyrene

3.1 Introduction

The primary objective in machining is to generate an object that confirms to the design specification from a raw block. As observed in Chapter 1, a milling cutter shatters the waste material. Cutting by slicing also separates the waste material from the product just as in milling. However instead of turning the excess material into debris along the cutter path, slicing separates both parts physically by creating a controlled fracture, which lowers down the cutting resistance force, while the excess material might also be reused.

Major issues in machining have always revolved around the speed of developing a shape or feature and the cutting force requirements. The combination of high cutting speed and lower cutting force is usually favoured (Kim et al., 2007). For machining expanded polystyrene, obtaining a manageable excess part is also a concerned, because from the industry experience, the excess part has low economic value as fine particles, which are also tedious to clean and requires hours of downtime for

maintenance of the machining facility. Therefore, this chapter studies an alternative cutting method of expanded polystyrene by means of slicing.

3.2 Fundamentals of Slicing

Slicing usually is applied in food processing, on materials such as meat and cheese (McGorry et al., 2003; Brown et al., 2005). Sculpture artists also used this method for carving woods and foams. Manufacturing industry applied slicing in bandsaw or rotary saw for cutting metal sheets (Malkocoglu and Odzemir, 2006). In manufacturing, slicing is usually limited to cutting of parts to small pieces rather than shaping.

In defining materials, there are hard and soft solids. However, the classification is ambiguous. Typical examples of soft solids are meat, elastomers and polymer gels. Soft solids could be defined as materials that have a modulus of elasticity within sub Mega-Pascal unit (Rey, 2005). Another opinion suggested that the distinction between soft or hard solids could be easily observed through the condition of the off-cuts, such that, the off-cuts of a soft solid would appear as ‘floppy’ and does not bind the cutter as cutting is progressing (Atkins et al., 2004; Williams, 1998). The non-binding condition provides relatively low cutting force resistance for a given feed rate.

In the manufacturing of fibre reinforced plastic (FRP) components, moulds made of expanded polystyrene are preferred because of low cost of procurement. The polystyrene block has adequate strength for machining, and the off-cuts appear as

floppy. In this research, the definition of Atkins et al. (2004) and Williams (1998) is applied. Thus, expanded polystyrene is treated as a soft solid.

Slicing combines the actions of deforming a workpiece through tension-compression and shear directions. Thus, the slicing method cuts a workpiece with a lower cutting force than pushing alone (Atkins, 2006; Williams, 1998). Tools for slicing include straight blades, curved blades and disk blades, while the cutting edge could be smooth or serrated. The mechanics of slicing is similar regardless of the blade types, but the action varies (Frazetta, 1988). In one pass, a straight blade has wider cutting line than a disk cutter. However, a disk cutter has a consistent slicing angle in both clockwise and counter clockwise directions.

3.2.1 Pushing

Williams (1998) illustrated pushing by using a wedge that was pressed into the material (Figure 3.1). There are several parameters involved. On the wedge, there is an angle α that defines the angular distance between the upper edges of the wedge to the horizontal plane of the entry. There is also an angle β, which is the angular distance between the bottom edges of the wedge to the surface of the cut material. The angle β is also known as the relief angle. If $\beta = 0$, the bottom edge has a friction due to contact with the surface of the cut section. The force that pushes the wedge is the cutting force F_{cut}. This force is applied along the horizontal plane. While the wedge is pushed into the material, another force acting normal to the horizontal plane is also applied, P, that pushes the excess away from the remaining material. On the material side, there is a resistance force K that was acting normal to the top edge of the wedge.

The displacement of the push force is *dv*. On the material side, there is also a displacement, *da*, which is the displacement at which a crack is developing due to the advancement of the wedge. Summing all the forces in horizontal direction (or the direction of push), the interaction of these forces is shown in Eq. 3.1:

$$F_{cut} = K(\sin\alpha + \mu\cos\alpha) + \mu P \qquad \text{(Eq. 3.1)}$$

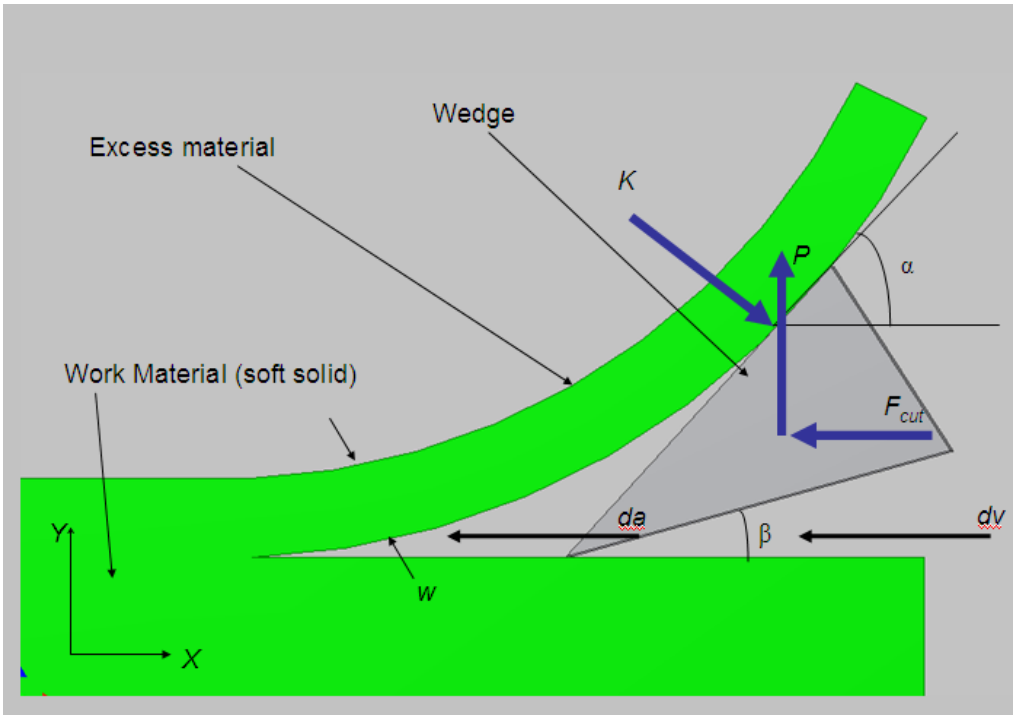

Figure 3. 1 Forces reaction as a soft material is cut through push action based on a simple wedge (Williams, 1998).

The effect of μP is included if β = 0, where μ is the constant of friction (μ=0; smooth, zero friction: μ=1: sticky, maximum friction). As shown in Figure 3.1 and Eq. 3.1, in soft solid, the excess material is assumed to be floppy. Therefore, while the

excess portion is increasing as the wedge is pushed deeper; its mass does not bind the cutter as the bending moment can be neglected. This is of course reducing the resistance due to contact friction.

Whilst Williams (1998) looked at the factor of geometry, Atkins et al., (2004) focussed on the cutting resistance due to the properties of the material. Back to Eq. 3.1, the resistance force K is broken down into several components. K is a function of the material toughness, R, multiplied by the thickness of the excess material, w, and the ratio between the displacement of the cut, da to the displacement of the wedge being push, dv (Eq. 3.2):

$$K = R \cdot w \cdot \frac{da}{dv} \qquad \text{(Eq. 3.2)}$$

Atkins et al., (2004) also included another force, the friction force, f , which acted along the length of the cutting edge. This friction force, f is a function of the shear yield strength τ_{sy}, multiplied by the length, L of edge of the wedge which is in direct contact to the material. A factor, m is also included in the equation, whereas m is the sticky factor of the material. The value for m is from 0 to 1. An 'm' value of one indicates the material is very sticky, where the sticky factor is proportionally related to friction. A side constant, C is also included. The value of C=2 implies that both sides of the edge are in contact with the material. Therefore, the friction force, f is depicted in Eq. 3.3:

$$f = C \cdot L \cdot m \cdot \tau_{sy} \qquad \text{(Eq. 3.3)}$$

Based on Williams (1998) and Atkins et al., (2004), this chapter expands Eq. 3.1, to include the material effect and the friction along the cutting edge (Eq. 3.4). Hence, when only pushing is considered, the magnitude F_{cut} must be large enough to overcome the material fracture toughness, frictions along the edges, and friction along the sides of the cutter that is in contact with the material.

$$F_{cut} = \left[R \cdot w \cdot \frac{da}{dv} \right] (\sin\alpha + \mu\cos\alpha) + \mu P + \left[C \cdot L \cdot m \cdot \tau_{sy} \right] \qquad \text{(Eq. 3.4)}$$

3.2.2 Sideways Movement

In pushing mode, the cutting force resistance depends entirely on the push force. When a slight sideways movement is introduced, the actual cutting force becomes the resultant of push and sideway forces (Eq. 3.5). The sideways movement is defined as the secondary vector component that produces a resultant cutting movement which is at an angle from the push direction. This action lowers the magnitude of the cutting force along push direction.

$$F_{res} = \sqrt{F_{cut}^2 + F_{side}^2} \qquad \text{(Eq. 3.5)}$$

Figure 3.2 shows the isometric view of Figure 3.1, where all the conditions are maintained, only a sideway motion is now introduced. The sideway force is F_{side}. Displacement along the sideway direction is *ds*. Here, it is assumed that the sideway motion is parallel along the Z-axis. The interaction between the push and sideway forces is called the slice/push ratio.

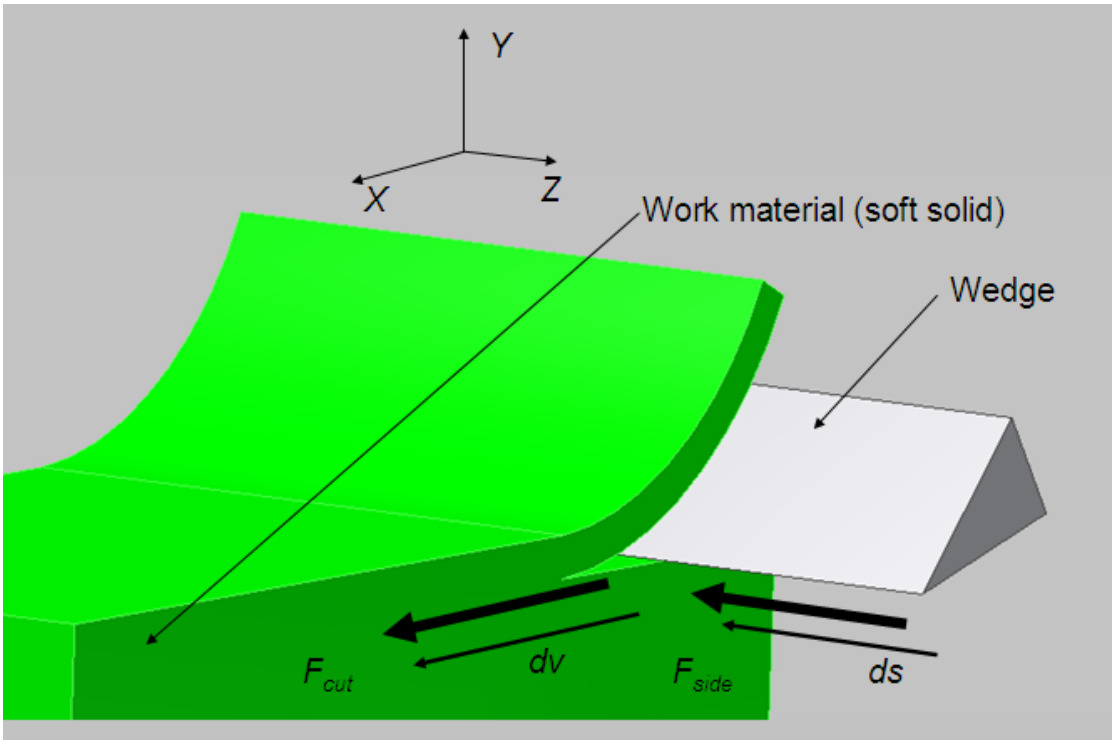

Figure 3. 2 Addition of sideways motion in the cutting process

Atkins et al., (2004) defined the slice/push ratio as the ratio between the displacements in sideways direction, *ds*, to the push direction, *dv* (Eq. 3.6):

$$\varepsilon = \frac{ds}{dv} \qquad \text{(Eq. 3.6)}$$

Although the sideway force takes over some load from pushing force as shown in Eq. 3.6, there are actually limits that needs to be taken into consideration. For instance, the sideway force could be absent, and with only pushing force, the material can still be cut - *pushing*. The situation is not true if the role is reversed, because cutting cannot be achieved without the push force. Without the push force, the cutter could not penetrate the material. Therefore, the function of the sideways movement is only to reduce the cutting force needed in the push direction due to the presence of shear deformation along the line. The sideways component of force cannot perform cutting on its own. Slicing can only occur whenever both the pushing and the sideways force components are present.

3.2.3 Curved blades

Blades could be straight or curved. Although the fundamental of cutting is the same regardless of blades, the variation in geometry causes the behaviour of the cutting force to differ slightly.

In Atkins (2006) a general form of curved blades was presented. The blade was assumed to have a variable curvature. The pivot point is not fixed; instead it varies along the axis of the curvature at a particular instantaneous point. This is actually a generic form for any curved blades including disk blades. The major difference between a generic curved blades and a disk blade is on the pivot, whereas a disk blade has a fixed pivot point, the generic one assumes that the pivot point varies according to the radius of the curvature. Consider a generic curved blade and assuming that

point *P*, is the point of contact, there are several parameters governing the cut (Figure 3.3). The true horizontal axis is *X*, and the true vertical axis is *Y*. Point *O*, is the origin of the true axes. The angular distance of point *P* to the pivot point, *O* is θ. The distance of point P to pivot *O* is *r*. At point *P* and because of slicing motion, angular distance of the axis of the sideways force, F_{side} to the line *r* is φ. The cutting force, F_{cut} is normal to F_{side}. As such the displacement of feed of *s* and *v* follows the axis of the forces respectively. At point *P*, there are also two feed directions due to circumferential effect, v_c and radial effect, v_r, with respect to *O*.

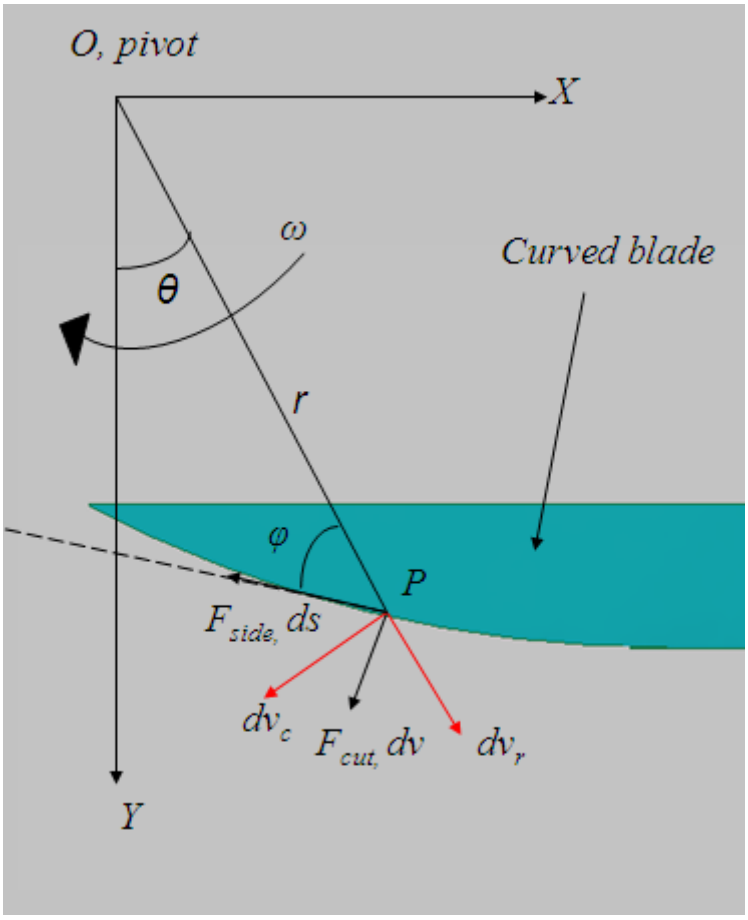

Figure 3. 3 Forces interaction in generic curved blades (Atkins et al., 2004).

From the pivot point, *O* to point *P*, the angular speed for the slicing motion is ω. Therefore, at point *P*, the corresponding feed rate due to circumferential effect is *r* multiplied by ω (Eq. 3.7):

$$\frac{dv_c}{dt} = r \cdot \omega \qquad \text{(Eq. 3.7)}$$

Likewise, the associate feed rate due to the radial effect is ω multiplied by the differential of radius, *dr* with respect to the rate of change of the angle θ (Eq. 3.8):

$$\frac{dv_r}{dt} = \frac{dr}{dt} = (\frac{dr}{d\theta} \cdot \frac{d\theta}{dt}) = \omega \cdot \frac{dr}{d\theta} \qquad \text{(Eq. 3.8)}$$

The actual feed rate along F_{cut} and F_{side} should comprise of the feed rate components along the circumference and the radial direction with respect to the pivot (Eq. 3.9 and Eq. 3.10):

$$\frac{dv}{dt} = \frac{dv_c}{dt}\cos\varphi + \frac{dv_r}{dt}\sin\varphi \qquad \text{(Eq. 3.9)}$$

$$\frac{ds}{dt} = \frac{dv_c}{dt}\cos\varphi - \frac{dv_r}{dt}\sin\varphi \qquad \text{(Eq. 3.10)}$$

Because the curvature of the edge forms an arc, the length of the arc is the sector length of the curve with respect to *O* (Eq. 3,11):

$$ds = d\theta\sqrt{r^2 + (\frac{dr}{d\theta})^2} \qquad \text{(Eq. 3.11)}$$

This chapter expands the description of cutting force in Eq. 3.4, whereas the cutting force, acting along the push direction is, with arc length *S*, replacing the straight line, *L* (Eq.3.12).

$$F_{cut} = \left[R \cdot w \cdot \frac{ds}{dv} \right](\sin\alpha + \mu\cos\alpha) + \mu P + \left[C \cdot S \cdot m \cdot \tau_{sy} \right] \qquad \text{(Eq. 3.12)}$$

3.2.4 Serrated edge

In section 3.2.1 to 3.2.3, the assumption is based on smooth edge. In serrated edge, there are teeth along the edges. The presence of teeth along the edge allows the blade to sink deeper into the material, thus preventing the cutting edge to slip. Although the material has not been deformed yet, the surface of the material is prone to damage or 'pre-deformation' because of the sinkage. In manufacturing, serrated blades are often applied in sawing, such as band-sawing and circular sawing on hard solids. (Sarwar et al., 2009)

A number of factors are affecting the performance of serrated blades: (1) the pitch of the teeth (2) the depth of the teeth and (3) the rake angle of the teeth. A large depth however binds the teeth to the material and thus increasing the slicing force. A high

frequency in tooth pitch resembles smooth edge, which diminishes the advantage of pre-deformation. A rake angle that favours one of the sides would have lower cutting force along the parallel sideways direction, but experience higher cutting force on the opposite side. (Frazzeta, 1988)

Because of pre-deformation, serrated edge blade produced fine particles as by-products of the excess. Therefore, this type of blade was not considered further. However, preliminary test was included to justify the study.

3.3 Materials and Methods

In section 3.2, the fundamental of slicing was discussed through the geometric relationship. There was a need for a study on the characteristics of cutting in order to select the optimum cutter design for moulding. Hence, the characteristics of slicing polystyrene were studied in two forms. The first test was a qualitative exercise based on several blade designs. The second test was a quantitative exercise that aimed at recognizing the trend of cutting forces on polystyrene based on disk cutters.

3.3.1 Carving

The qualitative exercise was completed by three subjects. Each was assigned to carve a polystyrene block. The objective was to create the appearance of the *table top* on the raw polystyrene block. On side note, the *table top* is a distinctive landmark in Toowoomba. Originally a volcano, the top of the hill appears as a flat field, hence the name *table top*. On the blade types, both smooth and serrated types were used. The

serrated type was a powered hand saw that oscillated at a speed of 115 RPM. The blades are shown in figure 3.4.

Figure 3. 4 Blades for carving exercise (a) common straight blade with smooth edge (b) Power hand saw (serrated edge)

A high density polystyrene block was manually carved with these blades. In carving, a set of rules was followed. First, the blade was held orthogonally along the direction of feed. Then, the blade was pushed into the material. Second, the blade was held at an angle along the direction of feed. Then, the blade was pushed into the material. For the first and second rules the power in powered saw was not in used. Third, the blade was held orthogonally, just as in the first test. Then, the blade cut with push and shear movements. Forth, the blade was held at an angle, just as the second test. Next, the blade cut with push and shear movements. Figure 3.5 shows a sample of raw high density polystyrene block. The grain is rough, but the material is solid.

Figure 3. 5 Surface of a raw high density expanded polystyrene

A number disk type cutters were fabricated (Figure 3.6). Some were made from thin metals, while some were made from thick stainless steel. Some disks were fabricated with grooves. In figure 3.6, the solid thin disk (D3) is a fabric cutter, with 0.125 mm thickness, while the bevel up (D1) and down (D2) disks were fabricated from a three millimetres thick stainless steel. The bevel up (D1) and down (D2) disks had a rake angle of 15^{o} (Figure 3.7). All disks were attached to a hand powered drill, set at maximum spindle of 580 RPM.

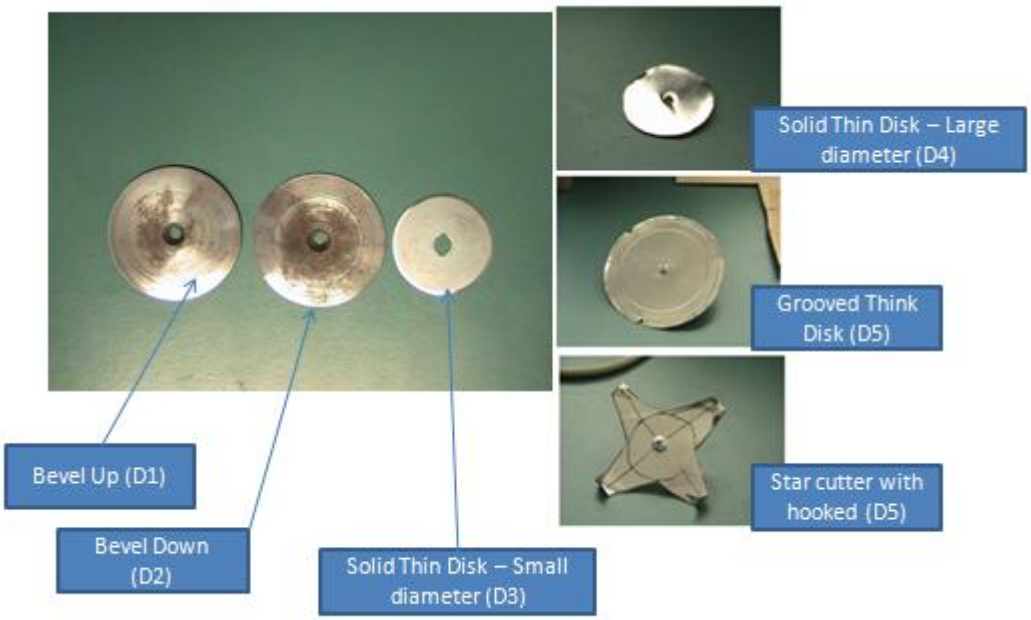

Figure 3. 6 Various types of disk blades

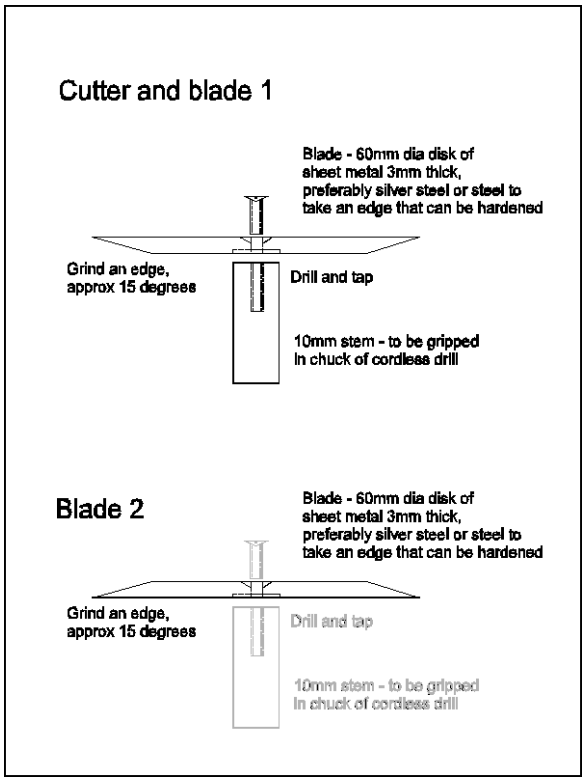

Figure 3. 7 Design notes for D1 and D2

3.3.2 Cutting Force Based on Disk Cutter

In section 3.3.1, the various types of cutters were tested, whereas the interest was mainly on the surface condition after cutting. Having established that a thin disk type cutter was an applicable candidate for precise machining, this section studied the trend of the cutting force resistance. The thin disk blade (D3) as described previously was used. The test specimen was a high-density polystyrene block, 450 mm x 200 mm x 200 mm. For testing, the specimen was held firmly on a sliding platform, designed in chapter 5 for direct drive-direct power concept (Figure 3.12). A load cell was installed at the connection link between the platform and the track. Prior to cut, the load cell was pretension to 25 N. In this test, the cutter was creating a straight line cut, where the cut was measured starting from the entry to the exit planes along the longitudinal direction of the specimen. Therefore, the total cutting length was 450 mm. There were two types of cutting directions. Firstly, the disk was slicing in clockwise rotation. Secondly, the disk was slicing in anti-clockwise rotation. In clockwise rotation, the disk was rolled-in in order to slice the specimen, while in anti-clockwise; the disk was rolled-out. Because the contact between the metal blade and the polystyrene would eventually increase the temperature of the blade due to friction, subsequent cut was completed after a five minutes rest, so that the metal blade would be allowed to cool down. The disk blade was set to spin at the fastest rotation, at 580 RPM.

Figure 3. 8 Test set-up for cutting force resistance on powered disk blades

As the slicing tool was fed into the test block, the corresponding force resistance was recorded in a video camera. The video data was originally in VOB format, but converted to WMV format using *Video Wave 9 - Roxio Easy Media Creator* video editor. The cutting operations in the video were visually inspected for completeness. For analysis, only a complete cut was chosen. Next, the video data was extracted frame by frame at an interval of 30 frames per seconds using *SC Video Compiler* software. This allowed the movement to be captured at 33.33 kHz. The extracted frames were stored in Bitmaps and the average speed of cutting (feed speed) was derived from the frame count. Each frame was analysed for maximum cutting resistance. The location where the maximum resistance occurred was also marked and recorded. The feed speed was segregated into three segments based on the duration of

cut. Average slicing speeds of less than 50 mm/s was classified as slow. A slicing speed of 50 mm/s to 70 mm/s was medium. The average slicing speed of more than 70 mm/s was fast. There was over a hundred trials cut, but only 67 were complete. For analysis, the data was grouped into the cutting force. They were analysed with a one-way ANOVA classification.

3.4 Results and Discussion

3.4.1 Carving

Among all the preset rules, pushing alone at orthogonal angle was the hardest for both cutters. Often they were bound and had to be pulled out. However, for the straight blade the push was made easier when the cutter was held at an angle. Even though no sideways movement was introduced, the inclined angle of push behaved as if sideways motion was present. Pushing serrated blades was difficult even at inclination. For slicing with orthogonal or inclined angle, the subject did not feel any significant difference. Figure 3.6 shows the results of carving the *table top* manually on the block, using various blades. Figure 3.7 shows the close-up view of the results in figure 3.6. Upon visual inspection, the carving exercise showed that slicing produced smooth surface. Smooth edge blades produced smoother surface than serrated. The number of passes on a particular feature did not show improvement on the surface.

Figure 3. 9 Results of creating a *table top* on polystyrene using various blades

Figure 3. 10 Closed up view of the results shown is figure 3.6

3.4.2 Force, Torque and Rake Angle

Table 3.1 shows the summary of forces and torques for D1, D2 and D3 for initiating a cut on the expanded polystyrene block. Initial assumption that the rake angle had a considerable effect on slicing was diminished. The result shows that the effect of the overall thickness of the blades was more important. Thicker disk blade such as D1 and D2 would form a wedge situation as described in Eq. 3.1, unless the rake angle was extremely steep, but of course that would either results in a very long diameter disk, or a thin disk, similar to D3. The thick body developed higher friction, even though the sideway force was acting at consistent rate according to the torque provided by the powered hand drill. Therefore, in the design of cutters for slicing, the overall thickness should be minimized.

Table 3. 1 Summary of force and torque for D1, D2 and D3

Disk Types	*Force*	*Torque*
D1	11.70 N	0.35 N-m
D2	11.25 N	0.34 N-m
D3	2.70 N	0.06 N-m

Upon establishment of the effect of thickness and rake angle, thin disks label as D4, D5, and D6 were tested. The cutters were also attached to a hand drill that spun at 580 RPM. The disks would cut the workpiece in one pass only and the surface condition

was observed. Figure 3.10 shows the sample cutting surface created by D4. As observed, the surface is smooth. Figure 3.11 shows the sample cutting surface created by D5. The surface finish is rough. Using D6 disk, the excess turned to debris and surface finish was even worse the raw surface of a block.

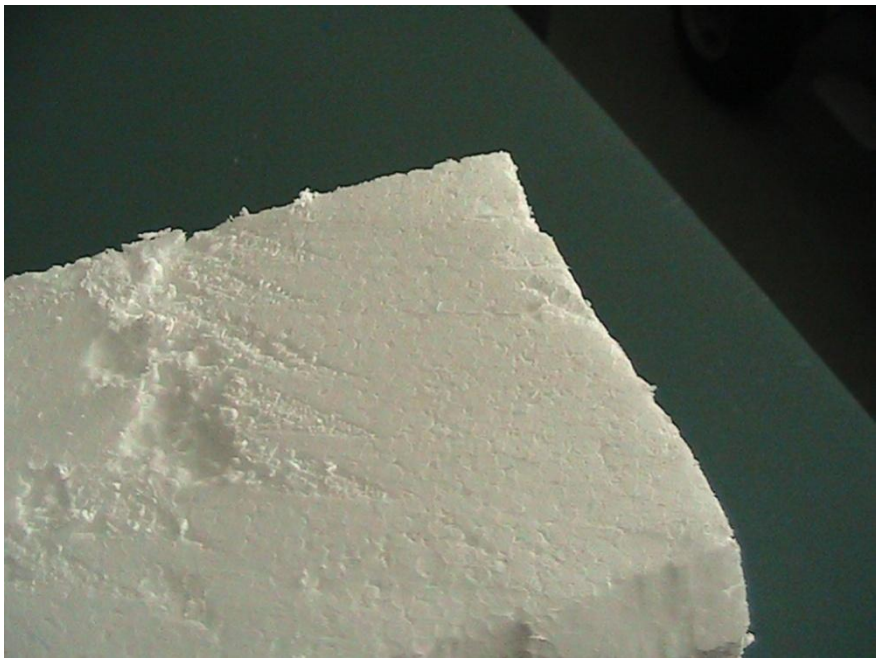

Figure 3. 11 A sample of cutting surface with smooth edge disk

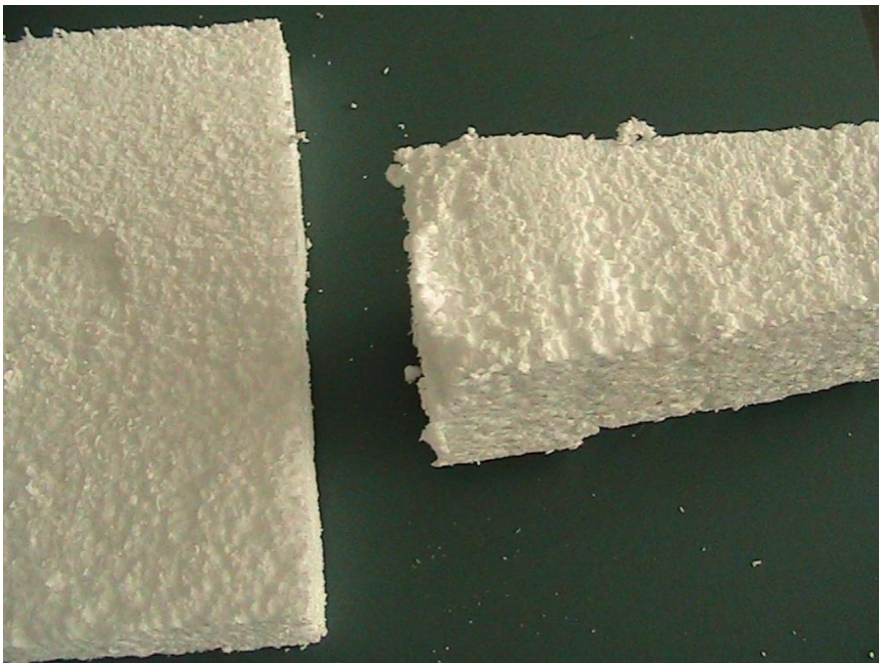

Figure 3. 12 Sample of cutting surfaces with groove edge

3.4.3 Cutting Force on Disk

Using a one-way ANOVA classification at 0.5 and 0.1 probability levels, there was a significant increased in the mean cutting force resistance from low to fast feed speed. (Table 3.2). On the effect of rotational direction of the disk, the one-way ANOVA did not indicate any significant difference (Table 3.3). Higher feed speed tends to develop higher cutting forces. In several attempts for higher speed, more than 100 mm/s, the disk was locked onto the workpiece. This had caused the cutting force to increase significantly, but the cutting was incomplete. Locking was due to undeveloped fracture that diminished the sideways effect as the motor torque was inadequate. Hence, the effort in cutting was diverted to pushing alone. This problem can be resolved with a higher powered motor to provide higher torque.

Table 3. 2 One-way ANOVA for comparison between feed speeds, (1) slow, (2) medium (3) fast

Net

	Sum of Squares	df	Mean Square	F	Sig.
Between Groups	11876.575	2	5938.287	158.747	.000
Within Groups	2394.063	64	37.407		
Total	14270.637	66			

Table 3. 3 One-way ANOVA for comparison between the directions of cutting disks, (1) clockwise (2) counter clockwise

Net

	Sum of Squares	df	Mean Square	F	Sig.
Between Groups	1.220	1	1.220	.006	.941
Within Groups	14269.417	65	219.529		
Total	14270.637	66			

At low feed speed, the mean cutting force was 12.17 N with a standard deviation of 3.178 N. At medium feed speed, the mean cutting force was 26.72 N with a standard deviation of 5.270 N. For the fastest feed speed, the value was 52.12 N and 12.138 N for the mean cutting force and the standard deviation respectively (Table 3.4).

Table 3. 4 Mean and standard deviation at three levels of feed speeds (1) low speed, (2) medium speed, (3) fast speed

Feed	Mean (N)	No. Replication	Std Dev (N)
Low speed	12.17	27	3.178
Medium Speed	26.72	30	5.270
High Speed	52.12	10	12.138

In chapter 1, the mean cutting force of milling expanded polystyrene along the feed direction was recorded at 8.41 N. This magnitude was closer to the result of slicing expanded polystyrene at low speed (12.17 N). However, slicing achieved this at a rotational speed, 3900% lower than milling. Smooth surface appearance is an advantage of slicing, regardless of number of passes. Another advantage of slicing is that, the excess parts are 'chunky' rather than appear as fine particle. The excess is easier to manage and clean up. It is possible for the excess to be reused.

3.5 Summary

This chapter studies the characteristics of slicing as alternative to conventional machining of polystyrene based on milling and hot wire cutting. The definition for soft material was discussed and the definition of Atkins et al., 2004 and Williams et al., 1998 was adapted. The fundamental of slicing was further discussed. The presence of a slice-push ratio that influenced slicing was acknowledged. Blades for slicing could be classified into straight or curved. Disk blade was considered as a subgroup of curved blades, whereas the pivot point of cutting action was rather fixed to an arbitrary point. Thus, disk blades could provide constant slice-push ratio as opposed

to generic curved blades. On the design of the cutter edge, smooth edge produced smoother off-cuts than serrated consistently. Therefore, in order to prevent the excess parts from turning into fine particles, the recommended design was the smooth edge disk type blade. Upon test of cutting force resistance with smooth edge disk type blade, the direction of rotation was not a significant factor; rather the force magnitude was influenced by the feed rate.

Chapter 4

Direct Pattern Encoding for Precise Displacement of Long Travel

4.1 Introduction

Precise machining relies on a computer-controlled system to govern cutter movement. The principal component is a positioning transducer to provide feedback for monitoring and course correction. In order to control position to a desired accuracy, it is essential that the transducer is able to measure displacement consistently for the entire length. It is necessary that the transducer is also affordable (Ekekwe et al., 2008). Using a transducer with these characteristics would result in a high quality product at lesser cost.

In this project, the industrial collaborator desires a machining accuracy of within sub-millimetres. This was translated as a maximum of 100 microns accuracy in tool placement. Because accuracy in movement relies on the capability of the transducer and searching for affordable means of controlling the position is also a prime target, this has motivated the research in a cost effective transducer design.

Chapter 2 has discussed the various technique applied in transducer design. Optical method has been acknowledged as the best candidate when cost is a major concern. The focus of this chapter is on optical sensing technique for precise positioning.

In literatures, a number of optical based sensing methods have been reported (Saito et al., 2009, Carr et al., 2009, and Merry et al., 2009). Some could achieve sub-micron level accuracy (Seco et al., 2005). However, most are relying on complex hardware and components design in order to implement the algorithm (Jasper & Fatikow, 2010). This has caused the transducer to lose its cost-effective appeal. In the making of polystyrene moulds, the requirement for accuracy is less stringent than the assembly process of electronics components. Nevertheless, the emphasis is more on feedback consistency and reliability for long travel movement.

Conventional optical sensing technique uses optical means to generate pulses. The technique to create pulse varies from simply obstructing the light beam, or running an optical sensor diagonally along a series of pattern, which would later be converted into Fourier series (Brier et al., 2007).

This chapter proposed a simplified optical sensing method that interprets the image of a repetitive pattern for displacement determination, rather than creating light pulse. The transducer is designed as an instrument for feedback control of long travel movement. The direct image encoding is applied with a novel communication protocol that defines the command to control and the resolution of the sensor to reach

within sub-pixels positioning accuracy on a grating that is originally a two millimetres scale surveyors tape measure. The transducer is tested on a test rig for evaluation.

4.2 Review of Transducer Design

Conventional approach in dealing with displacement sensing using optical sensors is to perform measurement based on pulse generation. Light interruption generates a series of pulses that appear as a binary sequence. Using a digital processor to receive the signal, motion data such as displacement, velocity, and acceleration are extracted for feedback control (Ekekwe et al., 2008). A typical optical transducer consists of a light source, a grating set to create lights interference, and a photoreceptor or phototransistor (Alejandre and Artes, 2005). The grating set (encoder) could be rotary or linear. Both encoders work on the same principles. The size of a pulse cycle depends on the widths of the opaque and transparent slots. In most design, the slots are equally distributed. However, the ratio of widths of the slots may not necessarily be equal.

4.2.1 Measurement Methods

A simple pulse measurement method could be implemented on an AVR 8-bit microcontroller to capture signal and measure the pulse. The pulse is generated by interrupting light that is beaming on the phototransistor through a rotary encoder. Then, the pulse signal is relayed to the controller input capture feature, which triggers an *Interrupt Service Routine* (ISR). The series of light pulse is segregated into rising or falling edges. Using either of these edges, a variable counter is set to react to the occurrence of successive events. Thus, displacement is a function of the successive

pulse events. If a rotary encoder has an *N* number of opaque slots, and if the opaque and the transparent slots have equal width, a full revolution is *2N*. If a cycle is the gap between two successive events, then the resolution of the sensor is the inverse of the full revolution, which is 1/(2N) revolution. The error of measurement is ± 1/(2N) revolution. This is the simplest measurement method. However, the resolution is dependent upon the grating scales. Hence, the accuracy is low unless the number of slots is increased.

Improvement in the simple count method comes in the form of pulse counting strategy. Ekekwe et al, 2008 classified the methods into two, namely period and frequency counting. By definition, period counting is counting how fast two successive pulse events occurred. In a rotary encoder application for example, the encoder is assembled to the shaft of a motor. As the shaft is rotating, the measured parameter is velocity, in which position and acceleration are derived from. Measured in *RPM*, the velocity of the period, ω_{p} as determined from period counting strategy is a function of the clock frequency of the microcontroller, f_p (Hz) divided by the product of encoder pulse per revolution, m and the final value of the counter, N_p (Eq. 4.1). N_p is a unit less parameter. The value '60' in Eq. 5.1 is the conversion factor of seconds to minutes.

$$\omega_{\mathrm{p}} = \frac{60 \cdot f_p}{m \cdot N_p}(RPM) \qquad \text{(Eq. 4.1)}$$

On frequency counting strategy, the number of pulses, N_f obtained in a constant period, T_f is measured. Here, the velocity, ω_f is also in *RPM*, but N_f is divided with the number of encoder pulse per revolution times T_f (Eq. 4.2). The value '60' in Eq. 5.2 is also the conversion factor of seconds to minutes.

$$\omega_{\mathrm{f}} = \frac{60 \cdot N_f}{m \cdot T_f}(RPM) \qquad \text{(Eq. 4.2)}$$

In frequency counting, a higher frequency count indicates higher speed, while smaller count is the reverse. In both the period and frequency counting, the relative error due to the counter error, δx is estimated based on the difference between the measured value, x_0 to the true value, x (Eq. 4.3).

$$\delta x = \frac{\Delta x}{x} = \frac{x_0 - x}{x} = \frac{x_0}{x} - 1 \qquad \text{(Eq. 4.3)}$$

Substituting Eq. 4.3 with velocity estimation based on period counting (Eq. 4.1), the relative error due to counter error in period counting is shown Eq. 4.4.

$$\frac{\omega_{\mathrm{p}}}{\omega} = \frac{m \cdot \omega}{60 \cdot f_p} \Delta N_p \qquad \text{(Eq. 4.4)}$$

Similarly, for frequency counting, the relative error due to the counter error in period counting is shown (Eq. 4.5):

$$\frac{\omega_{\mathrm{p}}}{\omega} = \frac{60}{m \cdot \omega \cdot T_f} \Delta N_f \qquad \text{(Eq. 4.5)}$$

In Eq. 4.4 and Eq. 5.5, the parameters that are proportional and inversely proportional to the relative errors are different. These are affecting the magnitude of the relative error. In period counting, the relative error would be lower at low speed, but in frequency counting, the role is the other way round.

4.2.2 Phase Manipulation and Codes

Either rotary or linear gratings, the conventional objective is to create at least three signals that were out of phase to each other. The first and second phases are for movement and vector, the third signal is the reference point (Alejandre and Artes, 2005). Mostly, the phases are created based on Moire or Talbot effect pattern (Kao and Lu, 2005). These patterns are aimed at producing the smallest pitch in the oscillating signal. An alternative is to use a grating set that has sub microns pitch scale, thus directly producing high frequency pulses (Merino et al., 2007).

Phase manipulation is heavily influenced by the accuracy of the physical grating. Depending on the pulse measurement strategy, the grating sets are constructed to provide either incremental or absolute codes (encoders). Incremental encoders have the same grating set for the entire length. However, an absolute grating consists of

patterns that are designed to provide distinctive marking for every position. Most absolute encoders apply Gray Codes (Etzion and Peterson, 1996, Hiltgen et al., 1996, Schwartz and Etzion, 1999; Lee and Lee, 1999). A major advantage of an absolute encoder is the ability to distinguished one position to another. Therefore, the transducer does not require specific reference points in order to find the point of origin. However, that also means that the number of absolute codes is dependent upon the resolution and the maximum travelling range. Conversely, an incremental encoder is easier to manage for long travelling range. It is also feasible to generate a high resolution phase differential based on incremental encoder, as demonstrated in Merino et al., (2007) who created a one micron pitch based on lithography technique, and Kao and Luo (2005) who generated a 20 micron pitch grating using Talbot self image technique.

4.2.3 Sensing Element

In most design, a phototransistor is used to capture the light signal. For displacement and vector, there are at least two phototransistors in a transducer. The phototransistor is a type of a single point sensor. There are also optical sensors that are based on photodiodes, such as the linescan, and framescan, which store data within pixel arrays (Figure 4.1).

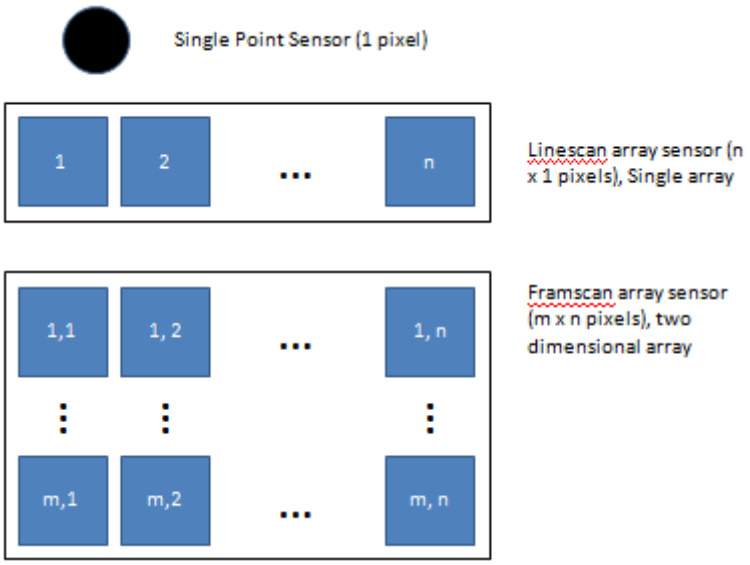

Figure 4. 1 Types of phototransistor arrays

Billingsley (2006) described the characteristics of each sensing elements. A single point sensor had only one photosensitive element, which alternated between on and off once at a time. The single point sensor was suitable for a simple light or dark sensing as in a rotary encoder. A linescan sensor consisted of a series of photodiodes arranged in a single row array. The linescan sensor could scan edges rapidly. Next, a framescan sensor consisted of two-dimensional arrays that formed an area and able to scan the features of an object, in monochrome or in colours. The framescan was suitable for sensing an area and identifying objects in two dimensions.

Brier et al., 2007 applied a linescan camera for positioning control application. For scanning of edges to sub-pixels, the linescan camera was positioned in a way that the captured image would be diagonal, and thus producing two out of phase oscillating waveforms. The waveforms were processed using a Fast Fourier Transform (FFT)

algorithm to distinguish the peak of the harmonics in order to obtain sub-pixels measurement. Then the peaks were utilized as pulse signals for displacement measurement.

On the surface, the linescan and the framescan are similar. The major difference is only on the arrangement of the arrays.

In a characteristics comparison test, Li et al., (1988) compared the performance of the linescan and the framescan cameras in an object inspection operation. The results showed that, the framescan camera had higher time interval to relay the data from the pixel elements to the processor. The results indicated that the framescan was suitable for object inspection where speed was not a major concern. In contrast, the linescan camera had a shorter processing interval and was recommended for inspecting fast moving objects.

4.2.4 Illumination

The effect of illumination is significant in optical transducer because the entire system relies on the presence of light. Lights can be of types that vary from visible to invisible spectrums. Infrared was normally chosen due to high energy emittance. Halogen lamps could provide brighter illumination on the gratings. However, the halogen lamps also produced heat, draws high amount of current and energy inefficient. On florescent lamp, flickers might interfere with the generated image, whereas inconsistent illumination would introduce false pattern recognition.

Houghton (2002) suggested LEDs, which produced constant lights without excessive heat.

The design for illumination could be direct or reflective. In direct illumination, the light source is facing the sensor, and a grating scale is placed in between them (Alejandre and Altes, 2007). In this arrangement, the level of illumination is optimized and worked best if the grating scale is made from a transparent material. However, this method consumes the most space for installation. In reflective illumination, light is reflected to a surface, then the reflection penetrated layers of grating scale before reaching the sensor (Kao and Lu, 2005; Merino et al., 2007).

4.2.5 Positioning Control in Machining

The main function of a transducer is to provide motion variables, particularly position, velocity, and acceleration. The variables data is feedback into the controller system for course correction. Control algorithms define the control strategy for an operation that required precise movement.

Different applications required different control strategy. In feedback control, the error of the measured parameters was looped back to the system. The proportional-integral-derivative PID controller was an example of such a strategy. It was also one of the most widely used methods. Other techniques were often compared with PID for performance verification. (Giam, 2007)

Since real control problems must deal with nonlinearities, such as the dynamic uncertainties and friction, controls with feedback are applied with adaptive or optimal methods (Sencer et al., 2008; Perez et al., 2007). Sliding modes control is also included in order to reduce the error of positioning while smoothing the damping characteristics simultaneously (Lu et al., 2009; Giam 2007). Intelligent control based on learning control scheme (Kuc et al., 2003) and fuzzy logic (Senol et al., 2003; Wu et al., 2007) have also being applied for precise positioning.

Precise positioning control has been researched extensively for short travelling distance. However, for long travel, there are challenges in maintaining the accuracy of positioning.

Li and Lee (2001) designed a controller for warehouse crane. One of the axes was tested for positioning accuracy at a speed of 1.57 m/s while moving as far as 30 m and the corresponding accuracy was 1.5 mm. An accuracy of 0.66 mm was also observed for three meters travel distance. Travel distance and the amount of load was a major factor in accuracy achievement.

4.2.6 Wireless Linkage

Cables and wires served as linkages between master controller and embedded controller of the slider. Transducers are often installed to the moving components. The master controller could be a console or a PC for human interfacing and is usually fixed to a permanent location. Connection of the cables are based a communication standard, which could be serial (RS232), CAN-bus, USB or even parallel port for

older systems. In wired communication, the data degrades, as the distance is further apart. Wires have also been reported as a source of failure and the escalating cost of hardwiring has made it less attractive for the future design of industrial equipment (Apneseth et al., 2003; Golnabi, 2003). In recent years, wireless communication for the control of signal transceivers has achieved exceptional reliability due to rapid development in wireless telecommunication. For industry, the cost of installing and maintaining wireless systems is decreasing rapidly (Ciardiello, 2005).

Rapid evolution in wireless communication is largely driven by demand from the consumers for home and office automation (Apnesath et al., 2003). There are a number of wireless standards that have been developed. The IEEE 802.11, IEEE 802.15.1 and IEEE 802.15.4 are the mostly used standards. Usually these standards are referred to the commercial modules associated with them such as the Wi-Fi, Bluetooth and ZigBee respectively. The modules are a subset of a particular standard. These standards are uniform worldwide, but targeted for specific applications, but for some applications, the distinction is not clear cut. Several researches that apply wireless control have been reported. They have been tested in robotics applications for pick and place, camera control and port container management.

Researches that integrated wireless communication for control of large mechanism have been reported in Derby and Brown (2003), Tlale et al. (2003), Ozdemir and Karacor (2006), and Kim et al. (2003). The primary issue regarding this application is also on the state of the signal, wherein the performance of the signal degrades when the distance between the object and the controller is further apart.

Derby and Brown (2003) designed a robotic system called TRACKBOT. The robot was designed to pick and place objects along a conveyor. There were a number of robot heads (Bots) along the tracks. Each Bots was equipped with an Infrared (IR) communication device for wireless communication. A host computer and a remote computer were used to control the motion of each bot. Through wireless communication, the remote computer determined several tasks, such as whether the Bot had entered the station, confirmed the incoming Bot ID, determined the space between successive bots and relayed new commands to the Bots. Some limitations were noted on the IR communication. Electromagnetic interference caused by the variable speed drive on the track chain was determined as a cause of interference between the remote computer and the IR signal. The communication period between the IR and the remote computer was also short, thus limited data were transferred.

Tlale et al., (2003) designed a wireless tele-operated platform for positioning the camera that would be used for shooting of films. The IEEE 802.11 wireless standard was applied. The wireless communication link was between the controller and the platform. It was reported that the design could perform satisfactorily for low data rate transfer. In addition, the line of sight was a limiting factor. The rate of data transfer was unreliable when the device was beyond the line of sight.

Kim et al., (2003) applied GPS and IEEE 108.11b wireless LAN to control an overhead gantry for placing of port containers. The work was aimed at improving

shipping port facilities. The positioning accuracy for horizontal movement was 2 cm, while the accuracy for vertical movement was 3 cm.

Integration of wireless communication for control of gantry cranes was also reported in Ozdemir and Karacor (2006). A mobile phones, based on GPRS and WAP protocol and SCADA was used as the interface to control the operation of a gantry crane. This application would let gantry operators to control the gantry at a remote site. Limitation to this technology was on the performance of the signal, such that the further the remote site, the harder the controller to access the gantry crane.

Improvement in wireless communication for control and monitoring could be achieved with a dedicated communication protocol. At the moment, Bluetooth and ZigBee are seen as a viable option. Both are operating at 2.4 GHz radio band. This radio wave specification is intended for the Industry, Scientific and Medical applications (ISM).

Safaric and Malaric (2006) compared the features of ZigBee, Bluetooth, Wi-Fi and GPRS/GSM. Wi-Fi had the greatest operating bandwidth, which was over 11,000 kbps (Table 4.1). ZigBee had the greatest battery life, hence the power consumption was the lowest. Besides that, ZigBee could also accommodate the greatest number of nodes per network. In sensors and control applications, the recommended standard was ZigBee, because these applications required low latency, low power consumption and did not necessarily required high bandwidth. However, selection between Bluetooth and ZigBee was debatable.

Table 4. 1 Comparison of wireless standard capability (Safaric and Malaric, 2006)

	ZigBee	Bluetooth	WiFi	GPRS/GSM
Code	802.15.4	802.15.1	802.11B	-
Bandwidth (kbps)	20-250	720	11,000+	64-128
Battery life (days)	100-1000+	1-7	0.1-5	1-7
Nodes	256-65k+	7	30	1000

Bluetooth module was based on IEEE802.11.1. Originally intended as a serial cable replacement, the module is capable of handling high data rate transfers (Morais et al., 2008). The rate of transfer for Bluetooth is 250 Kbits/sec (Dursch et al., 2004). However, the system consumes energy continuously, even when there are no data transfers.

ZigBee standard is based on the IEEE802.15.4. The IEEE802.15.4 defines the protocols for physical and Medium Access Control (MAC), while the ZigBee protocol defines the network layer that enable the system to function as a device to device communication (peer to peer) or a device to many devices in a mesh or star network topologies (Baronti et al., 2006). Unlike Bluetooth, ZigBee transfers data at slower rate; at 28 Kbits/sec (Dursch et al., 2004). The ZigBee modules are designed to function with low voltage supply and consume less power for extended period because the module would hibernate when not in used. All ZigBee modules can be configured to act as coordinator, router or end devices. As coordinator, the device

initiates and coordinates network formations and data keeping. As router, the device functions as linkages from other devices to the main controller system. As the end device, ZigBee is a part of the transducers system. In a multi-mesh network, ZigBee has the capability to hibernate the inactive nodes in a multi-mesh network for power management (Ciardiello, 2005). An automated system that does not need high transfer rate of data would prefer ZigBee if cost effective and low power consumption are the factor of concerns. ZigBee modules could also be activated using solar panel rather than typical batteries. Operations that apply ZigBee had been tested in vast fields; from farming (Nadimi et al., 2008, López Riquelme et al., 2009, and Morais et al., 2008) to mining.

One of the significant problems highlighted was the loss of data packets as the distance between the master and the slave increases significantly. In mining application, the percentage of packets received was 95% or over for a depth of up to 10 m and decreased significantly for a depth of greater than 20 m, although adding an antenna could improve the quality of the data transmission (Xio-wen et al., 2009).

4.4 Design Consideration

A set of black and white stripes forms the essence of a conventional incremental encoder for displacement sensing. Consider an object initially positioned on a black stripe and then moved several stripes forward. If the size of the stripes is known, then by counting the number of stripes traversed, one can track the displacement that the object has travelled. Likewise, if the time taken to travel from a given initial position

to the last position is also known, it is also possible to estimate the average velocity. The fundamentals that are explored in this section go beyond this to a much finer resolution.

4.4.1 Patterns

In displacement sensing, the stripes are usually referred to as two-phase encoders. The relative phases give a clear indication of the direction of travel and ‘bounce’ errors are virtually eliminated. It is possible to go much further and used a linescan chip as the sensor in place of phototransistors to monitor the motion. There is a single row array of pixels in a linescan chip, which are capable of scanning the edge of the phase differential at higher capacity than a regular phototransistor. This allows displacement to be detected to within the width of a single pixel, or to even less if the average is taken over several edges in a view scope. The linescan array is used to compare the condition of the two-phase differential at different time interval in order to track displacement.

If the image of the stripes is taken from a view scope, it would appear as a repetitive pattern. Figure 4.2 shows the image of the pattern as seen through a view scope at an instance. Using this pattern, motion information can be derived for precise displacement and positioning. The width of a stripe is equal to the distance between two successive edges. The size of a cycle is the distance between two successive edges, taken from the same phase. There are also two types of phase-difference; one is originating from the white stripe. The other is originating from a dark stripe. A monochrome pattern is adequate for providing a clear phase differential. Mapping of

this pattern provides information on displacement of an object if the positions of a given target between two successive images taken at different time intervals are monitored. If the sampling period is fixed, the information on velocity can also be derived. It is not necessary for the pattern to have the same width of stripes. However, it is important that the cycle is consistent. Hence, comparison between two successive images can be made based on equal footing.

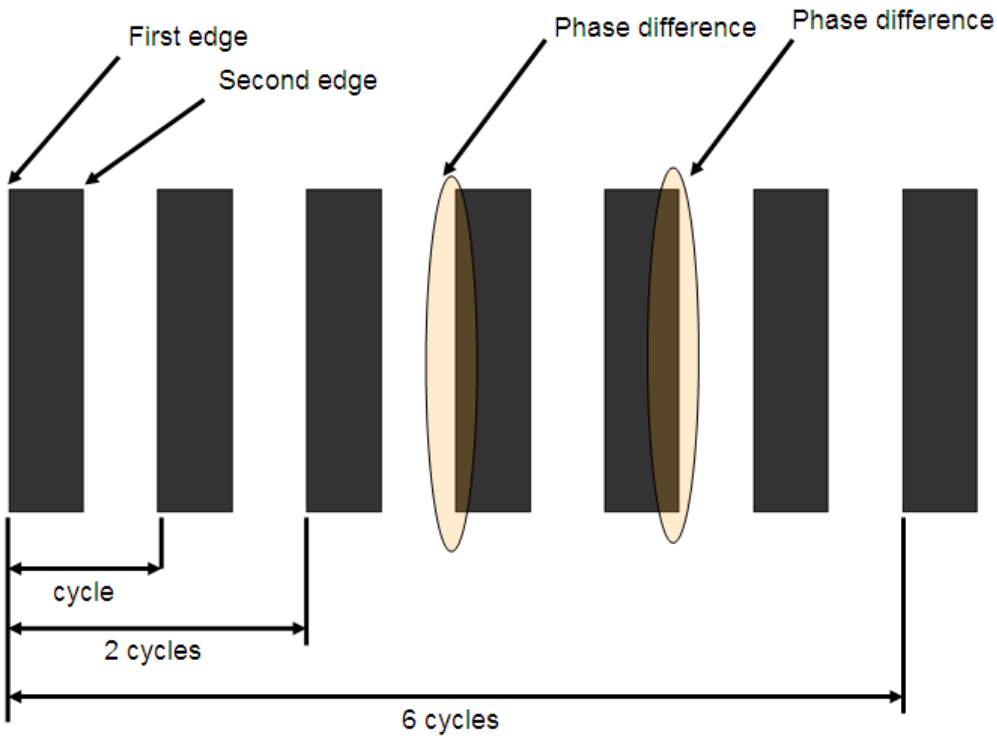

Figure 4. 2 Repetitive patterns and the major information provided the image

4.4.2 Pattern Mapping

Consider the image of a pattern, taken at time t_o as shown in Figure 4.3, there are three stripes appeared in the view scope, but only two appear in complete form.

Because the image occupies the whole span of the array, the edges of the pattern can be mapped and stored in the microntroller in a unit of pixel. Using the left most edge of the view as *reference*, this will be the first pixel. Then, the distance between the *reference* to the first edge is *Edge*. The distance between the *reference* to the second edge is *Edge+1*. Next, the distance between the *reference* to the third and the fourth edges are *Edge+2* and *Edge+3* respectively. In this image, the pattern has provided four edges. There could be more if more patterns are present in the view scope. If time t_o is considered as the first instance when the sensor is activated, then other parameters could be obtained for calibration. Similar to a conventional phase differential, the edges could be marked as *falling* or *rising*. In this case, the edge of transition phase between the white stripes to the dark stripe is assigned as *falling*, while the transition between the dark stripes to the white stripe is assigned as *rising*. Using this convention, the size of a cycle of the pattern can be determined. If a *cycle* is the distance between the edges of the same phase difference, then, the size of a *cycle* is either [*(Edge+2) – (Edge)*] or [*(Edge+3) – (Edge+1)*]. In general form, they are expressed as $cycle(t)$ in a unit of pixel (Eq. 4.6).

$$cycle(t) = \begin{cases} Edge(a+2) - Edge(a) \\ \\ Edge(b+2) - Edge(b) \end{cases} \qquad \text{(Eq. 4.6)}$$

Where:

$a = 0, 2, 4 \ldots$

and

b = 1, 3, 5 …

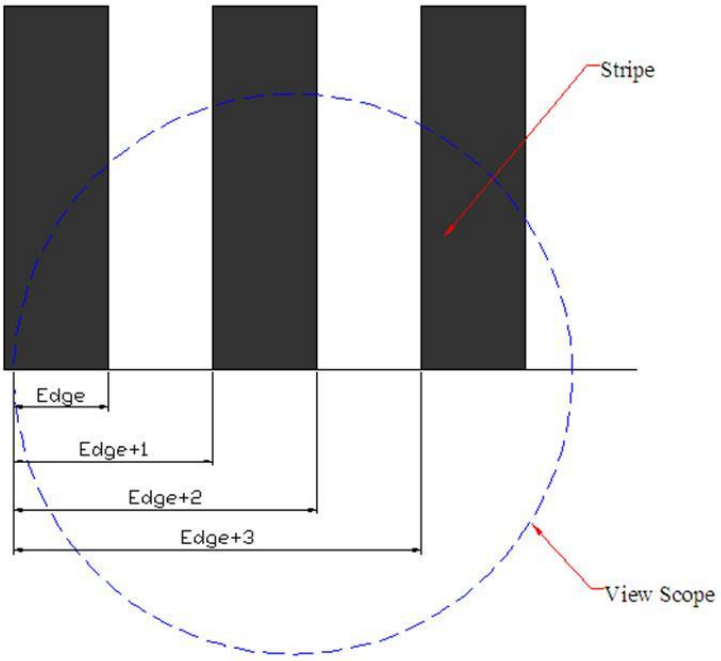

Figure 4. 3 Image of the pattern, taken at time, t_0.

At time t_1, there is a movement detected as shown in Figure 4.4. This movement has shifted the position of the patterns in the image. One of the possible scenarios is the clearance of the first stripe from the view, but a new stripe is trailing. Thus, the first edge as measured from the reference is *Edge*. The subsequent edges are *Edge+1, Edge+2, and Edge+3* for the second, third, and fourth edges respectively. These are the measurements of the patterns at this instant. In this situation, instead of beginning with a *falling* edge when the image sample is taken at t_0, the new patterns begin with a *rising* edge. The presence of alternating condition here is analogous to a conventional two-phase differential. However, the change is due the image being drifted because of the movement and detected by the sensor, rather than interruption of lights to generate

pulses as applied in conventional optical sensor. If the sensor is moving along the slider, the movement is measured directly, whereas backlash from the interaction of the motor and the associate linkages are eliminated from the measurement.

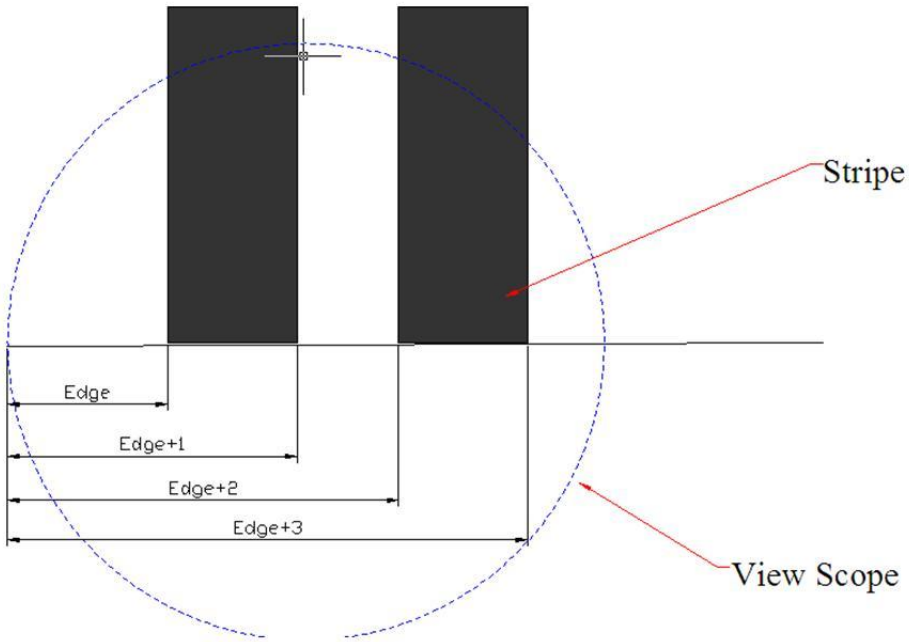

Figure 4. 4 Image of the pattern, taken at time, t_1.

In sampling the edges at any given period, the data of edges is stored in the pixel array. The data is segregated between the edges of *falling* and *rising*. The first *falling* edge is marked as *fall[0]*. The following edges of falling is marked as *fall[1]*, *fall[2]*, *fall[3], ..., fall[n]*. Similarly, the data for rising edges are marked as *rise[0]*, *rise[1]*, *rise[2]*, *rise[3] ..., rise[n]*. In general, they are expressed in matrix form as Eq. 4.7.

$$Edge(t) = \begin{bmatrix} fall \\ rise \end{bmatrix} \begin{bmatrix} 0 & 1 & 2 & ... & n \end{bmatrix} \quad \text{(Eq. 4.7)}$$

As the new image sample at t_1 is compared to the old image sample taken at t_0, the displacement can be determined. Any of the edges could be used, but here the second edge of the *falling* phase is chosen. In any case, the application of the first edge should be avoided, because this edge has a closer proximity to the boundary of the view scope. Since the first edge does not always come from a full stripe, there is an uncertainty to whether the stripe is an actual stripe or a false stripe. Similarly, the trailing edge, which is closer to the opposite end of the view scope, will behave just as the first edge. Instead, the second edge is more stable because the pattern is consistently within the central proximity of the view scope and the stripe would always appear in full form. The same condition is applied to the third edge. Using the second edge for measurement, the difference in the position of the patterns at two successive times represents the displacement, $move(t+1)$. The general form of measuring the displacement is expressed in Eq. 4.8, also in a unit of pixel.

$$move(t+1) = \begin{cases} fall_c(t+1) - fall_c(t) \\ \\ rise_c(t+1) - rise_c(t) \end{cases} \quad \text{(Eq. 4.8)}$$

4.4.3 Resolution

Precision of measurement is limited by the pixel resolution. Using a linescan array, the resolution, *res* is governed by the ratio between the overall width of the patterns in a view scope, *W* to the overall number of pixels available in the array *pix* (Eq. 4.9).

$$res = \frac{W}{pix} \qquad \text{(Eq. 4.9)}$$

If the linescan array has 128 pixels, and the overall width of the pattern in a view scope is 128 mm, the resolution of the pixel is one millimetre. However, if the overall width of the pattern is 12.8 mm, while the number of pixels in an array is 128 units, the resolution is 0.1 mm or 100 microns. Finer resolution is achieved with smaller cycle width. Achieving finer resolution is preferred in order to compensate for error due to accumulative interactions between several sliders. Through optical means, the resolution could be improved if the image is calibrated to minimize the overall width of the pattern in view. If the overall width of the pattern is one millimetre, while there are 128 pixels of coverage in the view scope, the theoretical resolution is 7.8 micron.

Theoretically, sub-micron resolutions can be achieved by manipulating the size of the pattern image observed in a view scope, but in actual implementation, there are limitations. A pattern must at least have one complete cycle, or two stripes in order to compare the status of the pattern between two successive intervals. On the other hand, having only one cycle present, the measurement would be unstable because there is a possibility that the edges are overlapping with the boundary of the view scope. This

would introduce a hesitation in the measurement because the direction of motion is uncertain. Therefore, more than one cycle in the image of the pattern are needed in order to ensure edges are tracked without ambiguity.

Another limitation is set by aliasing factor in sampling. While using direct image comparison simplified the encoding process, *Nyquist Sampling Theorem* stated that aliasing is avoided if the sampling rate, S_r is greater or equal to twice of the highest frequency of the signal. f_s (Eq. 4.10).

$$S_r \geq 2 f_s \qquad \text{(Eq. 4.10)}$$

The anti-aliasing condition as described above is influenced by the speed of the slider, V the sampling rate, S_r and the interval between two successive markings, gp. The minimum gap, gp is a product of V and f_s (Eq. 4.11).

$$gp = V \cdot f_s \qquad \text{(Eq. 4.11)}$$

Consider a sampling rate of one millisecond and the maximum speed of the slider movement is 1000 mm/s. Thus, a gap of two millimetres is appropriate. If the gap of two millimetres is considered as the width of a complete cycle, and in order to maintain that there is at least a complete cycle presence at any sampling period, then the minimum number of cycles that should be present within the view scope at any given time is at least two cycles. Because of drifting, adding 25% to the minimum

number of cycle required would ensure that two complete cycles are always present in the view scope. Assuming that the equivalent length is 5 mm, the theoretical resolution is 39 microns per pixel.

4.4.4 Displacement and Control

Because displacement consists of scalar and vector components, the direction is estimated based on comparison between the magnitudes of movement to the width of a virtual stripe. A virtual stripe is defined as an imaginary stripe, with a constant width. The summation of two virtual stripes is equal to the size of a cycle. Since a cycle comprises of two full stripes, therefore it is convenient to estimate that the size of a virtual stripe is half of a cycle. A virtual stripe is considered because the grating for capturing the image may not have equal size of stripe. Nevertheless, the size of a cycle is certain. Thus, if the image at the new interval is drifting to the right, provided that the move is greater than a virtual stripe, then a cycle of movement has been completed in that direction.

There is an interaction between fine and coarse measurement. If the movement is more than half of a cycle, a coarse movement is registered. For finer detection, the difference between the initial occurrences to the status for the same reference point is determined. In estimating position, both the coarse and fine measurements are included. The variable *cycle* is calibrated to the actual size of a cycle in a pattern, and the fine measurement is also the verniering that is calibrated to the resolution of the transducer (Eq. 4.12). A variable *'phc'* represents the value of the pixels count for half a cycle. '*pixel*' is the initial value while '*pix0*' is the offset reference. In the case

where the movement is from the absolute origin, *pix0* will be zero. However, if the movement is originated from a new datum, *pix0* is the equivalent value of the new datum point in pixels.

$$Position = (Size \times cycle) + \left(\frac{(pixel - pix0) \times 1000}{phc} \right) \qquad \text{(Eq. 4.12)}$$

In applying the transducer for position control, the control strategy will have to be considered. The machining operation influenced the strategy in positioning control. There are at least three positioning scenarios. The first scenario deals with positioning a cutter for calibration and resetting a datum point. In this case, the tool could move from the furthest end to end. The tool does not cut the material, so cutting resistance force does not exist. Moving the tool at the highest possible speed is preferred in order to commence the actual cutting work. In the second scenario, the tool is cutting the work piece, while moving from a given set of target for rough cutting. There is also a need for the highest possible speed, but because there are cutting resistance forces, the magnitude for speed is a compromise. In the third scenario, the cutter is moving at small steps while cutting the polystyrene, for fine cutting operation. Even if the travel distance is short, the highest possible speed is also favoured. In most of the machining operation, speed is a major factor. In this application, a control strategy based on speed-demand control is preferred. The designed linescan camera provided the displacement and positioning sensing.

In controlling the slider, the transducer is installed to the device, while a master controller is fixed in a separate location. For communication, the slider and controller are connected via ZigBee. On the embedded system for slider control, a microcontroller activates the transducer, whereas the linescan and the phase discrimination algorithms are initiated. Tasks in the controller are broken into sections. They are executed in sequence during intervals set by an interrupt. Initial task is to grab data from the linescan, storing only changes in the pixels and records the pixel number at which they are occurred. In the next interval, the type of phases is segregated. The intervals are tested for validation. Changes in the edge status is measured and compared with the previous state. Later, the information of the edges is utilized to estimate the actual position and the corresponding velocity and demanded velocity in real time.

In the control loop, position error, '*error*' is defined as the difference between the target positions to the current position. The target position is the new position as desired in the command. The position error also defined the distance of travel required for the slider to move (Eq. 4.13).

$$error = \text{target} - position \qquad \text{(Eq. 4.13)}$$

Applying a low pass filter to estimate the instantaneous speed, a variable *speed* is also determined, based on the actual difference in the displacement. Thus the algorithm provides a target speed for the movement (Eq. 4.14).

$$speed = speed + \frac{[(move \times micronperpixel) - speed]}{8} \quad \text{(Eq. 4.14)}$$

Velocity demand is determined based on the ratio between position error and the positioning period constant, *posdiv* (Eq. 4.15).

$$veldem = \frac{\text{error}}{posdiv} \quad \text{(Eq. 4.15)}$$

Velocity error is the variable for determining the difference between the demanded velocity and the actually speed. Value for *Velocity Error* decays as the slider is approaching the target position. Using velocity-demand control, the slider attempts to reach the entire distance at the highest speed possible. Eventually, the speed demand approaches zero as the target position became closer (Eq. 4.16).

$$velerror = veldem - speed \quad \text{(Eq. 4.16)}$$

The drive, *u* is made to be proportional to the *Velocity error* divided by a gain constant that acts as damping factor (Eq. 4.17). Since the actual drive of electric motors was limited to the rated design, a limiter was set at the output variable that constraint the maximum drive to within limited range in both directions. A plus sign

represent movement in forward direction, while a minus sign is the movement in reverse (Eq. 4.18).

$$u = \frac{velerror}{gain} \qquad \text{(Eq. 4.17)}$$

$$u = \begin{cases} if\ \ u > 10\ then\ u = 10 \\ if\ \ u < -10\ then\ u = -10 \end{cases} \qquad \text{(Eq. 4.18)}$$

In execution of the design of an anti-aliasing pattern, the sampling rate is limited by the maximum shutter period of a given optical sensor. If the level of illumination is sufficient, the linescan array is able to sense the edges of the stripes. There is a conflict in the level of illumination. Inadequate illumination causes the sensor to malfunction. On the other hand, excessive illumination saturates the image of the grating and prevents any stripes to appear. The dispute is between the frequency at which readings can be taken and the level of illumination required. For very short apertures, a millisecond or less, substantial lighting is needed. This could be visible or infrared.

4.5 Design of a Transducer

An optical displacement transducer was designed and fabricated. The following subsection explains the development of the design.

4.5.1 Mechanical and Optics

The transducer was designed to resemble a camera with a linescan chip as the sensing element (Fig. 4.5). The linescan chip was completely enclosed in a housing that prevented leakage of external illumination. A compound lens was installed to the frontal aperture of the camera in order to focus the image of the object being measured onto the linescan array. The image perceived by the transducer was two dimensional, having both the length and the height. Since the interest was mainly on the length of the image as it was in the same direction as the motion, the height of the stripe was ignored. The appropriate distance between the frontal aperture and the grating scale was determined based on the optical relation equation (Eq. 5.9). Here, the frontal aperture distance, D_w was defined as the ratio of the product between the focal length, L_{focal} and the total sum of the length of the object, L_{object} and the length of the image, L_{array} to the total length of the image. The length of the image was designed to be the same as the length of the array. Therefore, if the length of the array was 8.128 mm, the length of the image must also equal to this value.

$$\mathrm{D_w} = \frac{L_{focal} \cdot (l_{object} + l_{array})}{l_{array}} \qquad \text{(Eq. 4.9)}$$

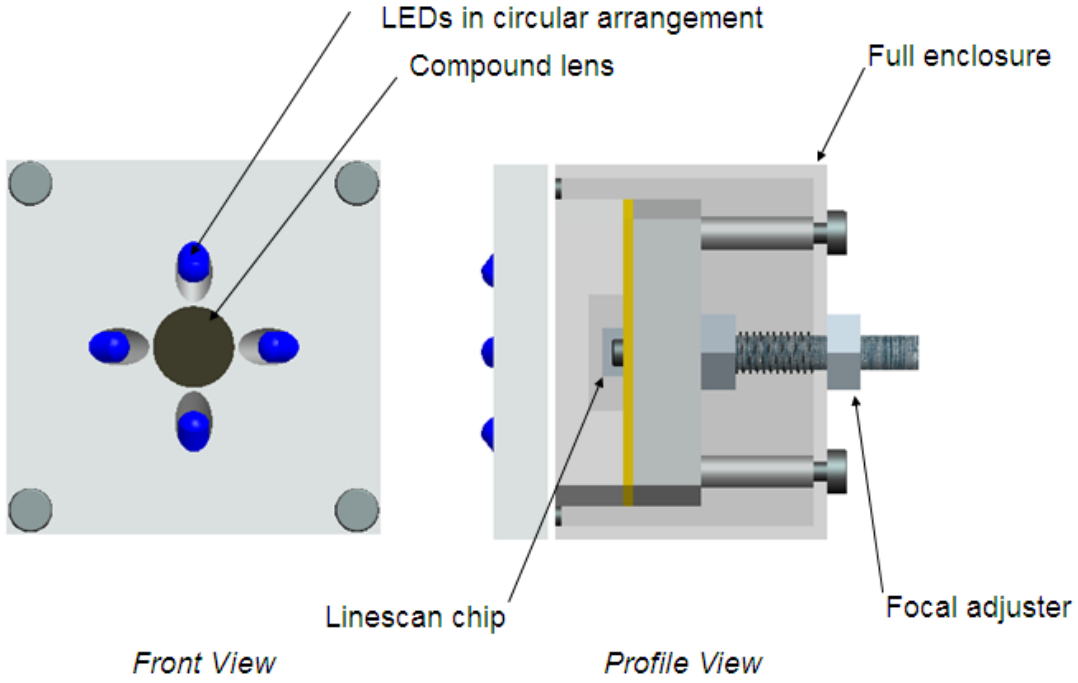

Figure 4. 5 Conceptual design of the direct image encoding transducer; the Front View shows the LEDs arrangement, while the Profile View shows the inner configuration on of the camera.

On the image, the sharpest focus was critical so that the cycle measurement was unambiguous. Therefore, the lens must have an adjustment capability. Adjusting the distance between the frontal apertures of the compound lens to the plane of the gratings allowed improvement in the sharpness of the image. Similarly, this could also be achieved if the distance of the array to the frontal aperture was made to vary, while the distance between the gratings and the frontal aperture was fixed. Advantages of having a back focal adjustment instead of the front are; the overall with of the object remains constant and the adjustment component is easy to access.

On the intensity of the image, the controlling parameters were the illumination level and the exposure period. For compactness, reflective illumination provided by an array of LEDs is applied. In the early stage, the LEDs were installed in circular arrangement.

The effect of focal length of the lens was significant such that shorter focal length allowed shorter distance between the frontal aperture and the gratings. A shorter distance was desirable, because a wider gap would expose the view scope to greater obstructions.

4.5.2 Hardware

The linescan chip was TSL1401R-LF (Fig 4.6). On the linescan chip, there were 128 pixels of photodiodes arranged in a single row. Each pixel was 63.5 μm heights by 55.5 μm width. Spacing between the centres of each pixel was also 63.5 μm, while the spacing between the edges of adjacent pixels was 8 μm. Overall, the linescan pixels array had a span of 8.128 mm measured from edge to edge of the pixels array. The photodiodes on the linescan chip were sensitive to all visible light spectrums and near infrared. Specifically, the acceptable operating wavelength was from 400 nm to 1000 nm. There were eight pins out but only six were essential. There was a pin each for serial input (SI), clock (CLK), analogue output (AO) and voltage source (VCC), and two pins for ground (GND) connection.

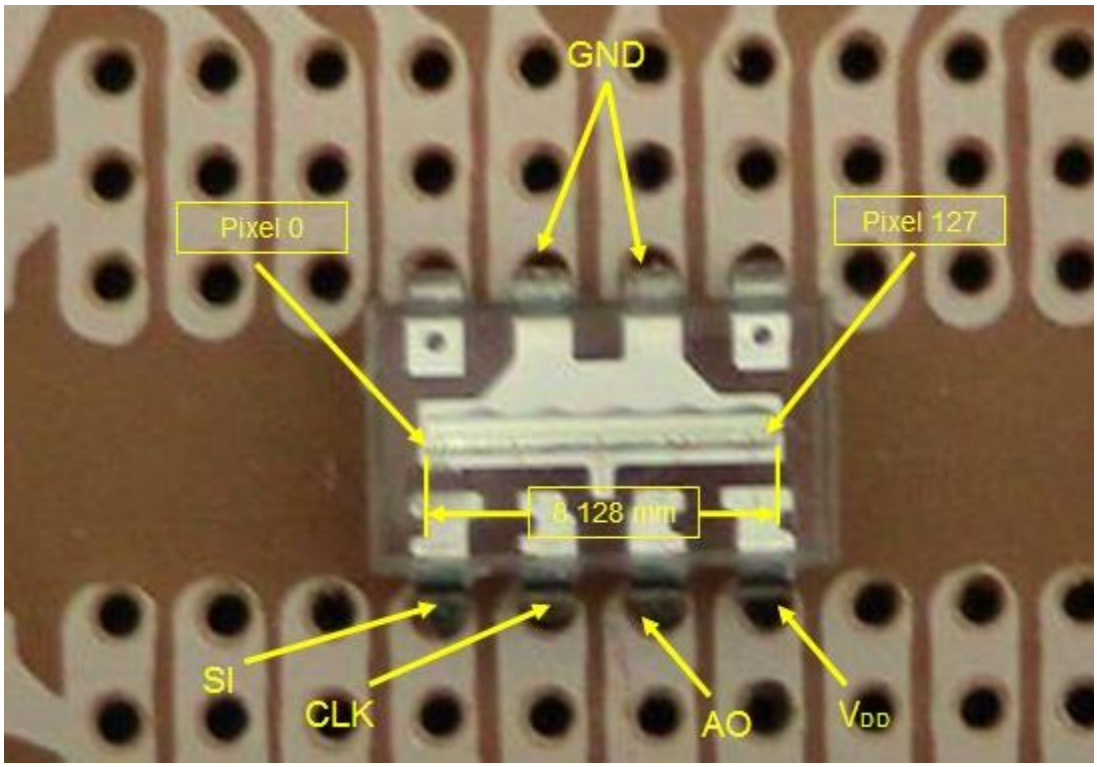

Figure 4. 6 Main features of the TSL1401R-LF linescan chip for sensing the edges of the repetitive patterns.

The chip was controlled and activated by an 8-bit microcontroller through software. An Atmega 8535 microcontroller was initially used, but because there were needs for expansion and additional peripherals, the controller was upgraded to Atmega 128. Both of these microcontrollers belonged to the Atmega family, thus the programming code was compatible with some minor adjustment, especially on the serial communication of the microcontroller initialization. In order to operate, at least five pin-outs from the linescan array were required. Pin four (VCC), of the linescan chip was connected to a five VDC source, while pin six and seven were the grounds. For initiation, a high signal was applied, first to the *Serial Input* (SI) pin, followed by the *Clock* (CLK) pin. A low signal to both pins then prepared the sensor to clock out the

optical data through the *Analogue Output* (AO) pin. The output was the image of the edges of the positioning markers. There was a choice, whether to use the internal comparator of the microcontroller, or an external comparator for processing the AO signal. Depending on the state of the signal received from the AO pin of the linescan chip, an internal comparator was preferred if the intensity of the image was high enough for a comparison in the standard internal comparator at 2.57 V. On the other hand, an external comparator was suitable for low intensity signal, while the threshold could be adjusted to be anywhere within the five volts range. Later, the post-threshold signal was fed back to the microcontroller for displacement tracking and positioning control.

4.5.3 Task Scheduling

A scheduling algorithm was implemented into the microcontroller. The algorithm controlled and managed the tasks to be performed by the microcontroller that included transducer initiation and positioning status. In order to implement, firstly the system clock of the microcontroller was programmed to run at 8 MHz. Using one of the built-in timers, the clock was rescaled to interrupt at 20 microseconds interval continuously. While the interrupt routine was active, the tasks in the algorithm for scheduling executed specific operations of the sensor. Initially, the microcontroller tracked the status of the edges, where the edges were mapped in a unit of pixel. Next, a positioning control routine and a mark-space routine for driving the slider were triggered for positioning control of the slider. Serial data for communication with the master control was prepared and transmitted. Next, a routine for receiving command from the master controller commenced. Upon receiving new commands, the new

information would be processed. The execution depended upon the state of the new command. The final task in the schedule was to refresh the scanning of repetitive patterns from the grating, where the signal was retrieved from the linescan chip. The tasks in the schedule formed a loop that ran continuously, with a sampling rate of one millisecond.

4.5.4 Communication and Protocol

The serial communication standard based on RS-232 was applied. This standard was compatible for both cables and ZigBee, although the ZigBee required additional configuration for operation. Data speed was transferred at 19,200 kbps. This data rate was slightly higher than most serial application that usually applied 9,600 kbps. The ZigBee module had its own physical layer protocol that defined each node connected to a network. The standard protocol insisted that each module was to be set as individual. Initially, the master controller would address the individual node in order to communicate. In this application, the standard ZigBee protocol was bypassed and replaced by a new protocol designed for this positioning application. In order to work, the ZigBee module was reconfigured as general transceiver. Therefore, instead of the need to call on a specific ZigBee module, the calling address was embedded in the controller codes that allow the master controller to function as the originator for all communications.

In a scenario where a number of Zigbee modules were employed to many sliders, all nodes were set to receive commands from the master controller at all times, whereas all commands and data were transmitted to every node. Commands were either

specific or general. In a case that the command was targeted to the traverse axis, the rest of the axis would also receive the data in the received interrupt routine. However, because the command was not address to that axis, the rest of the data was ignored. For the traverse axis, the new command were processed and stored. Depending on the level of urgency, an immediate command would override the existing work. Such command was the emergency halt command, which would be triggered if excessive error or system malfunction was detected. Otherwise, the command was to be executed upon completion of the existing work.

In an 8-bit application, the communication protocol was sectioned into two; with four of the most significant bits were the command bits, and the four least significant bits were the data bits. Command bits written in hexadecimals relayed information of the requested work to be done by the slider. The data bits specified how the work to be executed. There were five layers of command-data in this protocol. The first layer was the addressing. This layer initiated the response from individual controllers. A protocol for addressing had the same code for the command. Zero was used in this coding design for addressing. On the least significant bits, a value 0 to D was assigned to the individual axis. This allowed communication to a maximum limit of 14 axes. The entire code was written as 00 to 0D. On the same level as addressing, 0E and 0F were commands for data stored and applied braking immediately. Since the first line of the routine focused on finding the address, having the stored and braking command on the first layer would quickly bypass the current work and therefore prevented further damage if emergency emerge.

The second layer was dedicated to the control parameters. One of the most important parameters was the positioning variables. In positioning variables, the parameters were sliced into incremental units based on the least significant bits. The smallest units were in a micron. The next subsequent unit preceded at 16 microns increments. Then the next unit incremental was 0.25 mm, followed by 4 mm, 6.5 cm, 1 m and 16 m. The limit to this positioning unit allocation could reach 256 m. In order to prevent overflow, the positioning variable was stored as *long*. Another control parameter was the speed variable. Since the test rig was designed based on *speed* demand control algorithm, there were two levels of speed command. There was the general speed, which was applicable to all operation, and the rush speed, which was intended to drive the motor at maximum speed in case that the slider was needed to arrive to the next point in the least time possible.

The third layer was the procedure of execution. The individual controller would be specified to store the command for later execution, once the current work was either completed or a new target was applied without entering a stop, or halted current operations, pending for the new command to be executed.

The fourth layer consisted of commands for diagnostics. Upon receiving these parameters, the individual microcontroller would return the present status to the master controller. The final layer was the end of command line. This was to indicate that no more new parameters were transmitted and new individual axis was ready to be processed and executed.

4.6 Results and Discussion

The extraction of data for displacement and velocity took place when the post threshold signal that corresponded to the image of the pattern was transmitted to the microcontroller. Activities that involved image capture, edge analysis, displacement and velocity analysis followed a sequence as specified in the scheduling algorithm.

The sequence of the scheduled tasks was as follows: During the first task, *linescan ( )*, the entire array of the linescan chip was read, where the image of the pattern was observed. A variable *count* was incremented in a period that output control bits to the linescan chip to cause it to present the next sample of brightness data. A single comparator bit indicated whether the brightness signal was above or below the threshold. If the value of this bit was different from its previous value, the new value of *coun*t was stored in an array *edge []* for which the pointer *nedge* was then incremented. In addition, the brightness bit (*bit 7of Port C of the microcontroller*) was embedded into the stored value in order to discriminate the origin of the edge source. They were either *rising* or *falling*. When all 128 pixels had been read, the program returned to wait for the next timer interrupt. The maximum value for *count* was directly related to the maximum number of pixels available in the linescan chip. A value of zero to 127 was written to the variable *count* that represented the individual pixels on the array. One of the safeguards during pixels mapping was to include a minimum number of edges. Therefore, a variable *mask* was assigned as a lower limiter to the overall edge counting. This variable was included as a means for data control, such that only a firm number of pixels were considered for counting the

edges, rather than including all transitions. If all edges were considered, false edges might also be included. This would eventually lower the level of precision in the measurement.

In the second timer phase *track()*, the values stored in *edge[]* from the previous task were analysed. The pixels position of *rising* and *falling* were mapped. As a safeguard in the mapping tasks also, at least four edges were needed in order to map the transition and measure the size of the cycles. Because at any time, the edges might start from the *rising* or *falling* phases, both conditions were included in the code. As the transducer required at least two complete *cycles*, the code for pixel mapping was written to capture only three edges of *rising* or *falling*. Included in the pixel mapping routine was a variable *pitch [0]* which was the size of the cycle as measured in pixels. The variable *pitch [0]* was a function of time, whereas the stored value represented the previous value. There were also two variables called *mark [0]* and *mark [1]*, which counted the relative difference in pixels between the recently obtained value of the first *rise* to the first *fall* and the second *rise* to the first *fall*.

With all the necessary algorithm in placed, the functionality of the transducer was tested. For testing, a prototype camera was constructed to scan repetitive patterns printed on papers. In each paper grating, there were patterns with equal and different stripe widths. On the width of stripe, it was not necessary to have them both on equal value, because the repetitive patterns were intended as position marking reference. On the other hand, making the width of either one of them smaller allowed the linescan array to collect more patterns per view.

The image was processed, after receiving of the post-threshold signal from the comparator. In the view scope, the image of the grating occupied the entire length of the linear array. The occurrence on every pixel was recorded as a unit of pixel. Because the entry region may not be reliable enough for measurement and calibration, the first 16 pixels were expunged and the rest was cropped for data extraction.

As the camera moves along the gratings, the phase of the image changed. The first *rise* or *fall* indicated the movement within any cycle. The camera captured several edges. Theoretically, the interval between the first *rise* and the second *rise* should be equal to the first *fall* to the second *fall*, and similarly to the pixel distance between second *rise* and the third *rise* and the successive intervals. The size of a complete interval was equal to a complete *cycle*. There were two sources of displacement data available, since a *cycle* could either be determined from the *falling* or *rising* edges. Considerably more elaboration could therefore be added to the simple software described here, in order to apply error checking and recovery.

The earlier prototype was equipped with a lens that had a focal length of 8.00 mm, while the diameter of the view scope was 14.00 mm. Therefore, the length of the repetitive patterns that were considered was 14.00 mm. Because the total span of the array was 8.128 mm, the image was de-magnified. Figure 4.7 shows the inner configuration of the components.

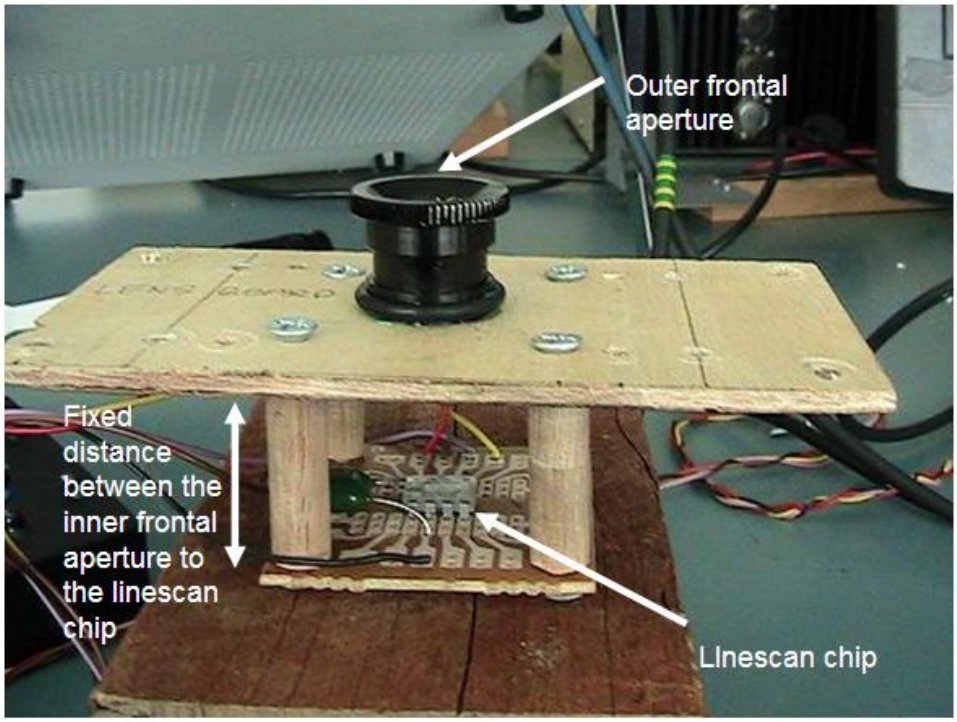

Figure 4. 7 Inner configuration of components for the first prototype.

The distance between the inner apertures of the compound lens to the linescan chip was fixed. In order to focus, the distance of the outer aperture to the repetitive pattern was adjusted manually (Fig. 4.8). The sharpness of the image was determined through oscilloscope, where an in-focus image should appear as a sharp line. Initial test for functionality commenced with a sampling rate of 50 ms.

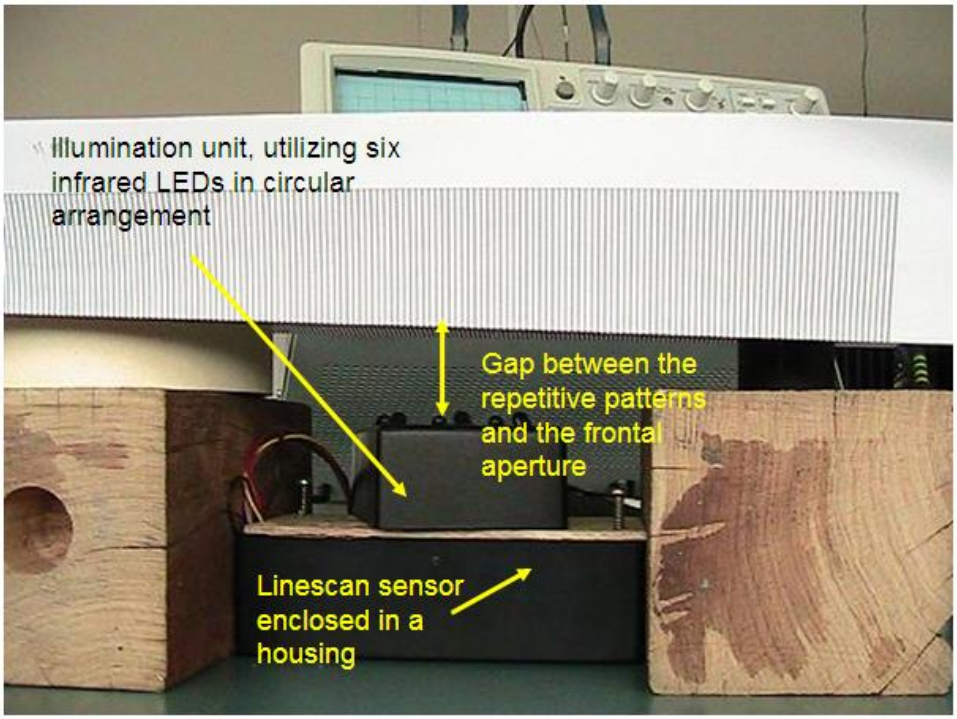

Figure 4. 8 Test arrangements for the first prototype using repetitive patterns printed on a paper.

Fig. 4.9 shows the post threshold image of the repetitive patterns with two millimetre pitch gratings. Because the pattern used for this test had equal width between the white and black stripe, the waveform observed showed an equally spaced top and bottom. From the view scope, the number of stripe was seven. This was equivalent to the total length of stripes of 14 mm. With a compound lens, it was the image of the object that was perceived by the linescan chip, not the actual grating scale. Here, the image was scaled down by a factor of 0.57.

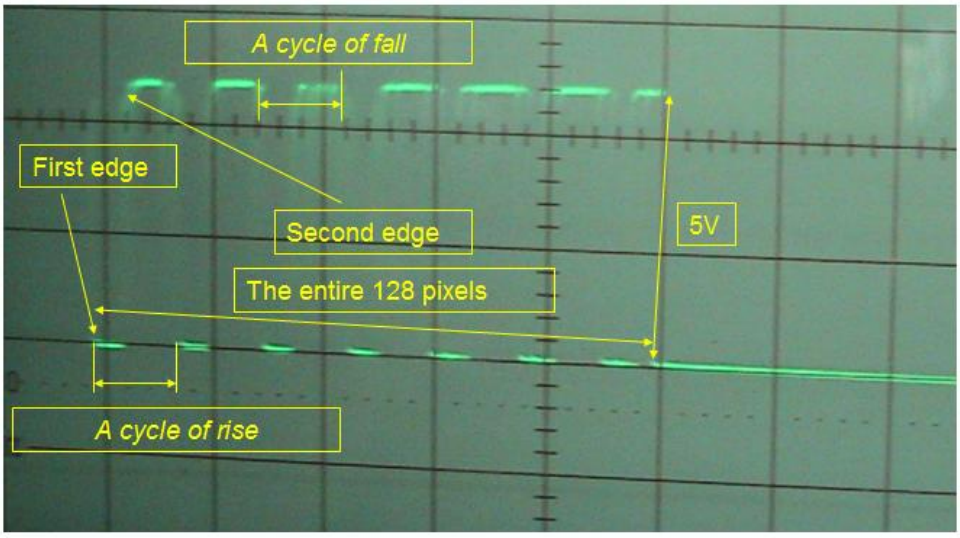

Figure 4. 9 The post threshold signal of the image of the repetitive patterns, taken at 50 ms exposure period.

As discussed in section 4.4, the required image must not necessarily contain a lot of grating cycles. Instead, an object pattern with overall width of five millimetres was optimum. Therefore, a change in the lens type was in order. In reference to the anti-aliasing factor discussed in section 4.4, the robustness in displacement tracking could be improved if there were at least two complete cycles presence within a single reading sample. This could be established through the application of a compound lens with larger focal distance. Two types of lenses, modelled number TN0602B and TN03602B, were applied. Each lens had a 1/3" CCTV viewing format that was equal to a width of 4.8 mm and a height of 3.8 mm. In conventional digital imaging, both the height and width factors of the image were considered for image focusing. However, in this case, the height factor was ignored because the linescan array was needed to scan the image laterally (along the longitudinal direction). The lens was installed in reverse so that the width of the view scope was maintained at 4.8 mm.

Therefore, parameters of the lens were also treated in reverse order. Now, the back focal length became the actual focal length. The width of the view scope was fixed to the width of the lateral size of the CCTC viewing format. The image of the pattern was magnified in order to fill up the entire span of the linescan array. Therefore, the width of the image was 8.128 mm. Based on the focal length for each lens, the image of TN0602B was magnified by a factor of 1.583. The magnification factor for the TN03062B was 1.250. In estimating the optical resolution of the lens, a pixel of the linescan array was equal to 35.1 microns. Because the lens was installed in reverse, and the distance between the front apertures to the object was fixed, the width of the image of the pattern was preserved regardless of the lens type.

Ideally, the image sampling rate should be the highest possible. However, it was found that, the highest achievable sampling rate was one millisecond, as observed through oscilloscope. Using *AVR Studio* software for debugging, the sampling rate was clocked at 1.235 ms. This rate was limited by the minimum exposure time of the linescan chip. Increasing the exposure period would strengthen the signal. While the signal was strong, the sampling rate was slow and inadequate for rapid displacement tracking. Therefore, the illumination level had to be increased. Without adequate illumination at faster sampling rate, the signal would be lost. For a pattern cycle of two millimetres, and the maximum sampling rate was found to settle at 1.235 ms. Using Eq. 4.11, the transducer could track velocity up to 1.62 m/s without losing any pattern. In comparison, at 50 ms for instance, the maximum velocity that the transducer could track was limited to 0.04 m/s.

There was a need for optimization in illumination. Thus, the linescan array was tested against several LEDs with various wavelengths. Removing the compound lens from the pin-hole, an LED was placed on that location and illuminated the linescan array directly. This test indicated the maximum intensity response as perceived by the array. The resulting output signal was observed through the oscilloscope and recorded (Fig. 4.10). The result showed variations of the signal intensity in terms of the voltage output. Among all the types assessed, only the infrared and the high brightness white and green generated an intensity of higher than 4.5 V. The ordinary white LED generated intensity response within 4 to 4.5 V. The rest of the LED types were lower than 2.5 V. The light intensity was reliant to the type of LEDs being used. Using this empirical evidence, it was assumed that both the infrared and the high brightness type could also provide the greatest light intensity if they were installed in the reflective design arrangement.

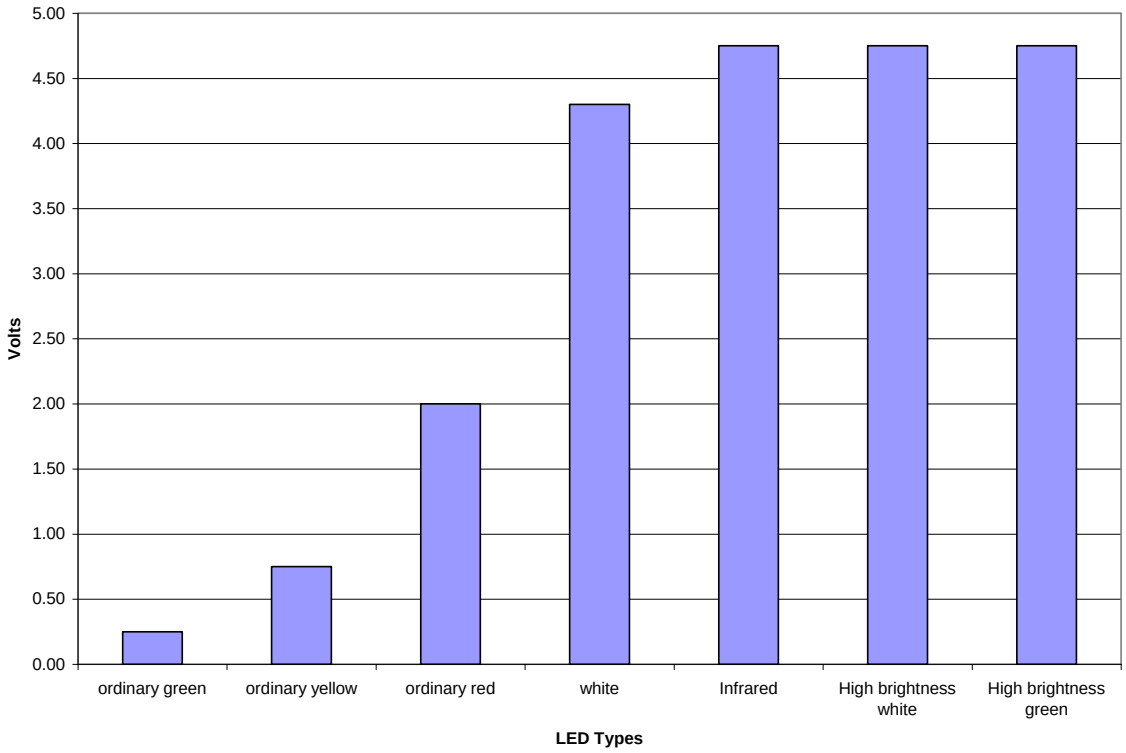

Figure 4. 10 Signal intensity in volts, due to direct illumination on the TSL1401 linescan array.

Although the issue with LED types was resolved, the issue with the LEDs arrangement for optimum illumination remained. In testing for higher sampling rate, a light source that illuminated the linescan array directly could saturate the output signal of the photodiodes. However, when tested in reflective illumination, the maximum voltage was two volts on the analogue output signal. The sampling period at this instance was at one millisecond. Although the analogue signal was low for an internal comparator, using an external comparator with variable threshold setting provided satisfactory digital signal. On the illumination level, an image with uniform intensity was preferred in order to keep the value of cycle consistence. This had led for optimization on the illumination arrangement.

In the first prototype, six infrared LEDs were arranged in circular format. The angle of light convergence was not optimized. Since the sampling rate was slow, the intensity of the output was not affected. In the second prototype, the number of LEDs was reduced to four, such that, the illumination would be concentrated on the centre of the view scope. However, this had produced a significantly unbalanced image due to the convergence of the of illumination energy at the central spot (Fig 4.11).

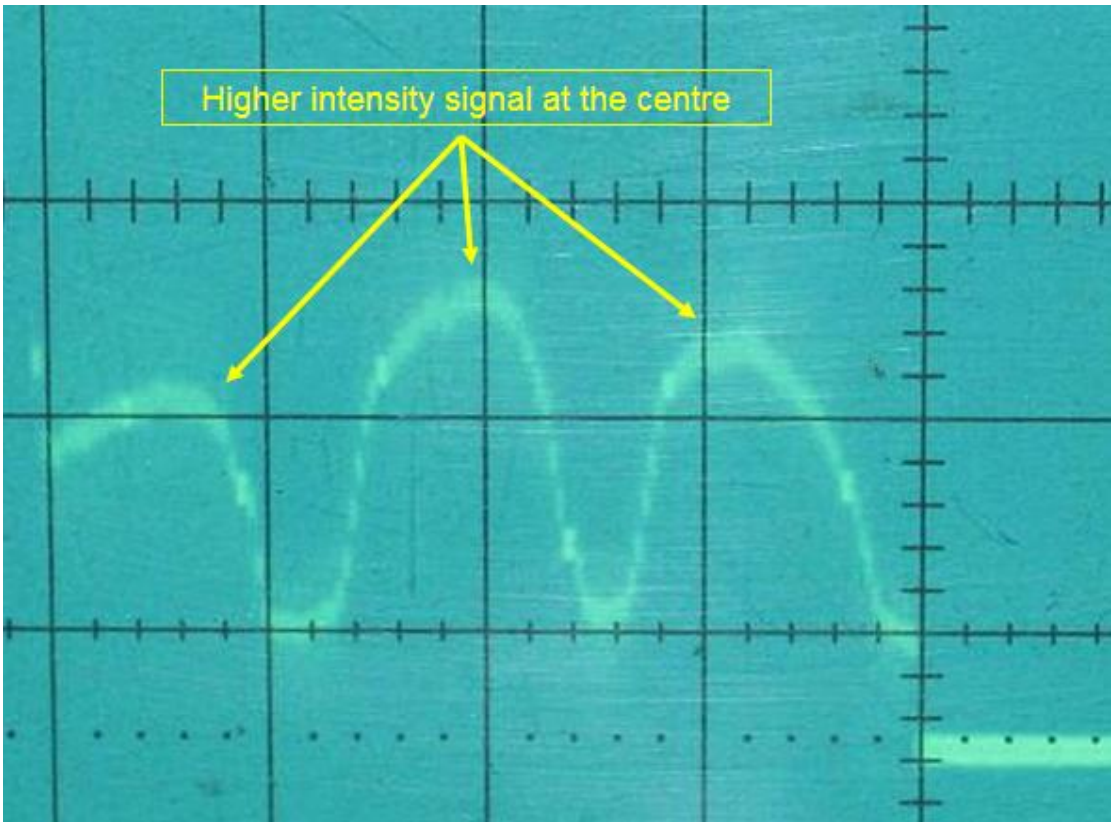

Figure 4. 11 The central spot of the view scope exhibit higher intensity due to convergence of light from the vertical and horizontal axis.

In order to correct, a test enclosure was constructed whereas only two high brightness white LEDs were used to illuminate the view scope along the axis of motion (Fig 4.12).

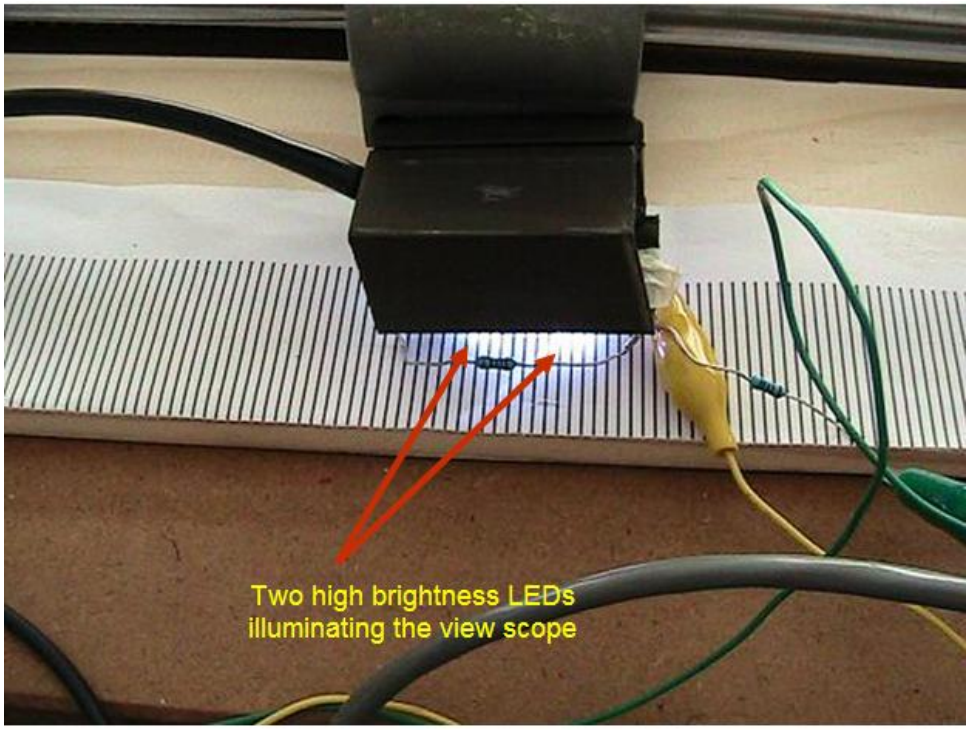

Figure 4. 12 Two high brightness LEDs illuminating the compound lens along the direction of motion.

While the maximum voltage on the analogue signal was similar for both conditions, the distribution pattern between the waveform was uniform throughout the entire view scope (Fig 4.13). Even though the levels between the peaks of the stripe were uniform, the intensity was roughly one volt. For threshold setting, this would require amplification.

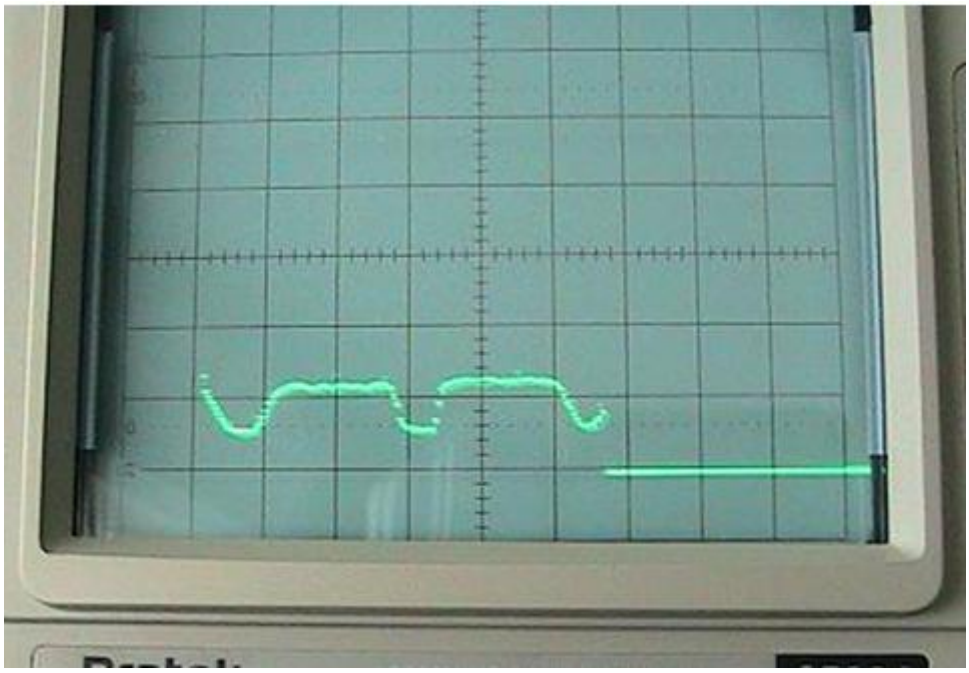

Figure 4. 13 Evenly distributed patterns in analogue form with two LEDs side by side.

Instead, an array of LEDs was constructed that illuminated the grating beyond the boundary of the view scope. This would ensure that illumination level was uniformly distributed across the view scope. Figure 4.14 shows improvement in illumination distribution. The peaks for both stripes were closed to 2.5 volts. The post threshold signal was evenly distributed across the view scope (Figure 4.15).

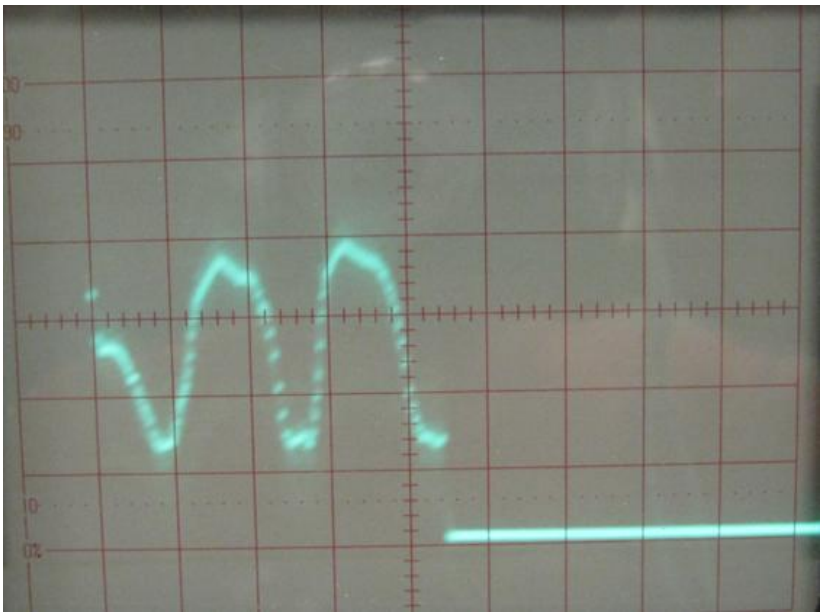

Figure 4. 14 Uniform intensity for both peak using two linear arrays of LEDs illuminating the top and bottom side of the view scope.

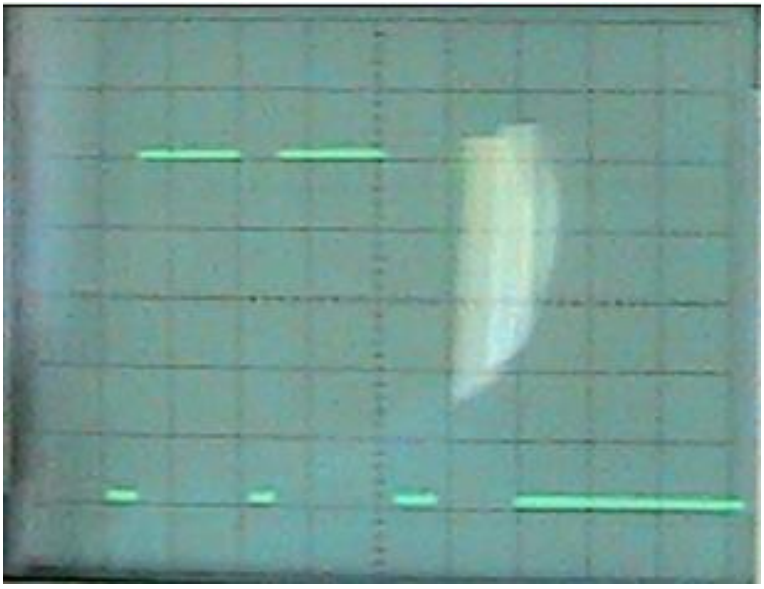

Figure 4. 15 Evenly distributed post threshold signals for the patterns in the view scope.

The camera had undergone several changes (Fig 4.16). The linescan chip was hardwired to a circuit board, while the board was fixed to a bracket. There were four micro-rods to enable the linescan bracket to slide within the allowable alignment tolerance. Maintaining the alignment was critical as it could also affect the precision of the image being read. Therefore, the tolerance of fit between the sliding rods to the placement hole was kept at 50 microns. At the centre back of the linescan bracket, there was a rod and a nut to adjust the focus. The position of the sensor to the back aperture of the lens was pretension to the minimal point. With adjustable focus adjuster, the linescan camera can accommodate different types of lenses with different optical properties, although in order to do so, the lens would have to be replaced manually.

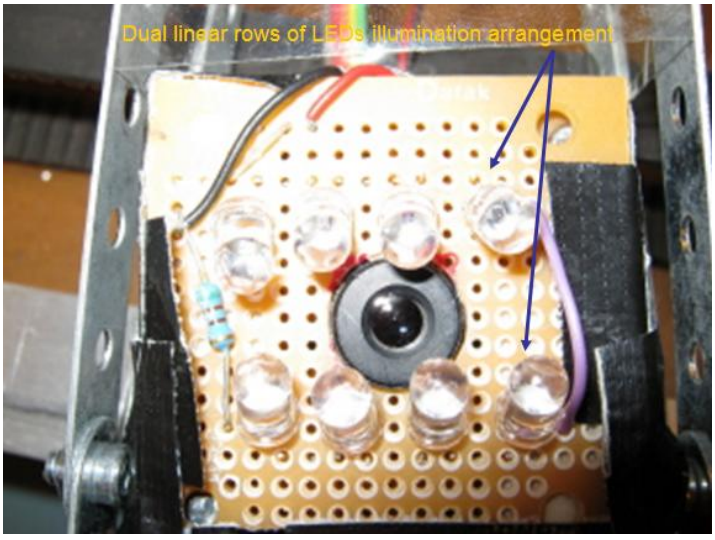

Figure 4. 16 Application of linear array of LEDs to ensure uniformity in the signal across the entire view scope

The transducer was calibrated in the lab using a lab scale test rig. A two millimetre scales of a surveyor tape measure was attached to the flat surface of the rig. The transducer was attached to the slider component of the test rig. Hence, the transducer and the slider were moving together (Figure 4.17). Communication between the microcontroller to the master computer was made through RS-232 cables. Upon initiation of the transducer, the data for a cycle under static and dynamic conditions were recorded for *falling* (Figure 4.18) and *rising* (Figure 4.19) sources. Under static condition, the falling source marked a cycle as equal to 50 pixels, while the rising source marked a cycle as equal to 46 pixels. Under dynamic condition, both sources recorded significantly varying size of a cycle, ranging from nearly zero to 100 pixels. The large difference under dynamic condition was largely due to the rapid instantaneous movement. The size of a virtual stripe (half a cycle) for absolute pattern comparison would be estimated from the static condition because at this moment, the true width of the pattern was observed. On the other hand, the dynamic data was beneficial for velocity tracking. In comparing the cycles, the resolution of the falling source was 40 microns per pixel, and 43 microns per pixel for the *rising* source. If 35.1 micron per pixel was the ideal measurement, the *falling* source was 14% higher, while the *rising* source was 22.5% higher. Using the *falling* source data for reference, the width of a virtual stripe was determined as 25 pixels.

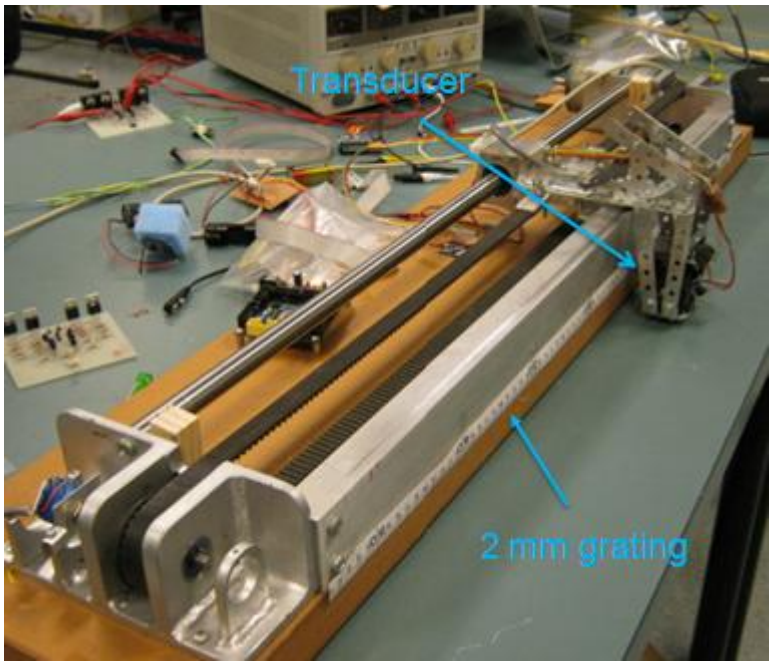

Figure 4. 17 Lab test for optical calibration

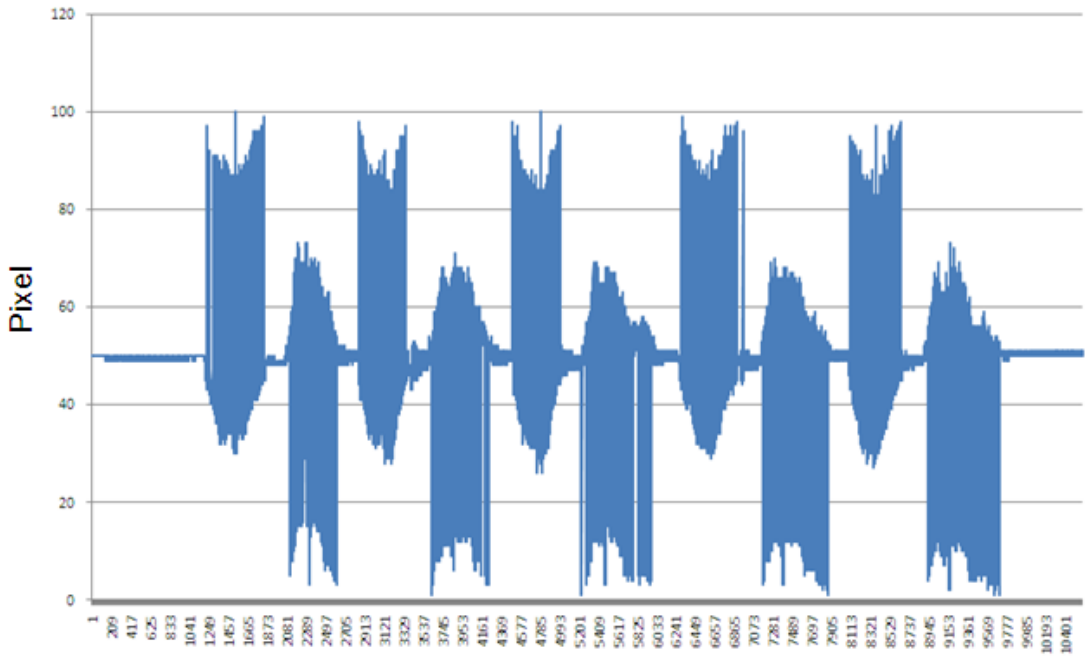

Figure 4. 18 Cycle of *falling* source

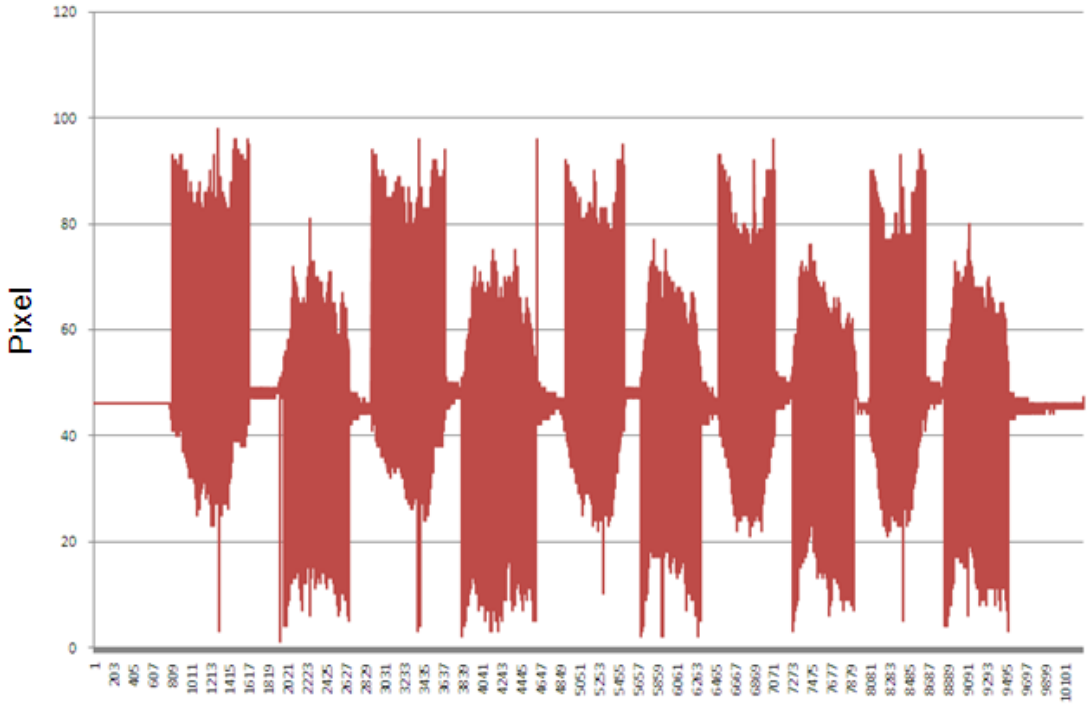

Figure 4. 19 Cycle of *rising* source

In order to apply the transducer on a full-scale track, further changes were made to the linescan camera design. Although the working principle was the same, the housing was enlarged. Thus, attachment brackets were added to the camera for attachment to the slider (Figure 4.20). A metallic frame for placing the LEDs top and bottom array was also fabricated. The slider control unit was separated from the linescan camera housing (Figure 4.21). For full-scale test, communication between the microcontroller and the master controller was established through ZigBee. Within five metres radius the ZigBee transmission rate was consistently at 100%. Therefore, there was no issues of transmission loses. Figure 4.22 and 4.23 show the test rig for traverse axis, which is explained in Chapter 5.

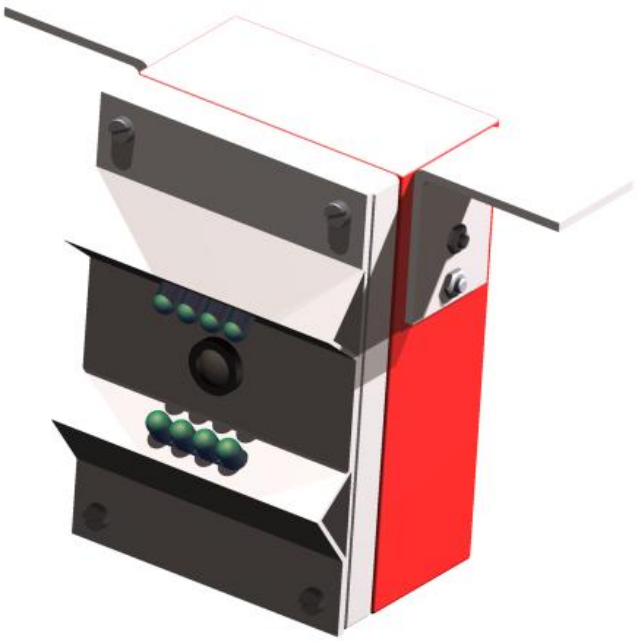

Figure 4. 20 Final version of the linescan transducer

Figure 4. 21 Slider controller unit

Figure 4. 22 Full scale lateral track test set-up

Figure 4. 23 The fabricated lateral slider with direct drive traction unit and the designed transducer that read patterns from a two millimetres surveyor tape

4.7 Summary

This chapter describes the design of a transducer for precise displacement of long travel. The transducer utilized a method that directly interpreted a series of repetitive patterns into displacement markers. *Nyquist Sampling Theorem* was adapted into the design, whereas the use of a two millimetres grating scales was justified. Using direct pattern, the designed camera could track displacement to 40 microns per pixel.

Chapter 5

Design for Leight weight in a Long Travel Gantry

5.1 Introduction

In cutting oversize polystyrene moulds, the machine encounters cutting resistance force at the cutter point. Then, the reaction force is transmitted to the other joints. Therefore, there are requirements to resist deflection and torsion. In applications where there are needs for heavy loads transfer, structural strength, and precise positioning; gantry is the optimum configuration (Rieber and Taylor, 2004; Tan et al., 2004; Jouaneh et al., 1997). In machining oversize moulds, the machine will also have to be sufficiently large in order to encompass the workpiece. It is also necessary for the cutter to reach the object within the workspace. However, the weight of the frameworks and the peripheral system could lead to a massive mechanical system.

Gantry configuration has been recognized for having the highest stiffness among many dynamic configurations (Kondo and Ting, 1999). The mechanical component as shown in Figure 5.1 consists of sliding joints to enable lateral, longitudinal and vertical movement (Sciavicco and Siciliano, 1996). There are variations in the design. In some cases, the vertical axis is not included. Instead, a straight beam or cable with

loads at the bottom end replaces the vertical axis. Usually, this design configuration is applied for '*pick and place*' applications (Hua and Shine, 2007; Sorenson et al., 2007). Usually a gantry is designed to have three degree of freedoms. Additional degree of freedoms could be added for yaw and pitch. These are usually provided by two rotational joints that are attached to the lower end of the vertical axis. Overall, this provides a total of five degree of freedom to the gantry. Usually the vertical axis carries the less weight, while the longitudinal axis carries the most. The way it is driven and the motor that is used to power the motion affect the performance of the slider.

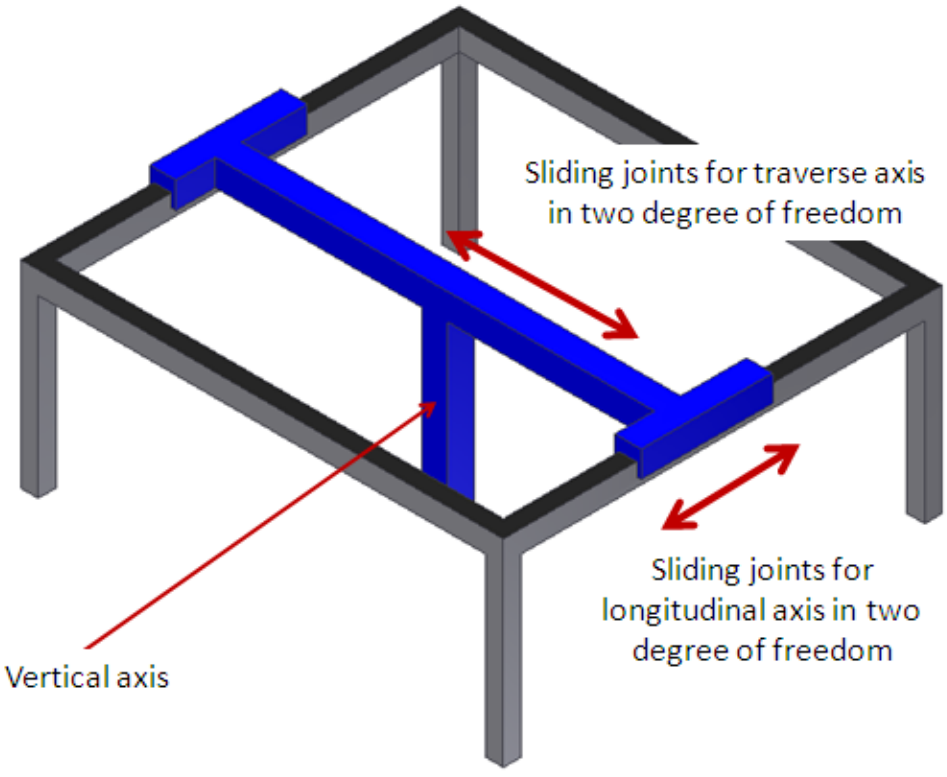

Figure 5. 1Sliding joints in gantry configuration

In the design of a machine for cutting, the primary factor of consideration is on the ability of the mechanical framework to resist deflection and torsion due to cutting. Literatures report two approaches in dealing with this problem. One of the approaches is based on rigid structures. The other is based on flexible structures.

In the flexible approach, the structural members are designed to be flexible. Rieber and Taylor (2004) proposed this approach in gantry design. Precise tool placement relied exclusively on the control system. The weight of the structural members could be lighter that caused low rigidity. The beam condition was modelled and incorporated into a gain scheduling control strategy. It was shown that the design could achieve closed loop control stability while compensating the variation of the beam dynamics.

Although allowing the structure to flex could lead to application of materials lighter than that of structural steels, heavily reliant on the control system for tool placement could expose the machine to positioning error. This will be encountered when power supply is cut off. Restoring the setting of the previous state would be complex.

In the rigid approach, the mechanism is designed to be stiff with zero deflection in all directions. This concept stresses on the needs to have a strictly rigid structural member, while the control system supplements the needs for precise control of the moving object. When considering the overall precision of the system, the degrees of straightness and parallelism have to be included along with stiffness (James et al., 2006). A major advantage of this approach, the mechanical system is reliable even

without the presence of the controller. For example, the parallel longitudinal axes on both sides will not bind, even when they are given an external push to move. A downside of this approach, the overall mechanism is massive. Therefore, high-powered motors are needed to drive the sliders. This adds more weight to the already massive mechanism. However, the control strategy could be less demanding because the platform is rigid enough to withstand deflection and vibration.

While the integrity of a structure is influenced by the material being used (Thompson and Sung, 1983), problems with massive robotic frames could be reduced if light weight materials were used (Brogadh, 2007). Carbon fibres for instance could satisfy the needs for light weight and rigidity, but the material is expensive and difficult to machine.

Most gantry designs use a cable drive system in connecting the power to the drive wheels/rollers in a slider. Placement of the motor is fixed to a position and the mechanical output of the motor is transferred through cable, chain or belt to the drive wheel (Hua and Shine, 2007; Rieber and Taylor, 2004). In this system, the elasticity of the cable has an undesirable effect on the closed loop dynamics, because the link is flexible and easily vibrates (Billinglsey 2006). This design is applicable for short travel movement, but for longer travel distance, such as two metres or more, the self-weight of the cable would cause itself to sag. In order to maintain precision, the linkage requires a tensioning device (Mahadi, 2005). Apparently, sagging due to self weight is also affecting ball-screws application for long travel movement when this component is installed laterally.

Electric motors are preferred as the prime mover for actuating the slider. Each track would have its own motor to drive the slider. In a gantry that requires the slider to run at high speed while carrying load, this would result in the application of a high-powered motor. On the contrary, this would add loads to the structural member because a high-powered motor is also massive.

The type of electric motors does not affect precision of the motion control significantly, except stepper motors that rely on a number of quantised steps in order to rotate precisely (Billingsley 2006). Precision in positioning depends on the design of the instrumentation, if the mechanical components are sufficiently stiff to resist external disturbances from the interaction of the cutter and the workpiece.

Mao et al., (2003) used brushed DC motors to achieve positioning error of within +/- 2 nm in an aerostatic slide system. In this design, brush motors were chosen because friction between the brush and the commutator provided mechanical damping for safety of the operation.

For many industrial applications, friction is a drawback, because the contact will wear out the brush. Depending on applications and load, carbon brush for a DC brush motor could last between 250 to 600 hours of operations (Figarella and Jensen, 2007). Because of *wear and tear*, many applications that use DC brush motors traditionally have been replaced with brushless DC motors.

A number of researches were dedicated to the development of permanent linear magnet motor. Although the linear motor was perceived as an alternative to ball-screw devices, common challenges still exist in the form of trajectory control, synchronization of tandem axes in motion and positioning offset of inter-axis. (Giam, 2007)

Another factor that contributes to massive loading is the cable connection that links the transducers and the drive system. Cables and wires are also a source of failure that requires extensive troubleshooting (Apnesath et al., 2003). In fact, the cost of installing cables and wires are escalating (Samad 2007). In recent years development in wireless communication technology has offered reliable wireless linkage between devices. As cable installation is becoming more expensive and contributes to frequent source of failure, the application of wireless communication, especially for data transfer between sensors and controllers is vital (Brogardh 2007). Integration of wireless communication allows the mechanism to be designed with reduce number of cables.

In short, the weight of the structural members, high powered motors for actuation and hardwire cable connection lead to a massive gantry configuration. This chapter seeks for light weight design alternative and discusses innovation in the drive configuration for weight reduction.

5.2 General Configuration

A full scale test rig was designed and developed for evaluation of the concept. The test rig design was based on overhead configuration. In this arrangement, the workpiece was fixed on the ground, while the cutter would reach the object from above. It had been decided earlier that the ground area was five metres by five metres, while the height was two metres.

An overhead gantry ran on either overhead rail or ground rail. In figure 5.2 and 5.3, simplified models for both configurations are designed in Autodesk Inventor and the finite element analysis is simulated using the built-in FEA analysis system of the software package. The models were used to decide on the structural design of the gantry. The test material was steel (density: 7860 kg/m^3). The beam was assumed to be solid, the cross sectional dimension was 300 mm x 300 mm. The span for the traverse member was five meters. The major difference between these arrangements was on the drive system for longitudinal axis. In the ground rail design, the longitudinal axis was running along a ground track. For overhead design, the track was elevated. On the longitudinal axis for the ground rail, there were two additional members that connect the traverse axis to the ground. Because of the additional members, the overall moving weight for ground rail design was higher than the overhead rail. In this model, the weight for the ground rail was 9,479 kg, while the overhead rail was 7,074 kg. The weight difference was more than 20%. In terms of mass moment of inertia, the overhead rail design required lesser power to actuate the movement, thus promoting less moving weight onto the entire system. Having all the

tracks overhead reduced the prospect of debris from the workpiece to clog the moving components. However, the overhead rail design required adequate rigidity in order to withstand dynamic loading and vibration.

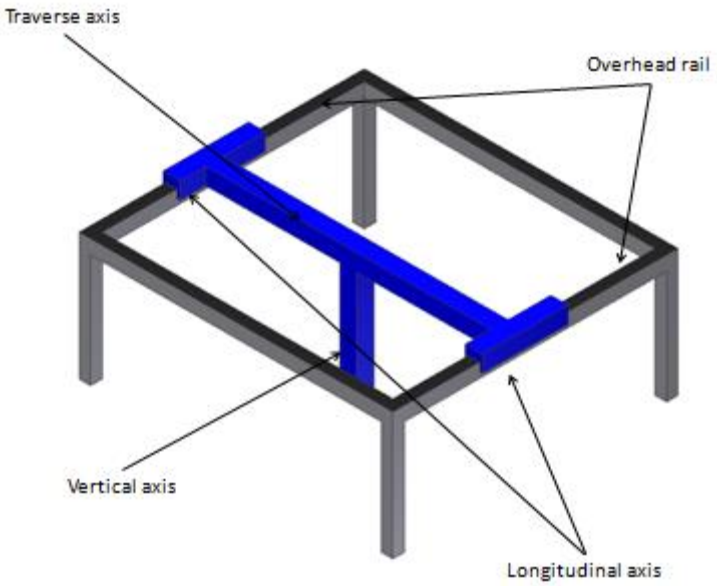

Figure 5. 2 Simplified configuration of an overhead rail gantry

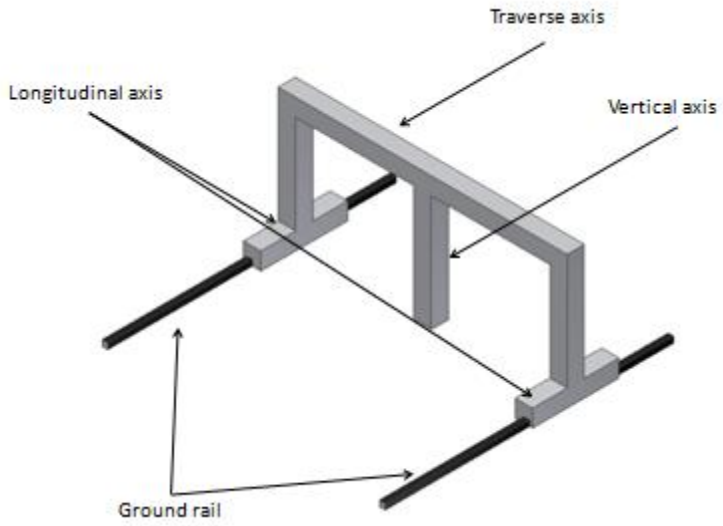

Figure 5. 3 Simplified configuration of a ground rail gantry

Upon decision in overhead rail, further design refinement was based on this configuration. Figure 5.4 and 5.5 show the level of deflection on the gantry when the workpiece is cut along the traverse and longitudinal directions respectively. In the models, all axes were integrated to the entire mechanical frame, thus providing maximum condition at any given load. A cutting force resistance of 100 N was imposed to the lower vertical end of the structure. This was the point of cutter attachment. This force magnitude was an increment by a factor of 10, higher than the measured cutting force on milling with a ball-end cutter reported in chapter 2. The force was purposely exaggerated in order to observe deflection reaction on the structural members. In both situations, greater deflection was observed near the point of contact. Deflection was the greatest if the tool was cutting along the longitudinal direction. However, the entire structural member was experiencing higher deflection when the cutter was cutting along the traverse direction. As shown in figure 5.4, the

traverse beam is buckling and the stress is transferred to the overhead rail structure. This indicated lack of structural support along the longitudinal direction.

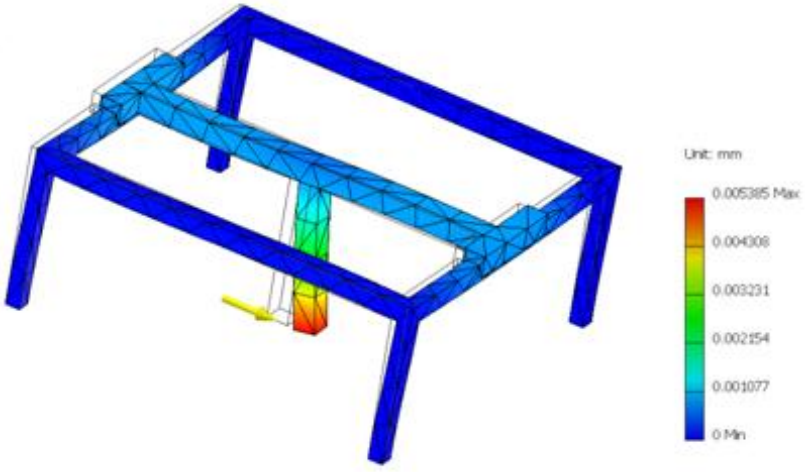

Figure 5. 4 Deflection based on cutting in traverse direction

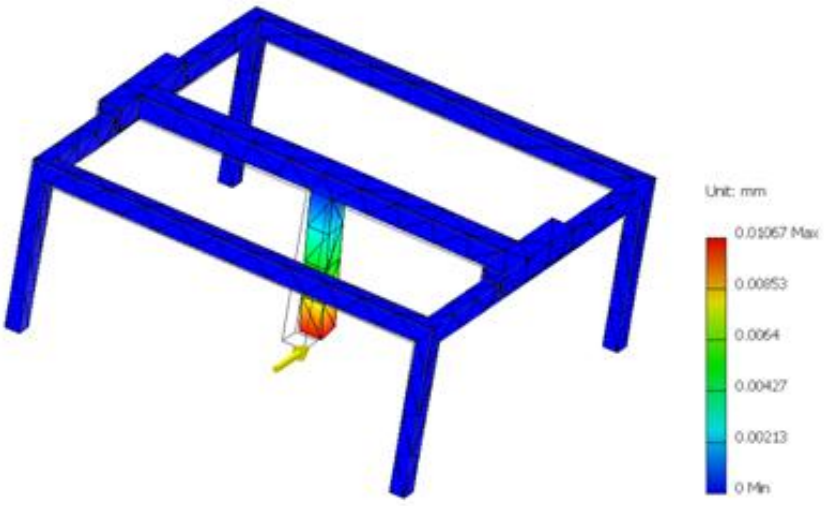

Figure 5. 5 Deflection based on cutting in longitudinal direction

Figure 5.6 and 5.7 show the deflection condition on the overhead rail design after inclusion of additional support columns at the centre of the longitudinal axis. Thus, there were six columns supporting the overhead rail, four for each corner and two for the mid-span section. While the other design parameters were not changed, the additional columns had greatly reduced buckling along the traverse beam. Figure 5.8 shows the conceptual design of the gantry. The major components such as the three principles axes were highlighted.

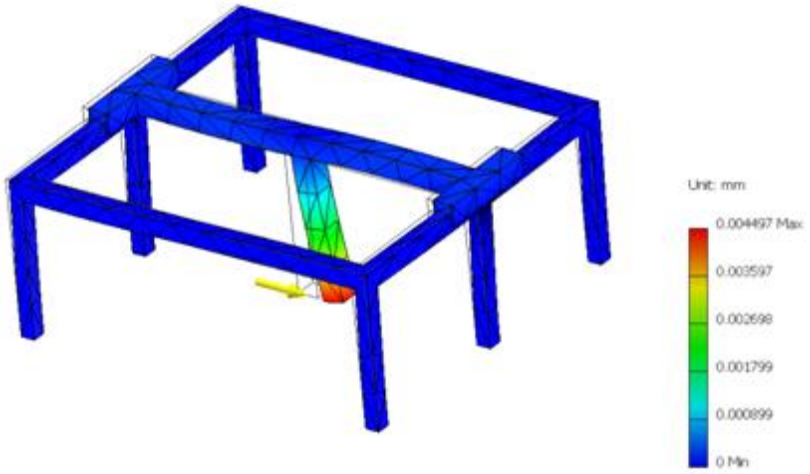

Figure 5. 6 Deflection of cutting along the traverse axis after the inclusion of additional support column in longitudinal axis

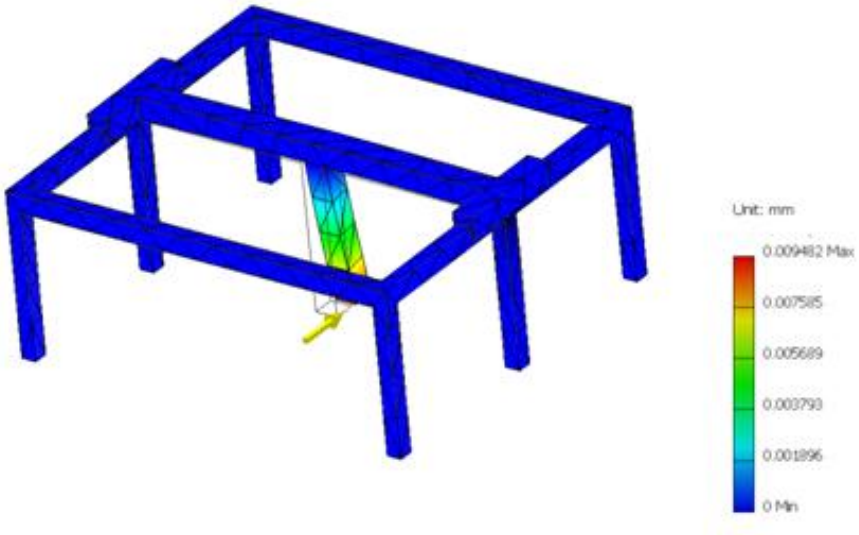

Figure 5. 7 Deflection of cutting along the longitudinal axis after the inclusion of additional support column in longitudinal axis

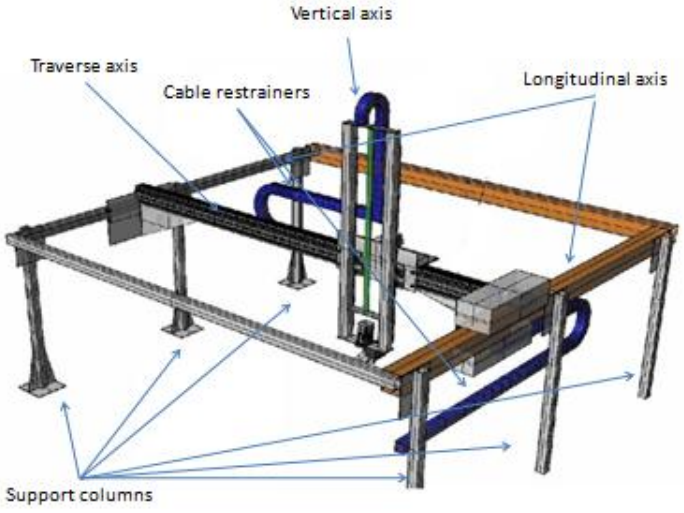

Figure 5. 8 Conceptual design for the cutting gantry

5.3 Design of the Traverse Member

In a multi-axis gantry, the most weight was allocated onto the longitudinal axis, while the vertical axis carried less. However, design for the traverse member was more complex since the axis was suspended and did not have a direct support, while at the same time this axis was also supporting the vertical member. On the mechanical configuration, the design could be an open framework or a beam. In open framework, getting the required level of straightness are problematic. Thus, a beam was considered for simplicity.

5.3.1 Cross Sectional Geometry

In the determination of the optimum geometry for cross section, a number of geometries were considered; they were based on triangular hollow and solid, and square hollow and solid. On the traverse beam, there were two sides of interest. In figure 5.9, the sides are labelled as the vertical plane and the horizontal plane. The vertical plane was the side for vertical axis attachment. Therefore, this plane would absorb the greatest moment due to the cutting force resistance, the weight of the vertical axis and the weight of the slider designed for carrying the tool in traverse direction. The horizontal plane would be used as a track for driving the slider.

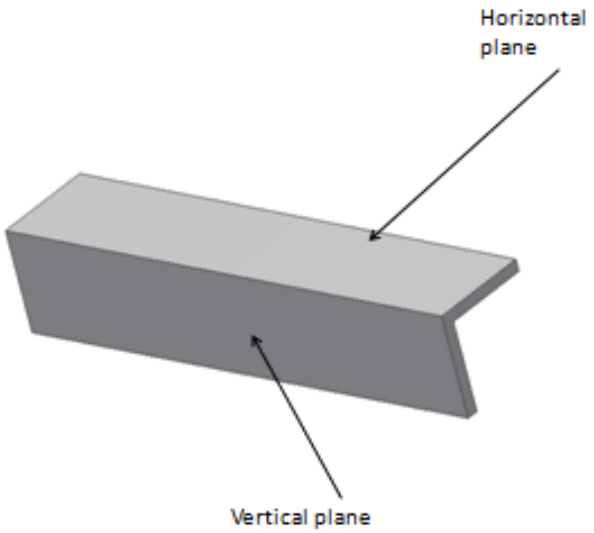

Figure 5. 9 Planes of interest on the traverse beam

Overall, the traverse member was five metres long. The target weight for the vertical axis was 500 N. Because the vertical axis was two metres long at maximum reach, a 1000 N-m moment was imposed to the midspan of the traverse beam. Using a design factor of ten, the cutting resistance force of 100 N was also added, thus the equivalent moment at the midspan was 200 N-m. For cutting along the longitudinal axis, the total moment at the midspan was 1200 N-m. Because both ends were attached to the longitudinal slider, in this case the constraints were fixed for that part.

Preliminary model of the traverse beam was also designed in Autodesk Inventor. The objective was to analyse the characteristics of cross sectional geometry for a given loading condition. Figure 5.10 to 5.13 show the deflection simulation for various cross sectional geometry. For a moment of 1200 N-m due to cutting along the traverse direction, both solid square and triangular beams had the lowest level of deflection. In

terms of weight, triangular beams were nearly half of that of the square beams with the same width and height. However, the square beams had the lowest level of deflection. The deflection of a solid triangular beam was 200% greater than the solid square. For hollow beams, the deflection of a hollow triangular beam was 87% greater than the hollow square beams. In this simulation, all hollow geometries had a level of deflection higher by a power of 10. However, the weight of a solid cross section was significantly high. Hollow beams were sufficient for this application, but the level of wall thickness would be significant when additional moments were included for the effect of torsion on the beam design.

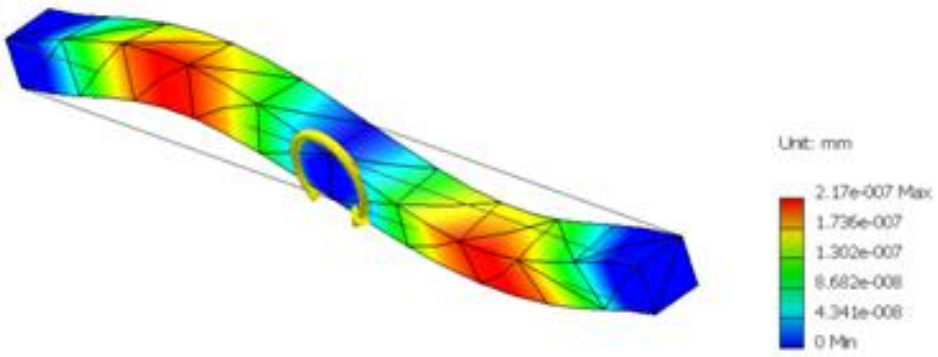

Figure 5. 10 Solid square beam

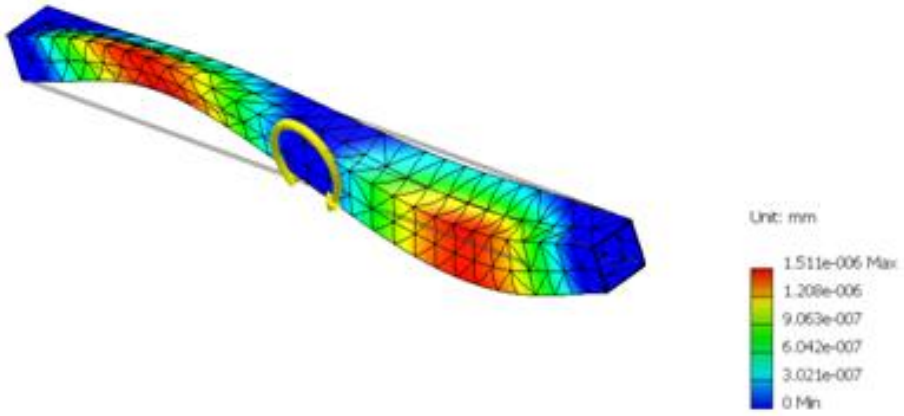

Figure 5. 11 Hollow square beam

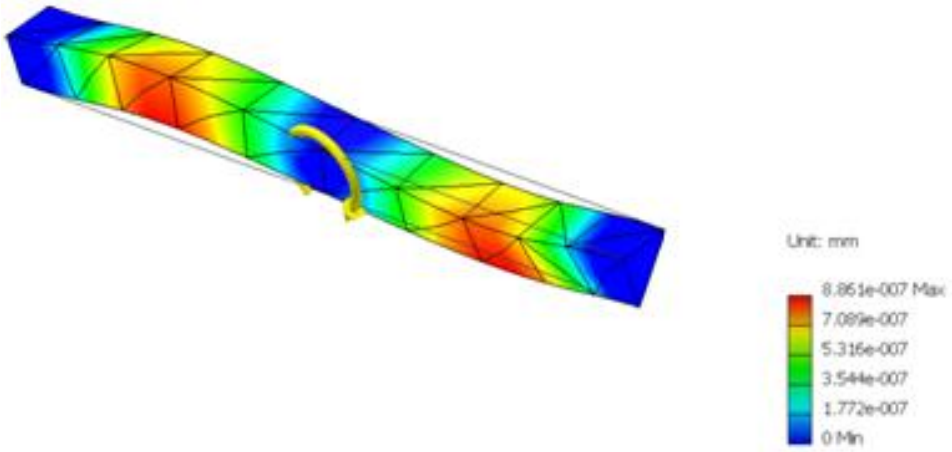

Figure 5. 12 Solid triangular beam

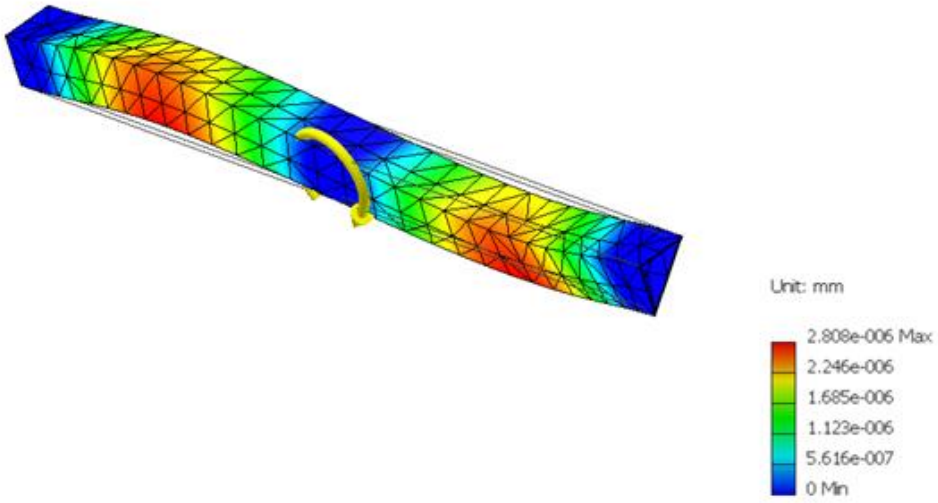

Figure 5. 13 Hollow triangular tubing

Additional comparison was needed, whereas a rectangular hollow beam with a cross section of 150 mm width by 200 mm height was included. Figure 5.14 to 5.16 show the deflection simulation for the given cross sectional geometry with additional moment along the horizontal plane. In this situation, all beams were twisted because the presence of moments in multiple directions. For the given moments, the rectangular cross section had the greatest deflection. However, the triangular hollow beam was having greater torsional deflection. Because of similar wall thickness, all geometries were deflecting at the same power factor. Thus, for maintenance of linearity, the square and rectangular beams were the better options. For the given square beam, the weight is 455.30 kg, while rectangular beam is 259.05 kg. There was a 98% difference which favours the application of the rectangular beam since there was a need for leight weight design and the level of 7.2 microns in deflection was tolerable.

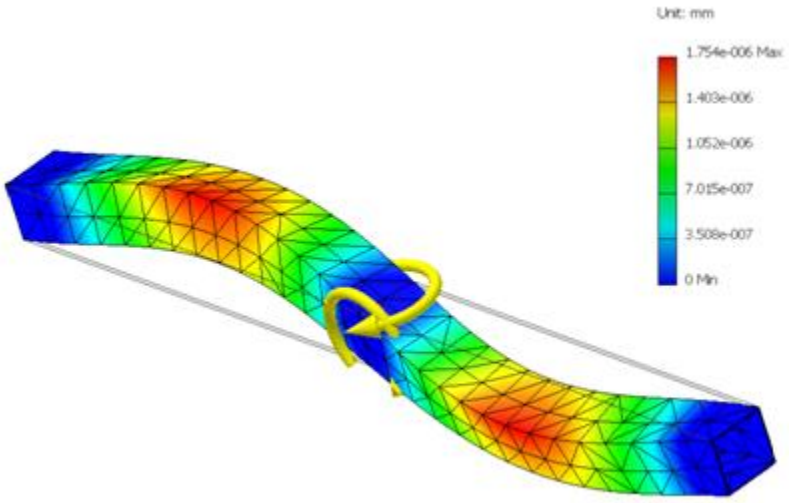

Figure 5. 14 Hollow square beam with moment along horizontal plane at midspan

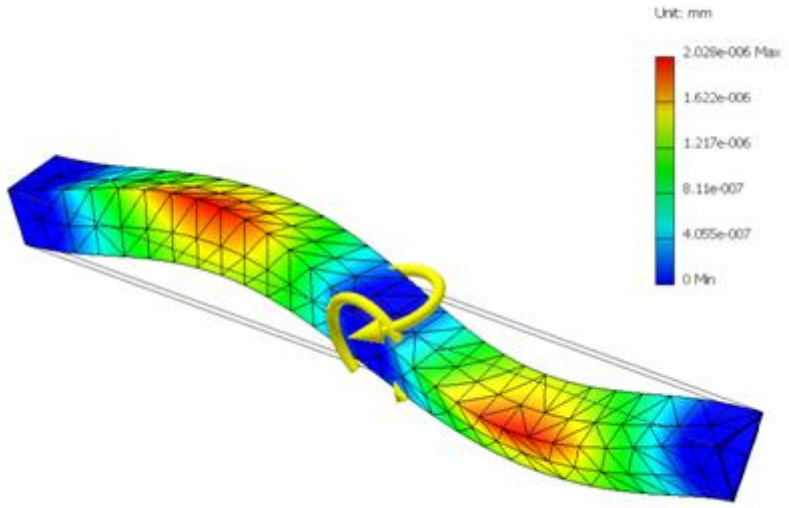

Figure 5. 15 Hollow triangular beam with moment along horizontal plane at midspan

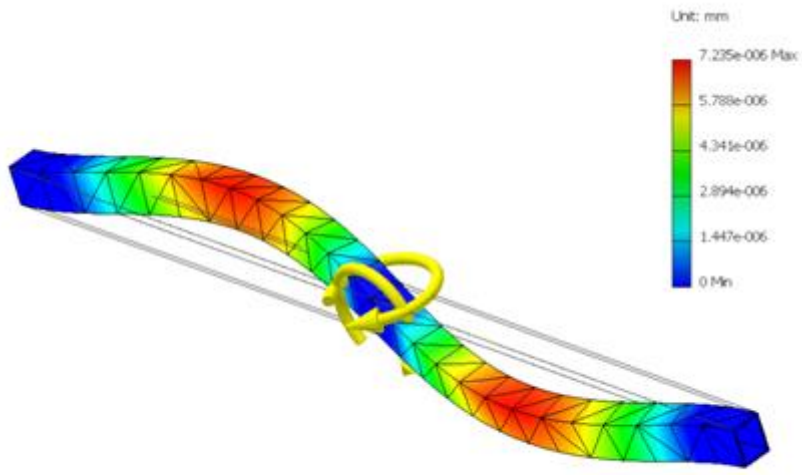

Figure 5. 16 Hollow rectangular beam with moment along horizontal plane at midspan

5.3.2 Innovations in Direct Drive

One of the sources that contributes to additional weight onto the structural mechanism were cables that were used for supplying power to the drive motors and communication between the embedded controller of each slider to the master controller. In using cables, the components were placed inside movable restrainers for management of tidiness. Eliminating the needs for cables would lead to less weight imposed onto the structural members. Thus, lighter and simpler mechanical configurations were attainable.

In the preliminary stage, the slider was designed to take up power from a live conducting track instead of cables that connect the drive system to the power supply. This concept was inspired by the design of high-speed locomotives. The intention was

to purge any source of peripheral weight, originated from cables and the cable management system onto the core structure of the frameworks. Therefore, the role of the track was to guide the movement of the slider and to conduct electrical current along the travel distance. On the overall design, the assembly consisted of two sub-frames. One of the frames was the slider and the other was the track. Both the frame and the slider were made of conducting materials. The track comprised of two sides. One of the sides was connected to a positive source and the other side was the ground. On the slider frame, there was a DC motor for driving, and there were four sets of rollers. Two sets were rolling on the positive side of the track. The other two rollers rolled on the ground side of the track. In order to prevent short circuit, an insulator was placed at the axle of the positive rollers. While the rollers completed the circuit, they were also designed to guide the slider frame onto the track. Because of misalignment could severe the contact, one side of the rollers were sprung.

For proof of concept, a test rig was designed and constructed (Figure 5.17). The track was made of carbon steel and the span was five meters. The rails on the track were divided into two sections – positive and ground. The positive-side was connected to the positive source, and the ground-side was connected to the ground. A 24V DC motor assembly was installed to the slider frame. This motor assembly was equipped with a polyurethane wheel. The motor assembly was obtained as a complete set. The drive wheel was set to run on the positive side of the track. The polarity cables of the motor were connected directly to the body of the frame. Hence, no additional cables were used. On the positive side of the slider frame, two brass rollers were sprung in tension. This was to ensure that the connection of this brass roller to the track was

maintained. On the ground-side of the slider frame, there were two more brass rollers, assembled to the furthest end of the rig. In order to prevent short circuit due to connection between the ground-side and the positive side, the bearing of the ground side rollers were insulated with composite infill (Figure 5.18). Upon activation, the rig and the track assembly formed a closed loop circuit.

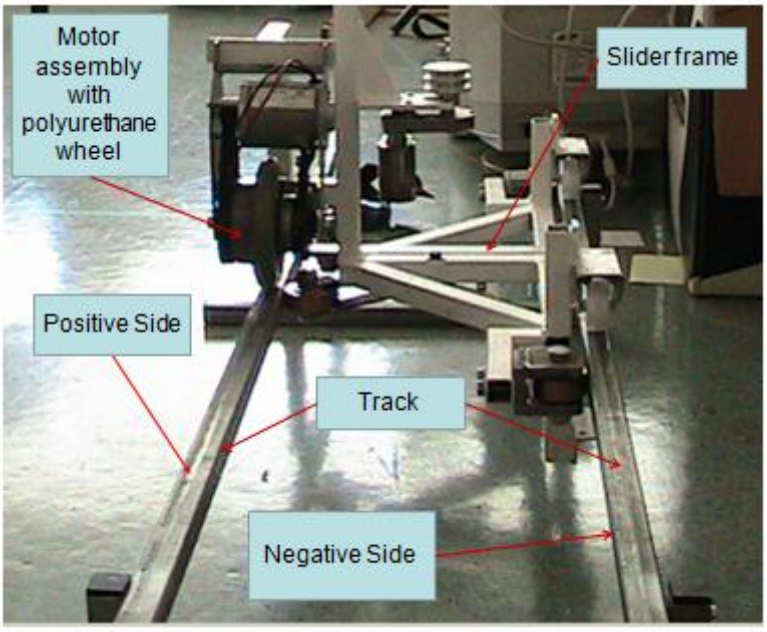

Figure 5. 17 Test rig for direct drive-direct power concept

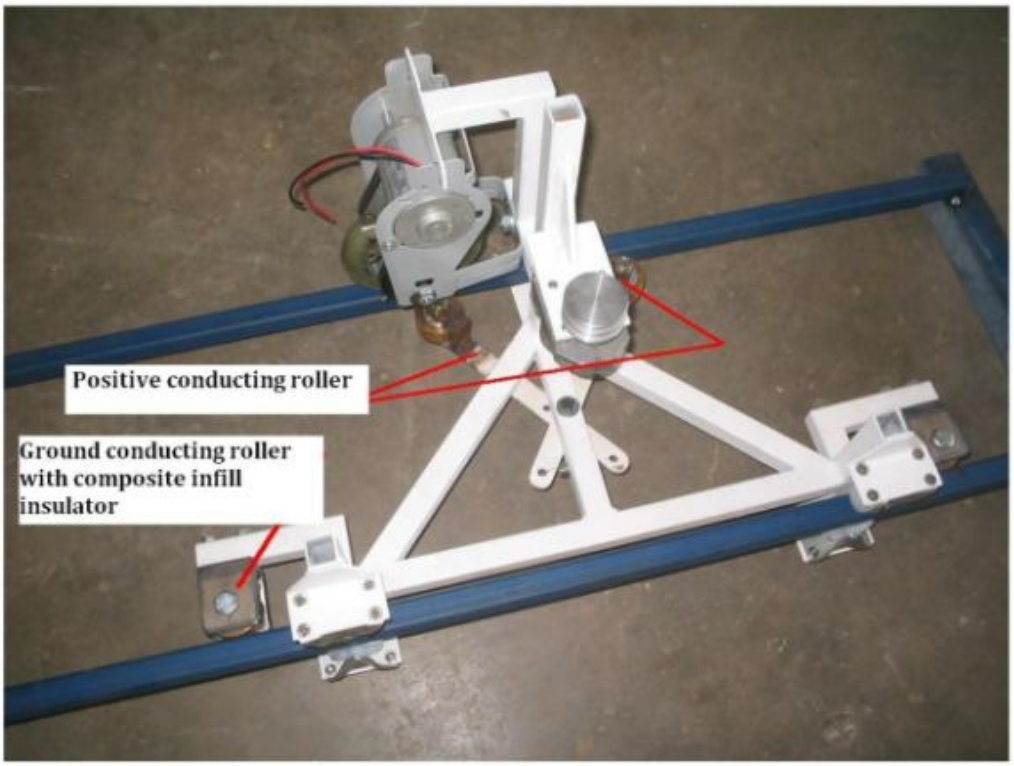

Figure 5. 18 Design of rollers for direct drive – direct power take up

Upon construction of the test rig, there was a short demonstration test run for initial evaluation. The rig was tested to run from end to end. Power was supplied from a laboratory type power supply set. Since the motor was connected directly to the supply, there was only one direction available. A return run was accomplished by manually changing the polarity connection of the motor.

The industrial collaborator was interested in the direct drive-direct power take up concept, but with some reservations. On one hand, this concept could simplify the design of the slider frame. On the other hand, running a live conducting track overhead would introduce safety issues. There was a concerned on fire hazard, since there were sparks if the roller bounced while running on the track. Therefore, a more

conventional approached in power connection was preferred. Cables for power connections were to be applied, but instead of relying on a motor for driving the slider, traction of the drive were distributed to several smaller motors connected in series.

5.3.3 Traction

A direct drive system relied on sufficient traction at the contact point between the roller/wheel and the track. Inadequate traction would cause slip, while excessive traction increased resistance to motion, hence commanding extra load to the drive motor. By definition, traction refers to the force developed at the contact footprint between the drive wheel(s) to the surface of the track. In the design for traction, there was a concern whether to equip the slider assembly with a rigid wheel or a soft wheel.

Extensive research in traction studies were found in off road vehicle design. Models for analysing interaction of soil-wheel had been reported. In soil wheel interaction, pressure from the wheel load deformed the soil; thus the reaction forces at the effective point were slightly offset from the centre of the wheel because of the soft ground conditions (Sharma, 1998; Shmulevich, 1998). Treating the effective contact point as the centre, a footprint was formed as a result of pressure from the wheel. The footprint was the contact area where normal stress and shear stress occurred. These stresses were the reaction of the ground to the load of the wheel. For a wheel on rigid ground, the effective point was assumed to be exactly aligned to the centre of axle in vertical direction (Wong 1989). Figure 5.19 shows the force reaction of a soft wheel on a rigid track. The downward vertical force was F_z. Because the wheel was actively

driven, there were torque, Q and angular velocity, ω. The entry and exit angle was θ. Stresses on the footprint area were the pressure σ and the shear stress τ due to friction between the wheel and the track.

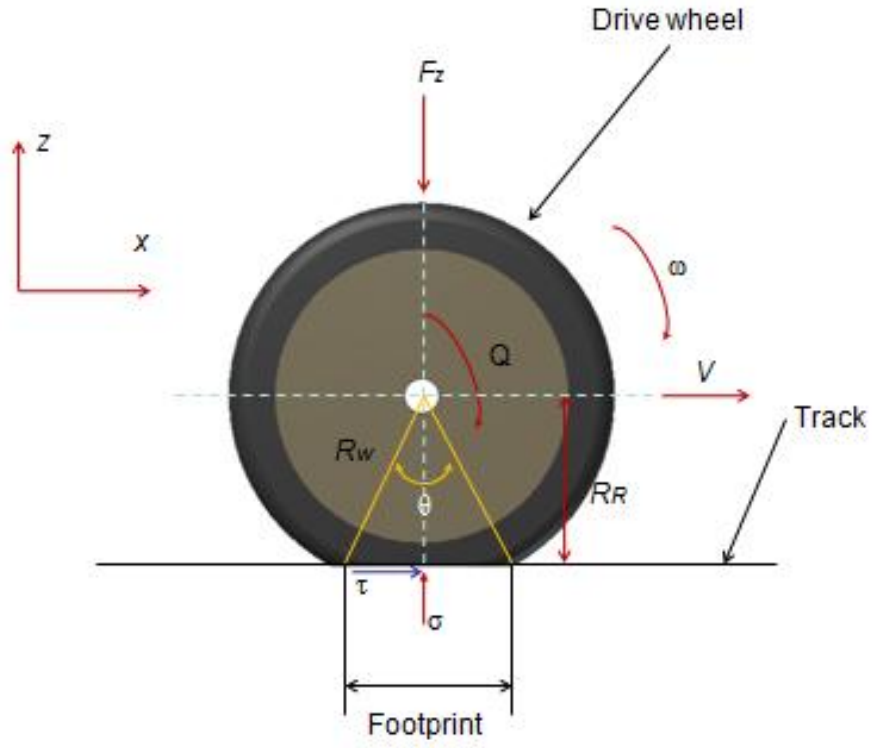

Figure 5. 19 Force reaction of soft wheel on rigid track

The size of the footprint area was significant in the development of traction. If a rigid wheel on a hard surface was considered, the footprint area resembled a line. On soft ground, the footprint area would form an ellipse if a soft wheel was used. The ellipse footprint was larger for softer wheel. However, for soft wheel on a hard surface, the footprint resembled a rectangle. Because of deformation, there were two radii on the soft wheel. First was the wheel radius, R_w and the second was the effective rolling radius, R_R measured from the centre of the wheel to the point of contact (Kiss, 2003).

In rigid wheel, the rolling radius was equal to the wheel radius. In soft wheel, the rolling radius was slightly less than the wheel radius, depending on how large the size of the footprint. Figure 5.20 is an extension to figure 5.19 that illustrates the relationship between the size of the footprint and the rolling radius of the wheels.

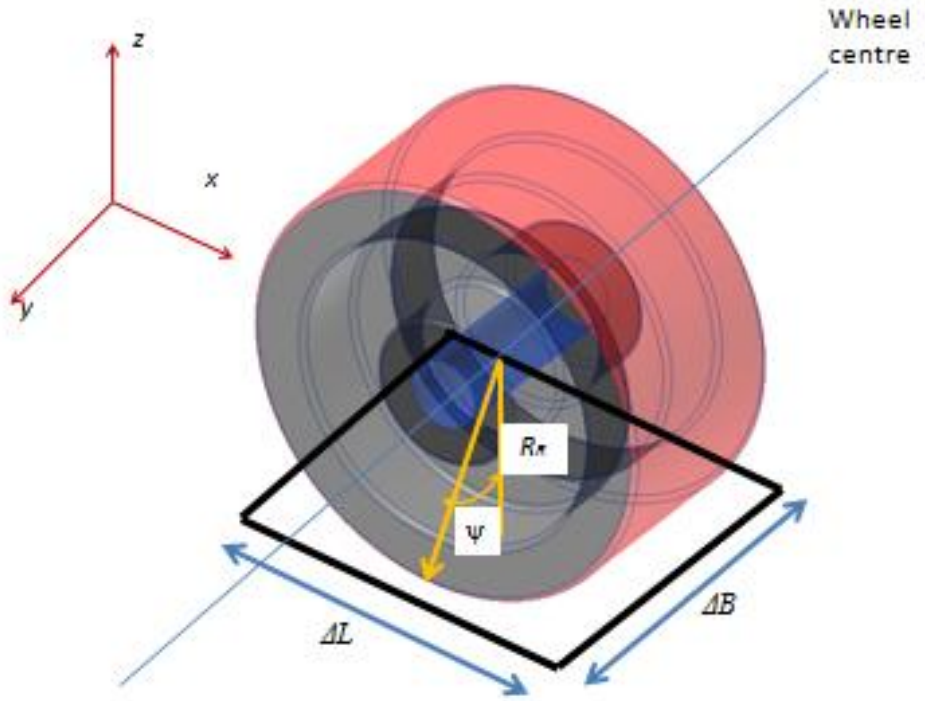

Figure 5. 20 Relationships between footprint and the wheel radii

In order to optimize traction, parameters that govern the footprint area were identified. The footprint area is the product of the effective length, ΔL and the effective width, ΔB of the wheel (Eq. 5.1).

$$A_{foot} = \Delta L \cdot \Delta B \qquad \text{(Eq. 5.1)}$$

The effective length is equal to the wheel radius times the angle θ that span along the entry to the exit point as measured from the centre of wheel (Eq. 5.2).

$$\Delta L = 2\left[R_w \cdot \sin(\frac{\theta}{2}) \right] \quad \text{(Eq. 5.2)}$$

The effective width is a function of rolling radius, R_R times the angle of deflection at the wheel base ψ, measured laterally from the centre of the wheel to the outer edge of the wheel (Eq. 5.3).

$$\Delta B = 2\left[R_R \cdot \tan(\frac{\psi}{2}) \right] \quad \text{(Eq. 5.3)}$$

Because R_R is a function of R_w, R_R can be described as Eq. 5.4 in terms of R_w and the entry to exit angle, θ.

$$R_R = R_w \cdot \cos(\frac{\theta}{2}) \quad \text{(Eq. 5.4)}$$

Therefore, the effective width, ΔB of the soft wheel in Eq. 5.3 can be rewritten as Eq. 5.5.

$$\Delta B = 2\left[R_w \cdot \cos(\frac{\theta}{2}) \cdot \tan(\frac{\psi}{2}) \right] \quad \text{(Eq. 5.5)}$$

Unlike the effective length, ΔL that could be zero, the effective width ΔB had a minimum value, even when the wheel was unloaded. The minimum value for ΔB was equal to the original width of the wheel. Therefore, if the width of the wheel was 75 mm, while the rolling radius and the wheel radius was also 75 mm and the angle θ was also zero, the value for ψ was 26.57^{o}.

Based on figure 5.19, the vertical force, horizontal force and moment (torque) about the centre of wheel are determined in Eq. 5.6 to Eq. 5.8.

$$F_z = \Delta L \cdot \Delta B \cdot \sigma \qquad \text{(Eq. 5.6)}$$

$$F_x = \Delta L \cdot \Delta B \cdot \tau \qquad \text{(Eq. 5.7)}$$

$$Q = R_R \cdot \tau \qquad \text{(Eq. 5.8)}$$

Substituting the wheel radius, R_w into Eq. 4.6 to Eq. 4.8, the forces and moment are described in Eq. 5.9 to Eq. 5.11.

$$F_z = 4 \cdot R_w^2 \cdot \sin(\frac{\theta}{2}) \cdot \cos(\frac{\theta}{2}) \cdot \tan(\frac{\psi}{2}) \cdot \sigma \qquad \text{(Eq. 5.9)}$$

$$F_x = 4 \cdot R_w^2 \cdot \sin(\frac{\theta}{2}) \cdot \cos(\frac{\theta}{2}) \cdot \tan(\frac{\psi}{2}) \cdot \tau \qquad \text{(Eq. 5.10)}$$

$$Q = 4 \cdot R_w^3 \cdot \left[\cos(\frac{\theta}{2}) \right]^2 \cdot \sin(\frac{\theta}{2}) \cdot \tan(\frac{\psi}{2}) \cdot \tau \qquad \text{(Eq. 5.11)}$$

The moment as described in Eq. 5.11 is also the rolling resistance that must be overcame by the torque from the drive motor. A compromise was needed whereas the minimum rolling resistance existed for sufficient traction.

There was also an issue whether to allow the drive wheel to fully support the weight of the slider. Excessive load would burden to the drive wheel if it was designed to support the weight of the slider. Therefore, the weight of the slider was allocated to a set of passive rollers that run on a fixed tracked. In addition, the passive rollers were also designed to guide the movement of the slider, thus ensuring straightness. Thus, the function of the drive wheel would only to provide traction. Since traction also required a vertical load in order to clamp the device onto the surface of the track, a spring load mechanism was designed.

5.3.4 Traverse Slider

The traverse slider was designed to enable translational movement along the traverse axis. In reducing the weight of slider, the direct drive concept as discussed in earlier section was applied. The slider was powered by DC type electric motors. However, power to the motor was relayed through cables. Because the interest was on leight weight, distribution of power to for drive is explored. In this case, instead of using a high powered motor, multiple smaller motors were combined to drive the slider. These motors were inadequate for individual usage, but when combined in series, they

provided sufficient power. For small DC motors, the power cable was relatively small and light and easy to manage. An added advantage to this design was the capability of the slider to maintain operation, even if one of the motor was malfunctioning and although the connection of the motors would have to be reworked, the amount of time to be spent on trouble shooting was less. In this case, the maximum speed would be less than the intended design, but the downtime for an ongoing operation would be less, as the operation could be resumed in a short period.

Initially, the slider was assumed to carry an overall load of 250 kg. If the motor acceleration was assumed to be 0.5 m/s^2 while the speed of movement was 1 m/s, the power required to move the slider was 125 W. At the stage where most parameters were undetermined, a design factor of four was included, thus provided a target power of 500 W.

Two 24 V DC geared motor was procured (SC250G). The motor documentation listed down several parameters. At maximum load, the motor would draw currents up to 13.12 A. Under no load, the maximum current was rated at 1.86 A. The weight of each motor was 2 kg. At maximum speed, the nominal torque was rated at 7.46 N-m. The power of the motor was rated at 250W.

The intention was to run both motors in series, so that the total power of 500W would be achieved. A subassembly that consisted of the motor and a drive wheel was designed and constructed (Figure 5.21). As discussed in section 5.3.3, this subassembly would be the drive unit, purely dedicated to power the movement, but

not exerting the load of the slider. The drive unit was designed as a cassette type, for ease of replacement. For each drive unit, there were two points of attachment. The fixed point attached the drive unit to the slider frame firmly. The fixed attachment plate was hinged to allow adjustment in clamping angle for traction. The other attachment point clamped the drive unit to the body of the slider (Figure 5.22). There were openings that allowed the drive wheel to protrude out from the slider frame, connecting the drive wheel to the track and established traction through adjustment of the height of the spring load system. Larger footprint would be established if the spring load was clamping harder.

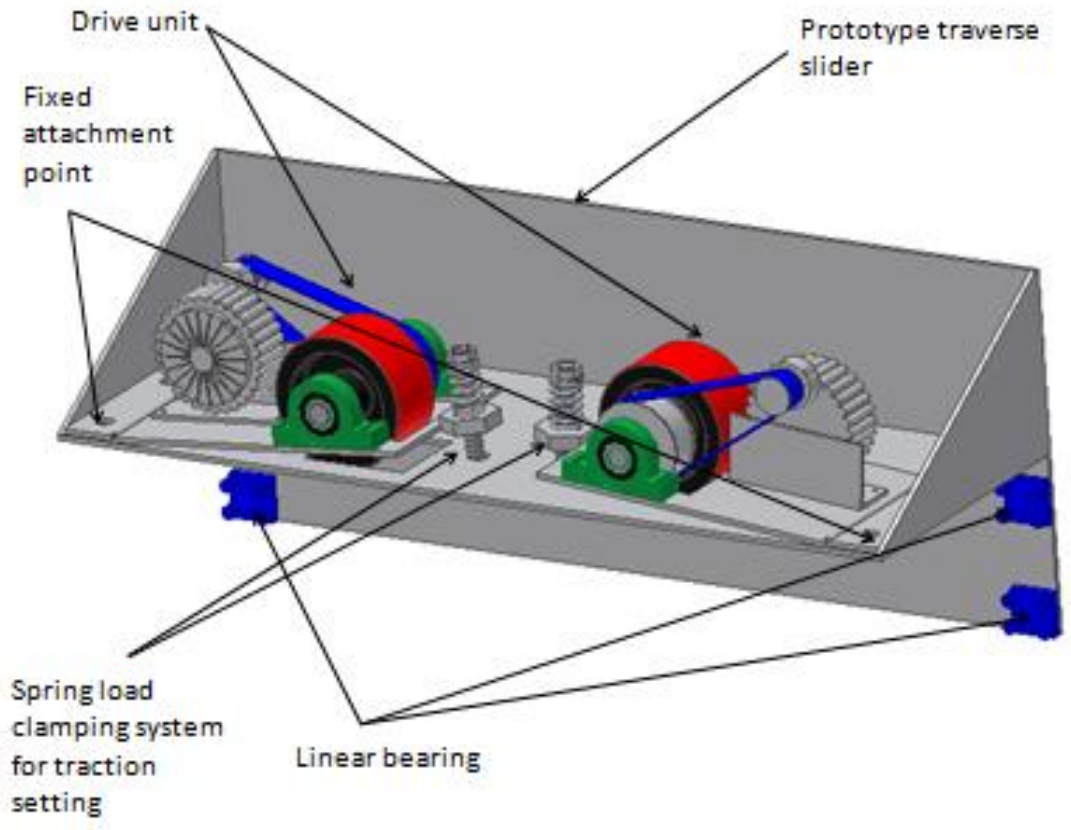

Figure 5. 21 Direct drive slider with linear bearing as passive rollers for load support

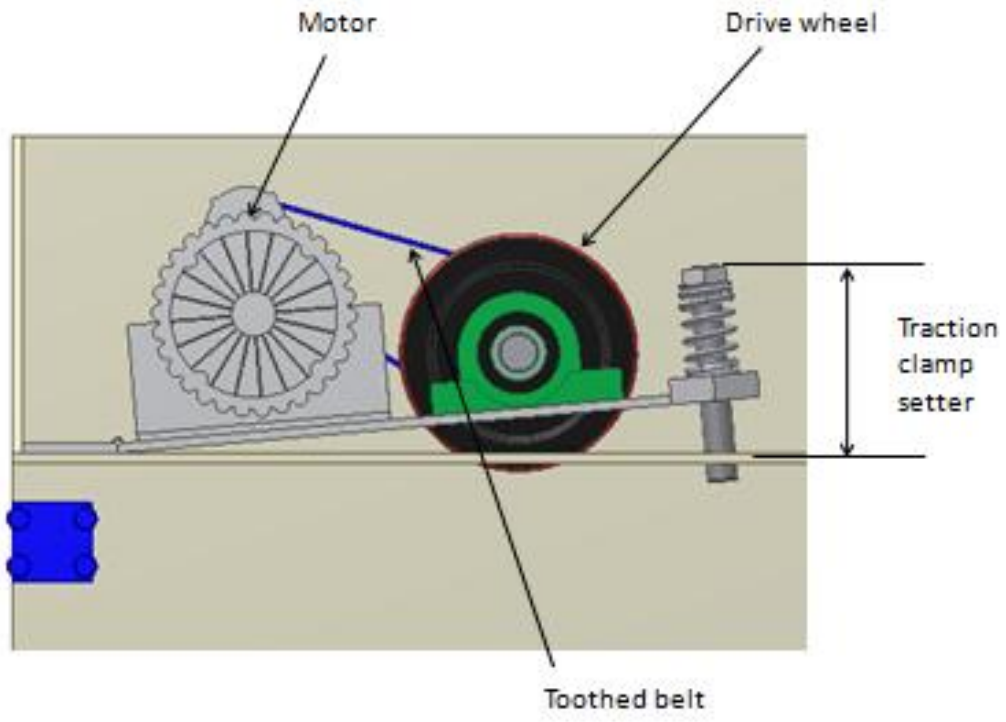

Figure 5. 22 Drive unit as installed to the traverse slider frame

Figure 5.23 shows the fabricated drive unit. The motor was originally assembled to a toothed gear, which were removed and replaced by a 31 mm diameter pulley. For driving, the drive wheel was attached to a 77 mm diameter pulley. The drive wheel diameter was 150 mm, while the width of the wheel was 75 mm. Power transfer was made through toothed belts for slippage resistance (Figure 5.24). The angular speed for the drive wheel was ω1, the angular speed for the drive pulley was ω2, and the angular speed for the motor pulley was ω3. Because they were attached to the same axis, ω1 was equal to ω2. In terms of linear speed transfer, linear speed of the intermediate pulley V2 was equal to the linear speed of the motor pulley V3.

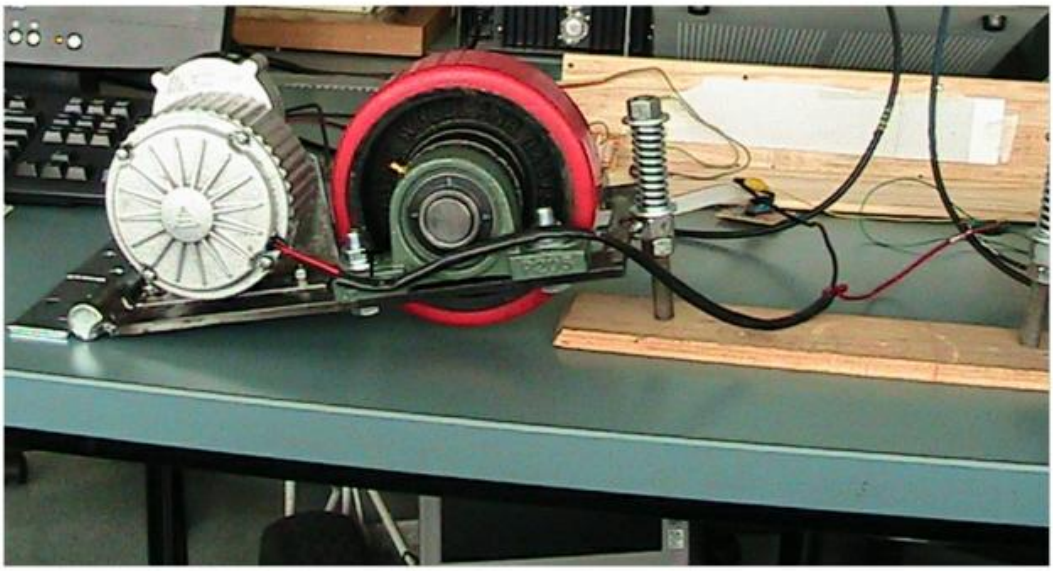

Figure 5. 23 The fabricated drive unit

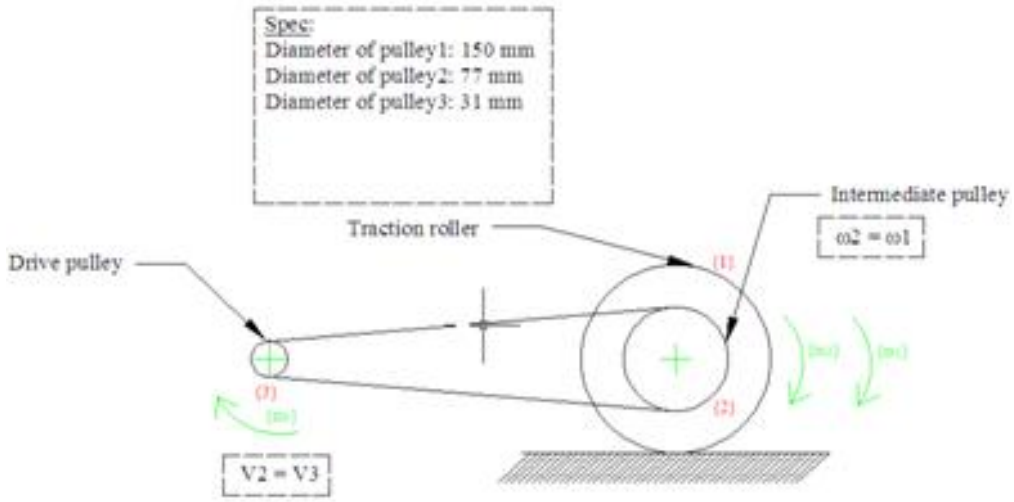

Figure 5. 24 Pulleys arrangement for power transfer between the drive motor and the drive wheel (traction roller)

The drive assembly was tested in the lab in order to verify the motion parameters. Under no load condition, the motor was attached to a laboratory power supply. The power supply was set at 24 volts. The time taken for the motor to settle at 1.8 A was recorded at an average of 2.24 s. Based on the manufacturer specifications; the maximum speed was 320RPM. The equivalent speed in radian per second was 33.52 rad/s. Therefore, the angular acceleration of the motor was the angular speed divided by the average time taken for the motor to reach maximum speed, which was 14.97 rad/s^2.

If the diameter of the motor pulley was 31 mm, the equivalent linear speed was 519.62 mm/s. The linear speed of the intermediate pulley was also 519.62 mm/s. Thus, the angular speed of the intermediate pulley was 13.50 rad/s, which was also the angular speed of the drive wheel. Therefore, the designed linear speed for this drive unit was 1012 mm/s, provided that the overall torque requirement was within 7.46 N-m. The designed speed and torque are inversely proportional; such if the requires torque is twice of the torque available, the speed is dropped to half of the theoretical maximum.

On the overall dimensions, the slider frame was one metre long along the traverse beam. Since the slider had taken a metre of the total span of the traverse beam, the operational working distance from side to side was reduced to four metres.

5.3.5 Bidirectional Control

Because current-load requires for this application was high, an H-bridge circuit was designed and fabricated. The circuit was designed for 30V and up to 15 A. Each MOSFET was attached to a heat sink. Operation of the H-bridge is based on the logical sequence in Table 5.1.

Table 5. 1 Logical input to the H-bridge

Operation	A	B
Brake	0	0
Clockwise	1	0
Counter clockwise	0	1
Free running	1	1

The H-bridge circuit was divided into two section, labelled as the A side and the B. The fundamental of H-bridge was the same for any design. However, the circuit could be design to suit for a particular operation.

Due to rapid switching, each MOSFET was attached to a heat sink. There were two logical points on the H-bridge marked as A and B, providing four levels of control to the motion of the motor. As of typical H-bridge design, a logical high on just one of the inputs point would result in motor rotation to either clockwise or anti-clockwise

directions. There were choices between a free run and a short circuit, and both could be accomplished if the logical point A and B received the same level of input. Since the slider was expected to operate continuously, providing high input to both A and B would allow the motor to rotate freely as the current flow was bypassed from the source to the ground. This characteristic should be beneficial when the motors were driven by a 'saw-tooth' waveform. The mark-space drive should take the form of drive-freewheel-drive-freewheel so that if both inputs are high the motor was open circuit. However if both were pulled low, a short circuit was applied across the motor, allowing a form of passive braking. In an emergency, where the motion needed to be halted, ground connection should serve this purpose. As such, no external braking mechanism was necessary. This would also simplify the design of the slider.

Power supply to the drive motor was provided by a fixed type power supply adapter that converted a typical 240V AC to 24V DC with electrical current up to 10 A. This power supplied was sized according to the specification of the motor. Since the design emphasize was to minimize the load on the slider, the power supply was housed in a metal casing located on the ground.

5.4 Other Components

As seen in figure 5.3 to 5.6, the vertical axis is experiencing the greatest deflection among all the axes because of contact between the tool and the workpiece. Therefore, adequate stiffness was essential for this member. The stiffness problem could be reduced if a slider type joint was applied. Thus, the reaction force could be absorbed

by the connection between the vertical to the traverse axis, rather than the motor for actuating the joints in rotational arrangements.

The longitudinal member was similar to the traverse member. However, there were two sides. On the end of each side, there were sliders that would carry the traverse members along the longitudinal track. The design of the longitudinal slider was also similar to the traverse slider, but they had different clamping configuration. The supporting roller on one side of the longitudinal member was fixed while the other side was hinged to the frame. In this arrangement, the non-fixed side could swing freely at limited angle in order to prevent binding. The only way the longitudinal member would bind is when the drive wheel set on each side of the slider was running in the opposite direction.

5.5 Results and Discussion

The linescan camera designed in Chapter 4 was applied in the test of the gantry. Using the edge detection algorithm, the camera could determine displacement instantaneously, using the central edge of the patterns as reference and the difference between two successive image sampling. The sensor read position as they were marked. Position was tracked as a combination of a coarse and fine tracking. A coarse tracking was based on a *cycle*. The variable *cycle* was written where a *cycle* referred to the displacement of two millimetres. This was also coincident with the actual pitch of the physical marking. A fine tracking was based on the difference between the central edges, which was under consideration at two successive intervals. For fine

tracking, the value of *fall1* that represented the central edge was utilized and marked as *pixel*. The variable *pixel* was compared to a variable *pix0*, which was set as the offset reference. In full distance measurement, *pix0* was the zero point, while in a case of setting a new datum; *pix0* would take the new designated value. Since the linescan camera was functioning as incremental encoder, one end of the traverse beam was set as the zero point, while the other end was the final point. Setting of the zero point was done when the slider was at one end of the track during initialization.

In order to verify the tracking quality of the displacement, the transducer was installed to the lateral beam of the slider. The lateral beam was designed to have a length of five metres, measured from end to end. Because the slider assembly was a metre long, roughly the entire travel distance was four metres. The displacement tracking was verified through a test, where the slider was set to move at the maximum speed attainable, hence measuring the overall travel distance. The motor assembly of the slider was connected to a 24 V DC power source for motorised movement. The slider was run from end to end, in both forward and reverse direction. There was a pair of runs, beginning with a forward motion. Once the slider reached the end, it moved in reversed. Because the objective was to measure the total distance travel, the slider was moved without control. Hence, switching was done manually. The switch was turned off once the slider hit the end and "bang". It was done in order to exclude the effect of gradual sliding before the slider was coming to full stop. The position of individual marking was plotted along the movement in order to determine the total distance travel. Position was calculated based on the source of falling edges, where, a cycle was set to be equal to 2000 microns, the resolution of the pixel was 40 microns. The

equation for position was described equation 5.12. Ten pairs of forward and reverse movement were recorded for verification of total distance travel. The time taken to traverse recorded by using a stopwatch and observation through the time stamp as received by the master computer for monitoring.

$$Position = (2000 \times cycle) + \left(\frac{(pixel - pix0) \times 1000}{phc} \right) \quad \text{(Eq. 5.12)}$$

Figure 5.25 shows a sample plot of a forward movement based on the *cycle* plot. This was a coarse estimate of the movement. Initially, the plot appeared as linear, where the slider was also stationary. The moment when the slider was moving, the plot began at zero and climbed up steady at constant rate, wherein the speed was at maximum. The speed was constant until the slider hit the end. There was a bang and the motor was switch off. There was a slight degradation, and in that instance, the cycle was bounced back by nearly 20 mm. This phenomenon was due to the slider being bounced by the wall. Because the power of the motor was cut-off at the moment of hitting, the slider was bounced and moved at free-wheel. In the data analysis, the data was cropped from the point of initial movement to the end point at which the slider hit the wall.

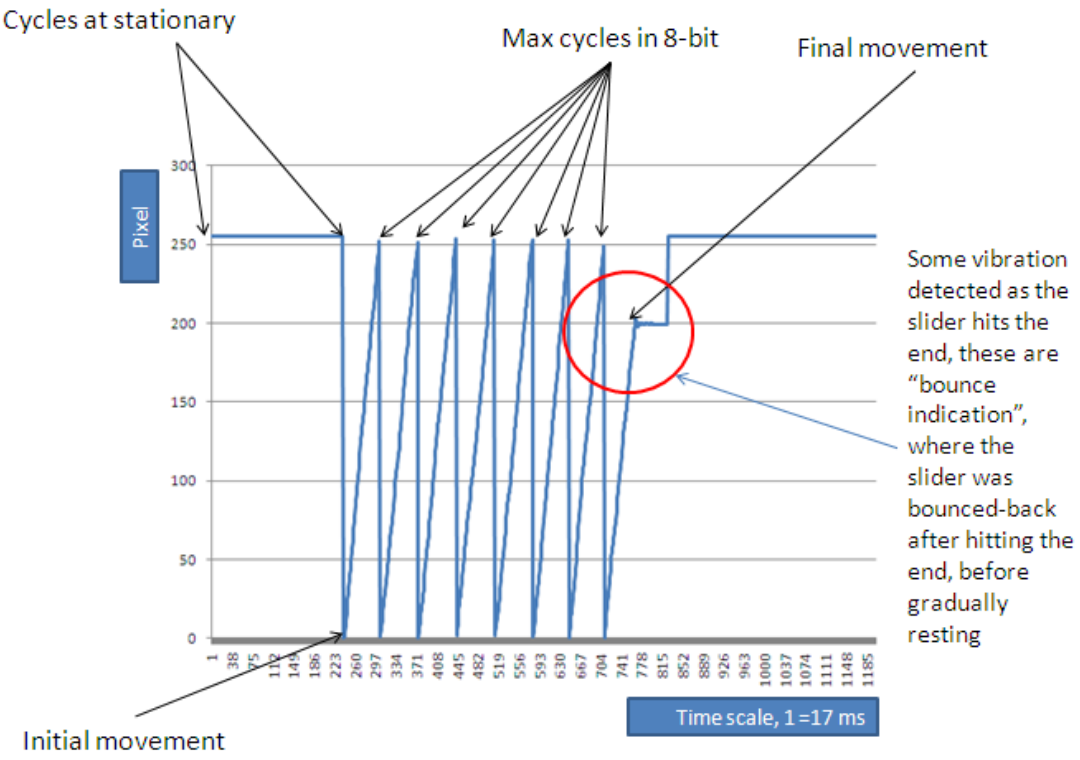

Figure 5. 25 Sample plot of a cycle in forward movement

The average distance travel for forward movement was 3976.04 mm. The average distance travel for reverse movement was 3976.00 mm. The difference between the distance measured between forward and reverse movement was 0.04 mm, which was 10% higher than the calibrated value for individual pixels. On the time taken to traverse at full distance, the time taken was 8.51 s for both forward and reverse motion. While there were slight variations in timing the slider movement with stopwatch, the timer on the plot indicated that for both movements, the time taken to traverse at full distance was 8.50 s. using the stop watch value, the average speed of the motion was 467.33 mm/s and 467.22 mm/s. The grand average for overall distance travel for the lateral beam was 3976.02 mm.

In positioning test, the slider on the lateral beam was fully controlled by the transducer. The motor assembly was connected to the 24 V DC power source via an H-bridge. The slider movement was initiated through a master controller. Communication between the master controller to the slider controller was established through ZigBee. The ZigBee was set as a general transceiver with open channel; hence the master controller was able to communicate with all ZigBee modules that were present. Because each slider had a unique address, a specific command was received by the target slider, where the command would be processed and executed. For a radius of within five metres, the ZigBee did not indicate any lost of data packet, even if the module was enclosed in a housing. The packet transmission rate was at 100% all the time.

Prior to testing for positioning accuracy, the parameters for drive, *u* were optimized. Because of quantization, *veldem* and *u* were rescaled to an inversely proportional constant. In testing the slider, it was found that the scale constant for *u* was directly related to the system damping. At a factor of 128 for example, damping was eradicated - underdamped, but at a cost of low stiffness. At a factor of 8 or less, the system was in overdamping condition. A compromise was found at a factor of 16. Therefore, the drive, *u* was written as velocity error, *velerror*/16.

The slider was tested for accuracy in placement, where the slider moves from origin to new a datum set, 1 m after the origin. The drive, *u* was set to be proportional to error. The error was observed to be reducing up to a certain point (Figure 5.26).

Although, the desired value was zero, the test indicated that there was an offset of 11 microns. Therefore, accuracy of measurement based on direct error feedback was 11 microns. The 11 microns was originated from the error of quantization of microcontroller.

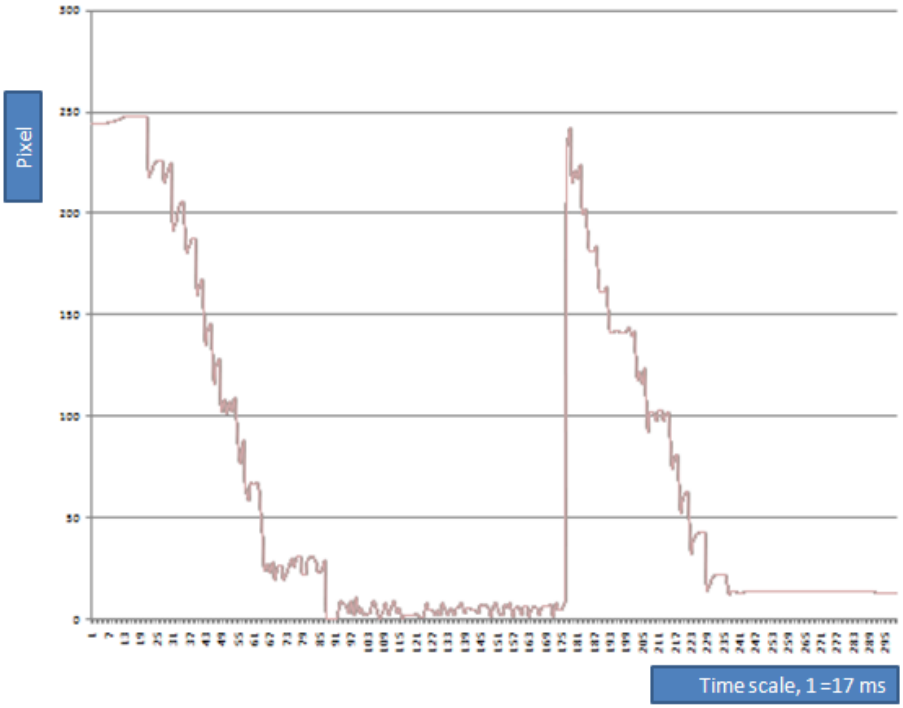

Figure 5. 26 Error measurement of a meter positioning track test

In the original algorithm, the plan was to utilize velocity demand for positioning control. Therefore, the drive *u* was back to using the value of velocity error. The slider was tested to run from origin to a new datum again at one meter. In the test, a major problem in positioning was detected as the error was obvious. Figure 5.27 shows the level of positioning error for various *posdiv* values. The target position was 1000 mm, but the slider was having a large deviation at various *posdiv* values. Apparently, the

scaling for velocity demand, *veldem* had affected the overall feedback of the system. Larger division for *veldem* led to contraction of the overall measurement. On the left hand side of the figure, the value of *posdiv* is 100. On the centre of the figure, the value for *posdiv* is 800. On the right hand right side of the figure, the value for *posdiv* was 2000. Optimum values for *posdiv* exist within the range of 800 to 1000, where deviation between go and return runs was at minimum. At *posdiv* higher than 1000, the deviation was small, but the positioning was offset by a 100 mm less.

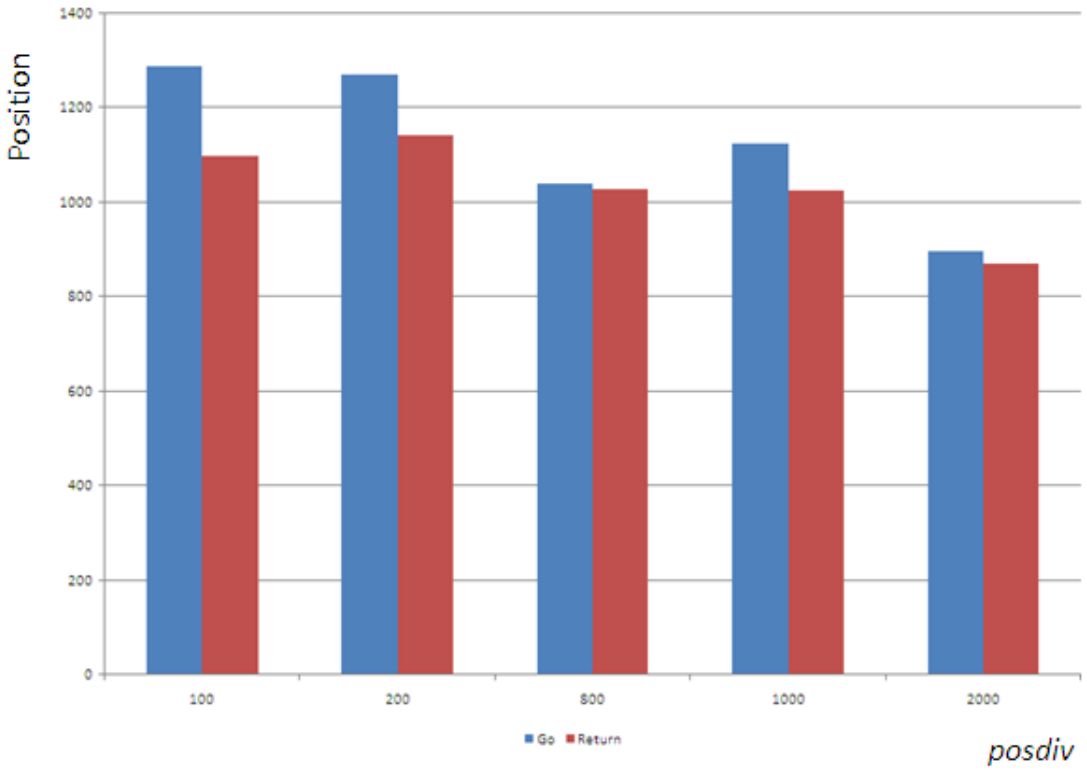

Figure 5. 27 Measured displacements at various *posdiv* constant, with a target position of 1000 mm

5.6 Summary

This chapter describes the design of long travel gantry. The design emphasised on light weight, thus innovative design in the driving was proposed. The slider component was based on direct drive, whereas a soft wheel and a preset load subassembly were used to provide traction. This eliminated the needs to cables or rotating rods for motion transfer. The linescan camera design in chapter 4 was installed to the gantry for feedback control. On direct positioning test, the positioning offset was 11 microns. When velocity error was used for feedback, the value required scaling constant factors between 800 to 1000.

Chapter 6

Conclusion and Future Works

6.1 Conclusion

Moulds for fabrication of fire reinforced plastics (FRP) parts are typically made of expanded polystyrene. In precise engineering, the polystyrene is machined using a multi-axis robotic or CNC platform. In current practice, there are limitations in the size of the machine. Thus oversize moulds which are longer and wider than a metre are made of several smaller segments. Bonding of these segments requires a lot of manual effort and cumulative errors are often encountered. Therefore a new approach is needed.

Motivated by the need of the industry, this research had identified the critical issues in the design of such a machine. The problems were interlocking. The type of material and the cutting approach had significant impact on the mechanical design. In the mean time, the mechanical design affected the level of machining accuracy, where the accuracy of cutting was also influenced by the controlling instrumentation.

A complete prototype requires continued effort, but the fundamentals concept of the design led to the breakthrough and establishment of direction. These were the critical issues being researched in this thesis.

In order to gain insight, the conventional approach as practiced by the industry was observed. In milling, the disadvantages were the requirement of a high-powered motor to actuate the spindle and generation of fine particles as by-products.

Slicing as an alternative cutting approach was proposed. The various aspects of slicing was observed and studied. This approach combined pushing and sideways motion that resulted in lower cutting forces than pushing alone. Cutter design for slicing varied from simple straight blades to curve and disk blades. The design of the cutter edge affected the appearance of the off-cuts significantly. Smoother edge had a tendency to produce smooth cuts. Serrated blades behaved like a mill cutter if the pitch of the teeth was greater. Further analysis on disk cutter revealed that the cutter could generate lower cutting force than mill at significantly lower feed speed.

In precise machining, the cutter and the mechanism required a feedback mechanism for control. It was possible for the design to achieve higher precision than required by the industry at the expanse of higher cost of development. An optical transducer design that encoded position directly from the image of a repetitive pattern was developed. The design of the transducer has proposed a variation on typical optical sensing, whereby direct image representation replaced the need for generating pulses. The result was a precise and cost-effective displacement transducer. Upon testing of the transducer, when error was used directly as the drive parameters, the slider could cover a one metre travel with 11 microns deviation. When velocity-demand, *veldem* replaced error for driving the slider, the deviation was at maximum. Only when the parameter *posdiv*, was changed to 800, then the deviation was improved.

Upon identification of an alternative cutter, the design of a machine to operate the tool was discussed. While most of the design fundamentals were similar to a typical gantry mechanism, the methods of actuating the slider was distinct. Weight and rigidity were two of the major concerns. Although the industrial partner rejected the proposed direct power connection, due to safety concern, an alternative that distribute traction was chosen. Since the motors consumed 24 VDC and 13 A, the cables for power connection was lighter and easier to manage. This had contributed to less weight imposed onto the structural mechanism.

6.1.1 Publication

The project was fully funded by the industrial partner. Due to the strict requirement requested by the industrial partner, publications were restricted. Only the study of using pixels for displacement sensing had been published and presented in *MAHADI, R. & BILLINGSLEY, J. (2008) Precise Measurement of Displacement using Pixels. Proceedings of World Academy of Science, Engineering and Technology, Bangkok Thailand, Volume 29, 29 May 2008, pp307-309. Bangkok, Thailand.*

6.2 Future work

Completion of a reliable prototype is progressing. The direction of the design had been established. The future works should embrace the following paths:

- A novel cutter path for slicing of polystyrene will need to be established. This will be significantly different than the path of milling because both cutters

behave differently. G-codes could be applied, thus integrating the machine to CAD/CAM.

- Further weight reduction should be established in the design for tool actuation. Instead of a multi-stage vertical arm, the system could be based on cable driven articulate actuator. The traverse and longitudinal members could be fabricated from fibre reinforced plastics for further weight reduction. This will require a new set of methodology to model and confirm the strength of the structure.
- While the accuracy of fabrication is influenced by the machine, having a fully adjustable flat floor will further enhance the capability of the machine. Inclusion of four poles on the further end of each corner will assist in recalibration and resetting of datum, provided that the poles will be acting as a secondary marker to the sensory system of the sliders.

Reference

AHN, D. G., LEE, S. H. & YANG, D. Y. (2003) A study on the influence of the sloped cutting angle on kerfwidth and part quality in the hotwire cutting of EPS foam for the VLM-s rapid prototyping process. *International Journal of Machine Tools & Manufacture,* 43.

ALEJANDRE, I. & ARTÉS, M. (2007) Method for the evaluation of optical encoders performance under vibration. *Precision Engineering,* 31**,** 114-121.

AMANO, Y., TSUJI, T., TAKAHASI, A., OUCHI, S., HAMATSU, K. & IIJIMA, M. (2003) A sensorless drive system for brushless DC motors using a digital phase locked loop. *Electrical Engineering in Japan,* 142**,** 57-66.

AMIN-NEJAD, S., SMITH, J. S. & LUCAS, J. (2003) A visual servoing system for edge trimming of fabric embroideries by laser. *Mechatronics,* 13**,** 533–551.

APNESETH, C., DZUNG, D., KJESBU, S., SCHEIBLE, G. & ZIMMERMANN, W. (2003) Wireless – introducing wireless proximity switches. *Sensor Review,* 23**,** 116-122.

ASPINWALL, D. K., DEWES, R. C., NG, E. G., SAGE, C. & SOO, S. L. (2007) The influence of cutter orientation and workpiece angle on machinability when high-speed milling Inconel 718 under finishing conditions. *International Journal of Machine Tools & Manufacture,* 47**,** 1839-1846.

ATKINS, A. G., XU, X. & JERONIMIDIS, G. (2004) Cutting, by 'pressing and slicing,' of thin floppy slices of materials illustrated by experiments on cheddar cheese and salami. *Journal of Materials Science,* 39**,** 2761-2766.

ATKINS, T. (2006) Optimum blade configurations for the cutting of soft solids. *Engineering Fracture Mechanics,* 73**,** 2523–2531.

BARONTI, P., PILLAI, P., CHOOK, V. W. C., CHESSA, S., GOTTA, A. & HU, Y. F. (2007) Wireless sensor networks: A survey on the state of the art and the 802.15.4 and ZigBee standards. *Computer Communications,* 30**,** 1655–1695.

BILLINGSLEY, J. (2006) *Essentials of Mechatronics,* Hoboken, New Jersey, Wiley-Interscience.

BRIËR, P., STEINBUCH, M. & JONKER, P. (2007) Low Latency 2D Position Estimation with a Line Scan Camera for Visual Servoing. IN AL., J. B.-T. E. (Ed.) *ACIVS 2007, LNCS 4678.*

BROGARDH, T. (2007) Present and future robot control development—An industrial perspective. *Annual Reviews in Control,* 31**,** 69–79.

BROWN, T., JAMES, S. J. & PURNELL, G. L. (2005) Cutting forces in foods: experimental measurements. *Journal of Food Engineering,* 70**,** 165–170.

CARR, J., DESMULLIEZ, M. Y. P., WESTON, N., MCKENDRICK, D., CUNNINGHAM, G., MCFARLAND, G., MEREDITH, W., MCKEE, A. & LANGTON, C. (2009) Miniaturised optical encoder for ultra precision metrology systems. *Precision Engineering,* 33**,** 263-267.

CHAUDHURI, R. A. & BALARAMAN, K. (2007) A novel method for fabrication of fiber reinforced plastic laminated plates. *Composite Structures,* 77**,** 160–170.

CIARDIELLO, T. (2005) Wireless communications for industrial control and monitoring. *IEE Computing & Control Engineering.*

DERBY, S. J. & BROWN, D. (2003) Distributed controlof a track based multi head robot. *Industrial Robot: An International Journal,* 30**,** 218-224.

DURSCH, A., YEN, D. C. & SHIH, D. H. (2004) Bluetooth technology: an exploratory study of the analysis and implementation frameworks. *Computer Standards & Interfaces,* 26**,** 263-277.

EDWARDS, K. L. (1998) An overview of the technology of fibre-reinforced plastics for design purposes. *Materials and Design,* 19**,** 1-11.

EKEKWE, N., ETIENNE-CUMMINGS, R. & KAZANZIDES, P. (2008) A wide speed range and high precision position and velocity measurements chip with serial peripheral interface. *INTEGRATION, The VLSI Journal,* 41**,** 297-305.

ETZION, T. & PATERSON, K. G. (1996) Near optimal single-track Gray Codes. *IEEE Transactions on Information Theory,* 42**,** 779-789.

FIGARELLA, T. & JANSEN, H. H. (2007) Brush wear detection by continuous wavelet transform. *Mechanical Systems and Signal Processing,* 21**,** 1212-1222.

FRAZZETTA, T. H. (1988) The mechanics of cutting and the form of shark teeth (Chondrichthyes, Elasmobranchii). *Zoomorphology,* 108**,** 93-107.

GALLINA, P. (2006) Delayed reference control for hotwire cutting of expandandable polystyrene foam. *Transactions of ASME,* 128**,** 360-365.

GIAM, T. S., TAN, K. K. & HUANG, S. (2007) Precision coordinated control of multi-axis gantry stages. *ISA Transactions,* 46**,** 399-409.

GOLNABI, H. (2003) Role of laser sensor systems in automation and flexible manufacturing. *Robotics and Computer Integreted Manufacturing,* 19**,** 201-210.

GUZEL, B. U. & LAZOGLU, I. (2004) Increasing productivity in sculpture surface machining via off-line piecewise variable feedrate scheduling based on the force system model. *International Journal of Machine Tools & Manufacture,* 44**,** 21–28.

HILTGEN, A. P., PATERSON, K. G. & BRANDESTINI, M. (1996) Single-track Gray Codes. *IEEE Transactions on Information Theory,* 42**,** 1555-1561.

HOUGHTON, H. (2002) LEDs: A flexible option for machine vision. *Sensor Review,* 22**,** 130-133.

HUA, Y. J. & SHINE, Y. K. (2007) Adaptive coupling control for overhead crane systems. *Mechatronics,* 17**,** 143-152.

JAMES, R., OZKAN, B. & RAVANI, B. (2006) Mechanical design of a robotic system for automatic installation of magnetic markers on the roadway. *Journal of Mechanical Design,* 128**,** 413-421.

JASPER, D. & FATIKOW, S. (2010) Line Scan-Based High-Speed Position Tracking Inside the SEM. *International Journal of Optomechatronics,* 4**,** 115-135.

JOUANEH, M., HAMMAD, A. & DATSERIS, P. (1997) A flexible automated foam cutting system. *International Journal of Machine Tools and Manufacture,* 37**,** 437-449.

KAO, C.-F. & LU, M.-H. (2005) Optical encoder based on the fractional Talbot effect. *Optics Communications,* 250**,** 16-23.

KIM, H. C., LEE, S. H. & YANG, D. Y. (2007) Development of a rapid heat ablation (RHA) process using a hot tool. *International Journal of Machine Tools & Manufacture,* 47**,** 124-132.

KISS, P. (2003) Rolling radii of a pneumatic tyre deformable soil. *Biosystems Engineering,* 85**,** 153-161.
KONDO, N. & TING, K. C. (1999) Robotics for Bioproduction Systems. St. Joseph.
KUC, T.-Y., BAEK, S.-M., SOHN, K.-O. & KIM, J.-O. (2003) Intelligent control of DC motor driven mechanical systems: a robust learning control approach. *Int. J. Robust Nonlinear Control,* 13**,** 71-90.
KUC, T.-Y., BAEK, S.-M., SOHN, K.-O. & KIM, J.-O. (2003) Intelligent control of DC motor driven mechanical systems: a robust learning control approach. *Int. J. Robust Nonlinear Control,* 13**,** 71-90.
LEE, E. T. & LEE, M. E. (1999) Algorithms for generating generalized gray codes. *Kybernetes,* 28**,** 837-844.
LI, C. & LEE, C. Y. (2001) Motion control of an auto-warehousing crane system. *IEEE Transactions of Industrial Electronics,* 48**,** 983-994.
LI, Y. S., YOUNG, T. Y. & MAGERL, J. A. (1988) Subpixels edge detection and estimation with a microprocessor-controlled line scan camera. *IEEE Transactions on Industrial Electronics,* 35**,** 105-112.
LÓPEZ RIQUELME, J. A., SOTO, F., SUARDÍAZ, J., SÁNCHEZ, P., IBORRA, A. & VERA, J. A. (2009) Wireless Sensor Networks for precision horticulture in Southern Spain. *Computers and Electronics in Agriculture,* 68**,** 25-35.
LU, Y.-S. & WANG, X.-W. (2009) Sliding-mode repetitive learning control with integral sliding-mode perturbation compensation. *ISA Transactions,* 48**,** 156-165.
LUO, P. F., PAN, S. P. & CHU, T. C. (2004) Application of computer vision and laser interferometer to the inspection of line scale. *Optics and Lasers in Engineering,* 42**,** 563–584.
LYE, S.-W., LEE, S.-G. & YEONG, H.-Y. (1996) An integrated, computer-assisted process planner for the machining of moulds for expanded polystyrene foam. *Integrated Manufacturing Systems,* 7**,** 53-60.
MAHADI, M. R. (2005) Design of Soil Bin Test Facility for Soil Dynamic Studies. MSc Thesis. *Biosystems Engineering.* Winnipeg, University of Manitoba.
MALKOCOGLU, A. & OZDEMIR, T. (2006) The machining properties of some hardwoods and softwoods naturally grown in Eastern Black Sea Region of Turkey. *Journal of Materials Processing Technology,* 173**,** 315-320.
MAO, J., TACHIKAWA, H. & SHIMOKOHBE, A. (2003) Precision positioning of DC motor driven aerostatic slide system. *Precision Engineering,* 27**,** 32-41.
MCGORRY, R. W., DOWD, P. C. & DEMPSEY, P. G. (2003) Cutting moments and grip forces in meat cutting operations and the effect of knife sharpness. *Applied Ergonomics,* 34**,** 375-382.
MERINO, S., RETOLAZA, A., JUARROS, A. & LANDIS, S. (2007) A new way of manufacturing high resolution optical encoders by nanoimprint lithography. *Microelectronic Engineering,* 84**,** 848-852.
MERRY, R. J. E., VAN DE MOLENGRAFT, M. J. G. & STEINBUCH, M. (2009) Velocity and acceleration estimation for optical incremental encoders. *Mechatronics,* In Press, Corrected Proof.
MORAIS, R., FERNANDES, M. A., MATOS, S. G., SERÔDIO, C., FERREIRA, P. J. S. G. & REIS, M. J. C. S. (2008) A ZigBee multi-powered wireless acquisition device for remote sensing applications in precision viticulture.

Computers and Electronics in Agriculture, 62**,** 94-106.
NADIMI, E. S., SØGAARD, H. T., BAK, T. & OUDSHOORN, F. W. (2008) ZigBee-based wireless sensor networks for monitoring animal presence and pasture time in a strip of new grass. *Computers and Electronics in Agriculture,* 61**,** 79-87.
NYCE, D. S. (2004) *Linear Position Sensor: Theory and Application,* Hoboken, New Jersey, John Wiley & Sons.
OZDEMIR, E. & KARACOR, M. (2006) Mobile phone based SCADA for industrial automation. *ISA Transactions,* 45**,** 67-75.
PALLAY, J., KELEMEN, P., BERGHMANS, H. & DOMMELEN, D. V. (2000) Expansion of polystyrene using water as the blowing agent. *Macromol. Mater. Eng.* , 275**,** 18–25.
PEREZ, H., VIZAN, A., HERNANDEZ, J. C. & GUZMAN, M. (2007) Estimation of cutting forces in micromilling through the determination of specific cutting pressure. *Journal of Materials Processing Technology,* 190**,** 18-22.
PETROVIC, G., KILIC, T. & TERZIC, B. (2009) Sensorless speed detection of squirrel-cage induction machines using stator neutral point voltage harmonics. *Mechanical Systems and Signal Processing,* 23**,** 931-939.
POSTHUMA, A. (2007) Development of a novel robotically effected plastic foam sculpting system for rapid prototyping and manufacturing. *Mechanical Engineering.* Christchurch, New Zealand, University of Canterbury.
REY, A. D. (2005) Mechanics of soft-solid–liquid-crystal interfaces. *PHYSICAL REVIEW E,* 72**,** 1-15.
RIEBER, J. M. & TAYLOR, D. G. (2004) Integrated control system and mechanical design of a compliant two-axes mechanism. *Mechatronics,* 14**,** 1069-1087.
RUSMEE, P. & DEVRIES, K. L. (2001) Mechanical properties of EPS foam do not behave as material constants. *American Physical Society, Annual March Meeting, March 12 - 16, 2001 Washington State*
Convention Center Seattle, Washington Meeting ID: MAR01, abstract #N17.008. Washington, USA.
SAFARIC, S. & MALARRIC, K. (2006) ZigBee wireless standard. *48th International Symposium ELMAR-2006.* Zadar, Croatia.
SAITO, Y., ARAI, Y. & GAO, W. (2009) Detection of three-axis angles by an optical sensor. *Sensors and Actuators A: Physical,* 150**,** 175-183.
SAMAD, T., MCLAUGHLIN, P. & LU, J. (2007) System architecture for process automation: Review and trends. *Journal of Process Control,* 17**,** 191–201.
SANTIAGO-PEREZ, J. J. D., OSORNIO-RIOS, R. A., ROMERO-TRONCOSO, R. D. J., HERRERA-RUIZ, G. & DELGADO-ROSAS, M. (2008) DSP algorithm for the extraction of dynamics parameters in CNC machine tool servomechanisms from an optical incremental encoder. *International Journal of Machine Tools & Manufacture,* 48**,** 1318-1334.
SARWAR, M., MARTINPERSSON, HELLBERGH, H. K. & HAIDER, J. (2009) Measurement ofspecific cutting energy for evaluating the efficiency of bandsawing different workpiece materials. *InternationalJournalofMachineTools&Manufacture,* 49**,** 958–965.
SCHWARTZ, M. & ETZION, T. (1999) The structure of single-track gray codes. *IEEE Transactions on Information Theory,* 45**,** 2383.

SCIAVICCO, L. & SICILIANO, B. (1996) *Modeling and Control of Robot Manipulators,* Singapore, McGraw-Hill International Editions.
SECO, F., MARTÍN, J. M., JIMÉNEZ, A. R. & CALDERÓN, L. (2005) A high accuracy magnetostrictive linear position sensor. *Sensors and Actuators A: Physical,* 123-124**,** 216-223.
SECO, F., MIGUEL MARTÍN, J., PONS, J. L. & JIMÉNEZ, A. R. (2004) Hysteresis compensation in a magnetostrictive linear position sensor. *Sensors and Actuators A: Physical,* 110**,** 247-253.
SENCER, B., ALTINTAS, Y. & CROFT, E. (2008) Feed optimization for five axis CNC machine tools with drive constraints. *International Journal of Machine Tools & Manufacture,* 48**,** 733-745.
SENOL, I., DEMIRTAS, M., RUSTEMOV, S. & GUMUS, B. (2003) Position control of induction motor a new bounded fuzzy sliding mode controller. *The International Journal for Computation and Mathematics in Electrical and Electronic Engineering,* 24**,** 145-157.
SHAN, L. & QIAO, P. (2005) Flexural–torsional buckling of fiber-reinforced plastic composite open channel beams. *Composite Structures,* 68**,** 211–224.
SHARMA, A. K. & PANDEY, K. P. (1998) Traction data analysis in reference to a unique zero condition. *Journal of Terramechanics,* 35**,** 179-188.
SHEEN, B.-T. & YOU, C.-F. (2006) Machining feature recognition and tool-path generation for 3-axis CNC milling. *Computer-Aided Design,* 38**,** 553–562.
SHMULEVICH, I., MUSSEL, U. & WOLF, D. (1998) The effect of velocity on rigid wheel performance. *Journal of Terramechanics,* 35**,** 189-207.
SORENSEN, K. L., SINGHOSE, W. & DICKERSON, S. (2007) A controller enabling precise positioning and sway reduction in bridge and gantry cranes. *Control Engineering Practice,* 15**,** 825-837.
TAN, K. K., LIM, S. Y., HUANG, S., DOU, H. F. & GIAM, T. S. (2004) Coordinated Motion Control of Moving Gantry Stages for Precision Applications Based on an Observer-Augmented Composite Controller. *IEEE Transactions on Control Systems Technology,* 12**,** 984-991.
THOMPSON, B. S. & SUNG, C. K. (1985) The design of robots and intelligent manipulators using modern composite materials. *Mechanism and Machine Theory,* 20**,** 471-482.
TLALE, N. S., POTGIETER, J. & BRIGHT, G. (2003) Wireless teleoperated mechatronics control system for camera platform positioning. *Industrial Robot: An International Journal,* 30**,** 177-183.
TUTUNEA-FATAN, O. R. & FENG, H.-Y. (2005) Determination of geometry-based errors for interpolated tool paths in five-axis surface machining. *Transactions of the ASME,* 127**,** 60-67.
WANG, X., LU, H., QIAN, F. & BU, Y. (2001) Laser diode interferometer used for measuring displacements in large range with a nanometer accuracy. *Optics & Laser Technology***,** 219–223.
WEBSTER, J. G. (1999) *The Measurement, Instrumentation and Sensors Handbook,* CRC Press, Springer and IEEE Press.
WILLIAMS, J. G. (1998) Friction and plasticity effects in wedge splitting and cutting fracture tests. *Journal of Materials Science,* 33**,** 5351-5357.
WONG, J. Y. (1989) *Terramechanics and Off-road Vehicles Engineering,*

Amsterdam, Elsavier
WU, J., PU, D. & DING, H. (2007) Adaptive robust motion control of SISO nonlinear systems with implementation on linear motors. *Mechatronics*, 17**,** 263-270.
XIAO-WEN, L., MAN-YI, W., JIN-CHAO, W. & ZHENG-FANG, Z. (2009) Transmission performance of 2.4 GHz wireless sensor nodes when used in a working-face environment. *Mining Science and Technology (China)*, 19**,** 0185–0188.

Appendix

H-Bridge for Bi-Directional Control:

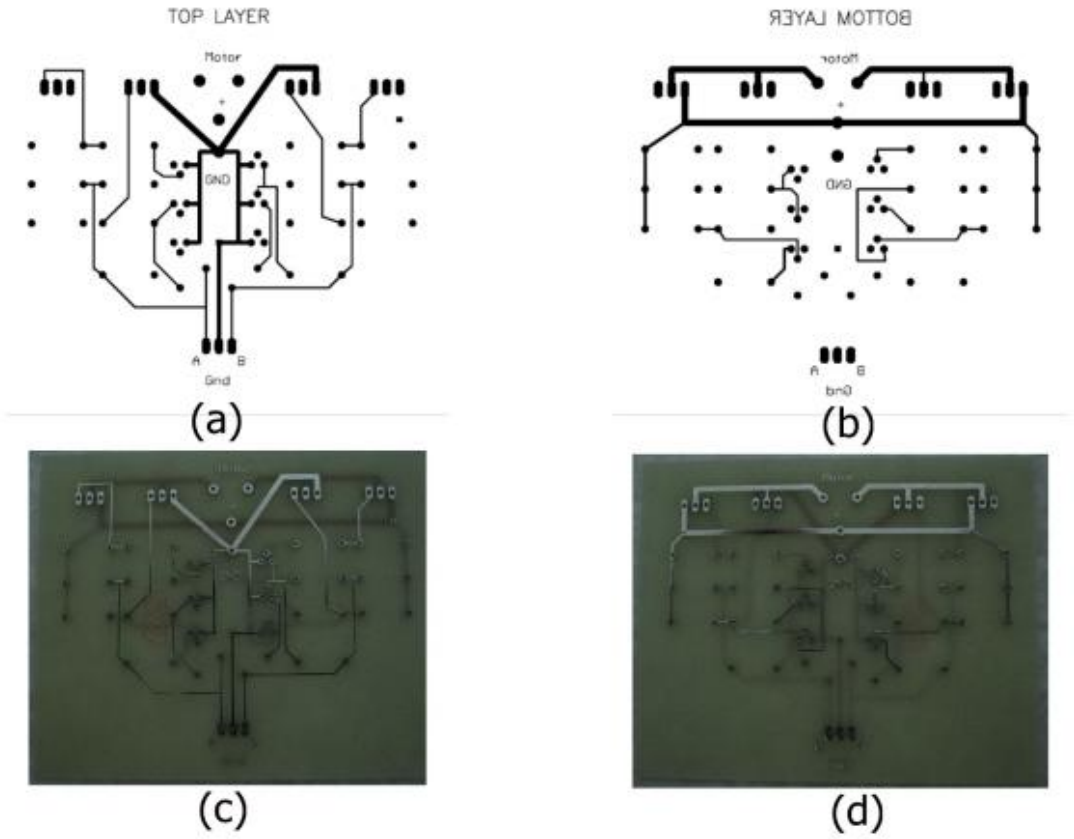

H-bridge Schematics:

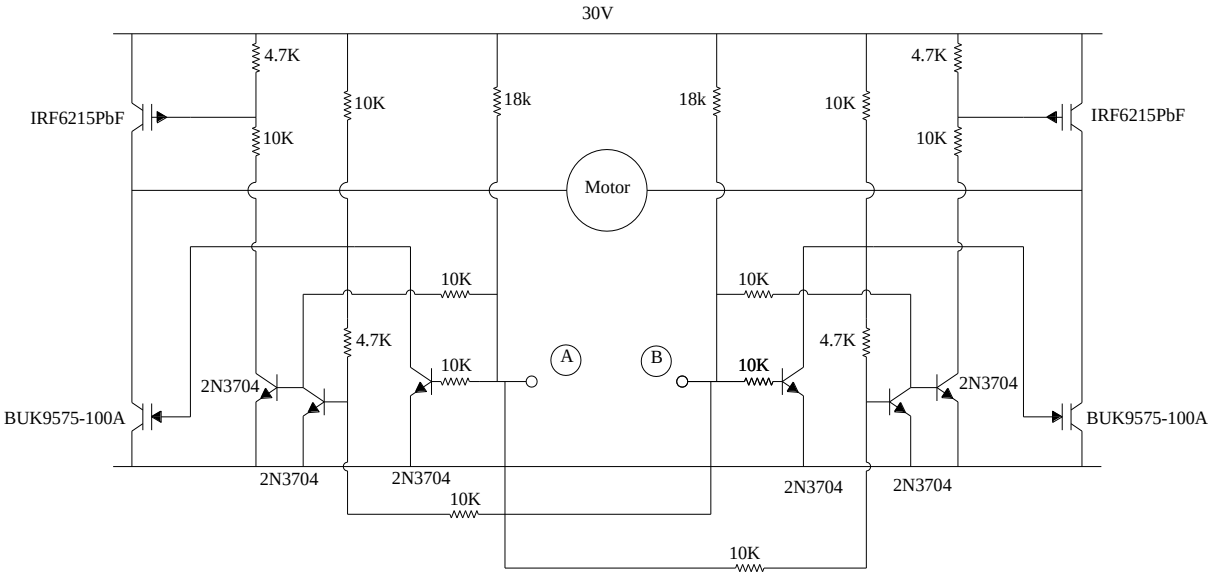

Source Code for Atmega128:

/***

controller: Atmega128
Communication:
'Multidrop' system in which all cards receive the same signal and all transmit their data
on a single pair of lines or radio channel.
All communication is initiated by the Master machine.
Each output byte contains four command bits and four data bits.
Each output packet starts with 0x and ends with FF

0x: The first byte of an output packet is the address of a controller -

One-byte commands to all controllers:

0E: All execute stored command now. (New target, new speed limit)
0F: all apply brakes,

so we could have up to 14 axes.

Succeeding bytes carry data values, for stored 'next command':

3x: Most significant used 'nibble' of target position (a nibble is 4 bits)
4x: next nibble - multiples of 6.5 cm
5x: next nibble - multiples of 4 mm
6x: next nibble - multiples of .25 mm
7x: smallest used nibble, multiples of 16 micron.

The position variable is held as a 'long', 8 nibbles. The lsb of each nibble is as follows:
1 micron, 16 micron, .25 mm, 4 mm, 6.5 cm, 1 metre, 16 metre, 256 metre
thus the two most significant nibbles are not used for commands.

8x: Most significant nibble of speed limit
9x: Least significant nibble of speed limit - eight bits is enough.

10: Do it now - apply new targets without waiting. Clear 'stop mode'.
11: Enter 'stop' mode, apply braking drive.
12: Apply position target to replace present measured position.

Switch-on calibration might be:
start in 'stop mode'
send speed limit of minimum,
send position target of 1 metre
send 'set present position'.
send position target of zero.
send 'do it now'

Axis starts to move slowly, master waits for sensor to indicate limit reached,
sends 'set stop mode'
sends position target zero
sends set present position.

Ax: Tell me:
A0: Present position
A1: Present speed
A2: Target position (for diagnostics)
A3: Speed limit (for diagnostics)

FF: End of packet
F0: All stop talking.
F1: Heartbeat. If micros do not hear this regularly, they stop.

For the reply from the micro:

First byte is ID echo.
Second byte is a nibble of data with appropriate tag or echo of a command.
Then more data
FF to end the packet.

The routine in the micro is:
On interrupt, build the packet.
When FF has been received, process the packet.

1. Is the first byte my address?
2. Is it a general action - such as "Do it now", "Stop talking", "Pause"?
3. If not, clear packet and wait for the next.

If it is 'me', send ID at once.
Send command echo or requested data.
Send FF.

(Remember that input and output are on separate lines, so micros cannot hear each other.)

So to translate an XY G-code we could have

Message for chip 0: New target.
Message for chip 1: New target.
General message 'do it now'.

An interface program send a command and the command is executed by
the controller

```
**********************************************************************
/

#include <avr/sfr_defs.h>
#include <avr/interrupt.h>
#include <avr/io.h>

/* UART setting */
#define FOSC 8000000 // Clock Speed, 8 MHz
#define BAUD 19200
#define MYUBRR FOSC/16/BAUD-1

/* Board ID */
char board=0x1;// board#1

/* For timeslice scheduling */
```

```
unsigned char step;
short ramp;
short slope=1;


/* For Message */
int newbytes;
char buffer[18];
char newbyte[18];
char respon;
short meslen;
unsigned char code;
unsigned char load;

/* for uart */
short nbytes;
short nb;
unsigned char busy=0;
char packet[18];
short n;
unsigned char i;

/* for linescan() */
unsigned char count;
char bright;
char oldbright;
char edge[17];
#define expose 25;
unsigned char nedge=0;

/* for track() */
#define phc 25; //pixels per halfcycle - pixels/mm
long pixpercycle=2*phc;
long pixhalfcycle=phc;
long micronperpixel=1000/phc;
char mask=10;      //pixels to crop from start of scan
char rise[5];
char fall[5];
char mark[5];      //intervals between level changes
char pitch[5];     //cycle - interval betweeen similar edges
long position=0;   // in microns.  Range is 2^31 = 2000 metres
long cycles=0;
long pixels;
long pix0;         //Datum for pixels
long move;
long speed;
char speed8;
```

```
short oldrise;
short oldfall;

/* for control(), mark-space */
char stop=0;       //Change to '1' for final version.
short u;
long newtarget=0;
char *pnt=&newtarget;

long target;

long error;
short veldem;
short velerror;

long bob=1;

// u max = 10
short velmax=phc;  //initial value 1 metre per second
long posdiv=1000;   //10 for 4mm error

//Prototypes - instead of header file
void init_uart(unsigned int ubrr);
void uart_transmit(void);
void linescan(void);
void track(void);
void control(void);
void obey(void);
void process(void);
void markspace(void);


/* Initiate UART channel 1 */
void init_uart(unsigned int ubrr){
        /*Set baud rate*/
        UBRR1H =0;
        UBRR1L = (unsigned char)ubrr;

        /*Enable receiver and transmitter*/
        UCSR1B = (1<<RXEN1)|(1<<TXEN1)|(1<<TXCIE)|(1<<RXCIE);

        /*Set frame format: 8data, 2stop bit*/
        UCSR1C = (1<<USBS1)|(3<<UCSZ10);
}

void obey(void){
        if(buffer[0]==board){
```

```
 for (i=0;i<meslen; i++){
        code = buffer[i]&0xf0;
        load = buffer[i]&0x0f;
        switch (code){
                case 0x30:
                  newtarget=0;
                  *(pnt+2)|=load<<4;
                  break;
                case 0x40:
                  *(pnt+2)|=load;
                  break;
                case 0x50:
                  *(pnt+1)|=load<<4;
                  break;
                case 0x60:
                  *(pnt+1)|=load;
                  break;
                case 0x70:
                  *pnt|=load<<4;
                  break;
                case 0x80:
                  velmax=load<<4;
                  break;
                case 0x90:
                  velmax|=load;
                  break;
                case 0x10:
                  target=newtarget;
                  stop=0;
            break;
                case 0x11:
                  stop=1;
                  PORTB=0;
                  break;
                default:
                  break;
        }
                if(code==0x12){
                  cycles=newtarget/2000;  //set new position datum
                  pix0=(newtarget-2000*cycles)/micronperpixel;
                 }

 }
}else if(code==0x0e){
 target=newtarget;
 stop=0;
}else if(code==0x0f){
```

```
            stop=1;
            PORTB=0;
        }
        meslen=0;
}



void linescan(void){
        nedge=0;
        PORTC=2+128; //SI
        PORTC=3; //SI and CLK
        PORTC=1; // CLK
        PORTC=0; //CLK low, can read data
        oldbright=PINA&128;//First pixel
        for (count=0;count<127;count++){
                PORTC=bright+1; //CLK High
                PORTC=bright; //CLK Low
                bright=PINA&128;
                if((bright!=oldbright)&&(count>mask)){
                        edge[nedge]=count|bright;
                        if(nedge<16){nedge++;}
                        oldbright=bright;
                }
        }

}

void track (void){
        // Edge selection, must have at least 4 edges
        // Pixels mapping
        if (nedge>4){
                if (edge[1]&128){
                        rise[0]=(edge[1]&127)-mask; // Start with rising edge
                        fall[0]=edge[2]-mask;
                        rise[1]=(edge[3]&127)-mask;
                        fall[1]=edge[4]-mask;
                        rise[2]=(edge[5]&127)-mask;
                        fall[2]=edge[6]-mask;

                        pitch[0]=rise[1]-rise[0];
                        mark[0]=fall[0]-rise[0];
                        mark[1]=rise[1]-fall[0];

                }else{
                        fall[0]=edge[1]-mask; // Start with falling edge
```

```
                rise[0]=(edge[2]&127)-mask;
                fall[1]=edge[3]-mask;
                rise[1]=(edge[4]&127)-mask;
                fall[2]=edge[5]-mask;
                rise[2]=(edge[6]&127)-mask;
                pitch[0]=fall[1]-fall[0];
                mark[0]=rise[0]-fall[0];
                mark[1]=fall[1]-rise[0];
        }

        pixels=fall[1];
        move=fall[1]-oldfall;   //pixels per millisecond

        if (move>pixhalfcycle){
                move-=pixpercycle;
                cycles-=1;
        }
        if (move<-pixhalfcycle){
                move+=pixpercycle;
                cycles+=1;
        }

        position=2000*cycles + (pixels-pix0)*micronperpixel;

        speed=speed+((move*micronperpixel)-speed)/8;
//time constant is 8 ms, scale is micron/msec = mm/sec
//quantisation residual is 7 (decay value if move = 0)

        speed8=speed>>8;                //for plotting
        oldrise=rise[0];
        oldfall=fall[1];
    }
}

void control(void){

    error=target-position;
    veldem=(error/posdiv);  //micron/sec

//      if (veldem>velmax){veldem=velmax;}
//      if (veldem<(-velmax)){veldem=(-velmax);}

    velerror=veldem-speed;

  u=velerror/16;
    //u=velerror/128;
```

```
        if (u>10){u=10;}
        if (u<-10){u=-10;}

//      u=velerror;
}

ISR(USART1_TX_vect){
  if(nb<=nbytes){
        UDR1=packet[nb];
                nb+=1;
  }else{
    busy=0;
  }
}

/* set the number of byte to send
- send the bytes back to the PC */
void uart_transmit(void){
        if (busy==0){
                nbytes=5;//bytes to send
                busy=1;
                nb=0;
                UDR1=255;
        }

        /*send bytes*/
        packet[0]=pixels-pix0;//fall[1];//vernier
        packet[1]=cycles;//cycles;//position
        packet[2]=speed8;//speed8;//speed
        packet[3]=target;
        packet[4]=u;
        packet[5]=newtarget/100;
}

/* interrupt while receiving newbytes
- process the newbytes */
ISR(USART1_RX_vect){
        newbytes=UDR1;//data from the user
        //target=UDR1;
        buffer[meslen]=newbytes;//build an array
        meslen++;//increase message length
}



/* Scheduling routines */
ISR(TIMER0_COMP_vect){
```

```
        TCNT0=0;
        step++;
        switch(step){
          case 25:          //expose:
            linescan();
            step=0;
            break;
          case 1:
                  track();
                  break;
          case 2:
            control();
                  break;
          case 3:
            markspace();
            break;
          case 4:
                  uart_transmit();
            break;
          case 5:
                  if (newbytes==0xff){
                    obey();
                    meslen=0;  //reset the message length
                  }else if (newbytes==0xfe){
                    stop=1;
                    PORTB=0;   //apply brakes
                  }
        }


}

void markspace (void){
        /* mark space */
        ramp+=slope;
        if (ramp>=10){slope=-1;}
        if (ramp<=0){slope=1;}
        /* drive */
        if (stop==0){
          if (u>ramp){PORTB=1;}          //drive forward
          else if(u<(ramp-10)){PORTB=2;} //drive reverse
          else{PORTB=3;}                 //Freewheel
        }else{
          PORTB=0;
        }               //Apply brakes
}
```

```
int main (void){
	// Initiate UART
	init_uart(MYUBRR);

	// Initialize IO ports
	DDRA=0;
	PORTA=(1<<PORTA7);
	DDRB = 255;//All port B as output
	DDRC=255; //All port C as output

	DDRD=48;//(1<<PD4)|(1<<PD5); //PD4 & PD5 for Timer1, PD7 for Timer2,
as output
	DDRF=0; // as input
	PORTF=255;//(1<<PORTF7); //set high to PinF7

	// Set Timer0 Comparator
	TCCR0=(1<<CS01)|(1<<CS00); //Timer clock
	OCR0=5; // no of counter increment before interrupt
	TIMSK=(1<<OCIE0); //Enable timer0 Comparator
	TIFR=(1<<OCF0); //Clear pending interrupt

	sei(); // enable global interrupt
	while (1){}
	return 0;
}
```

Sample Frame Capture in Cutting Video Analysis: